# FORWARD DI-HADRON ASYMMETRIES FROM $p^{\uparrow(\downarrow)} + p$ AT $\sqrt{s} = 200$ GeV AT STAR

A Dissertation

by

JAMES LUCUS DRACHENBERG

Submitted to the Office of Graduate Studies of
Texas A&M University
in partial fulfillment of the requirements for the degree of

DOCTOR OF PHILOSOPHY

May 2012

Major Subject: Physics

# FORWARD DI-HADRON ASYMMETRIES FROM $p^{\uparrow(\downarrow)} + p$ AT $\sqrt{s} = 200$ GeV AT STAR

A Dissertation

by

JAMES LUCUS DRACHENBERG

Submitted to the Office of Graduate Studies of
Texas A&M University
in partial fulfillment of the requirements for the degree of

DOCTOR OF PHILOSOPHY

Approved by:

| | |
|---|---|
| Chair of Committee, | Carl A. Gagliardi |
| Committee Members, | Che-Ming Ko |
| | Saskia Mioduszewski |
| | Joseph Natowitz |
| | Robert Tribble |
| Head of Department, | George R. Welch |

May 2012

Major Subject: Physics

# ABSTRACT

Forward Di-hadron Asymmetries from $p^{\uparrow(\downarrow)} + p$ at

$\sqrt{s} = 200$ GeV at STAR. (May 2012)

James Lucus Drachenberg, B.S., Abilene Christian University

Chair of Advisory Committee: Dr. Carl A. Gagliardi

One unresolved question in hadronic physics is the origin of large transverse single-spin asymmetries, $A_N$, observed in hadron production from high-energy polarized-proton collisions. Collinear perturbative Quantum Chromodynamics (pQCD) predicts that $A_N$ should scale with the quark mass, however, experiments have since reported large $A_N$ for inclusive hadron production. Recent measurements from RHIC experiments show examples of these asymmetries at forward angles in a kinematic region where pQCD cross-section calculations reasonably agree with measured cross-sections.

Disentangling dynamical contributions to $A_N$ from hadro-production requires moving beyond inclusive measurements. One possibility is to investigate asymmetries in two-particle correlations due to Interference Fragmentation Functions (IFF) and the Sivers effect. In 2008, RHIC dedicated a portion of the run to transversely polarized proton collisions at $\sqrt{s} = 200$ GeV. STAR was equipped with a Foward Meson Spectrometer (FMS) and a Forward Time Projection Chamber (FTPC), overlapping in the pseudorapidity range of $2.5 < \eta < 4$. By analyzing neutral pions with the FMS correlated with charged particles from the FTPC, correlation asymmetries can be measured at kinematics where large inclusive asymmetries have been measured.

Correlations are measured for $\pi^0$'s with $2 < p_{T,\pi^0} < 5$ GeV/c and associated charged particles in two ranges of transverse momentum: $1 < p_{T,\mathrm{ch}} < 2$ GeV/c and $0.5 < p_{T,\mathrm{ch}} < 1$ GeV/c. IFF and Sivers asymmetries manifest themselves through the

correlation of two particles from the same jet. These events are selected through a cut on the pair radius, $\Delta R$. Gain non-uniformities and electronics failures have resulted in large holes in trigger acceptance and associated particle acceptance, respectively. This non-uniform acceptance allows the Sivers and IFF effects to mix and distort the raw asymmetries. Techniques are developed to measure this leak-through by means of unpolarized yields and event weighting. They result in small corrections to the asymmetries.

IFF and Sivers asymmetries both for $x_F > 0$ and for $x_F < 0$ are reported for forward-angle $\pi^0$-charged particle correlations from polarized-proton collisions at $\sqrt{s} = 200$ GeV. Asymmetries are shown corrected for full underlying-event and pile-up backgrounds, as well as corrected only for pile-up contributions. It appears the asymmetries are less sensitive to $\Delta R$ when corrected for the full underlying-event background. Unfortunately, statistics limitations preclude a firm conclusion.

To Him Who laid the foundation of the earth

# ACKNOWLEDGMENTS

To my wife, Dr. Annie Drachenberg, M.D., thank you for your patience, support, and love, without which this would not have been possible. To my son, Daniel, thank you for helping me keep a perspective on the important things in life. To my advisor, Dr. Carl Gagliardi, thank you for invaluable guidance, instruction, and generous accommodation during times my family needed me. To my parents, Mike and Paula Drachenberg, thank you for your love, support, and for being the first to suggest I could, one day, pursue a doctorate. To my grandfather, Mr. Lester Wynn, thank you for cultivating my fascination with the physical sciences and showing me wisdom is greater than the university. To my late grandfather, Dr. Cecil Drachenberg, Ed.D., thank you for your legacy of doctorate-level education and carving a path for our family to Abilene Chrstian University. To Dr. Steven Hepplemann, thank you for your critical contribution to the theories which I have studied and for your valuable feedback and dialogue. To Dr. Len Eun, thank you for your solidarity during our graduate school trials and for the enlightening and honest discussion of the great mysteries of life. To Dr. Akio Ogawa, thank you for helping me integrate into the STAR FMS group. To Dr. Rusty Towell and Dr. Donald Isenhower, thank you for teaching me to love nuclear physics and for pointing me toward Texas A&M University. To Mr. Matthew Shaw, thank you for mentoring me in my first year of physics research with PHENIX and in my first year of physics laboratories at Abilene Christian University. To Mrs. Gail Lilly and Mr. Kenneth Parrish, thank you for introducing me to the study of physics and fostering my love for mathematics at Northland Christian School. To my friend Mr. Cody McCain, thank you for your loyalty and camaraderie through the years. To my friend Mr. Blake Haws, thank you for continuing to challenge me in all ways intellectual, ethical, moral, and spiritual after nearly 30 years of friendship.

# TABLE OF CONTENTS

CHAPTER Page

# LIST OF TABLES

# LIST OF FIGURES

FIGURE Page

FIGURE Page

FIGURE Page

FIGURE Page

FIGURE Page

FIGURE Page

FIGURE Page

FIGURE Page

FIGURE Page

FIGURE Page

FIGURE Page

# CHAPTER I

# INTRODUCTION

The nature of spin in particle physics has been described as everything from "an inessential complication" to a "scalpel-like" probe whose path is "strewn with the wreckage of discarded theories" [1]. With such a reputation, it is a wonder anyone would want to study spin. Nevertheless, the brave (or, perhaps, deranged) souls willing to take up such a study have illuminated intriguing ways to test leading theories. Galvanized by the influx of polarized data, hope of answering some of the questions remains alive.

## A. Measurement History

By the mid-1970's, fixed-target experiments studied transverse spin-effects by means of inclusive production from strong interactions at center-of-mass energies, $\sqrt{s} < 5$ GeV [2]. Among the listed motivations was tantalizing insight into particle wave functions. While cross-sections, $d\sigma$, provide access to the modulus of the wave function amplitudes, the transverse single-spin asymmetry,

$$A_N = \frac{d\sigma^{\uparrow} - d\sigma^{\downarrow}}{d\sigma^{\uparrow} + d\sigma^{\downarrow}}, \tag{1.1}$$

provides access to interference terms, depending directly on "spin-flip" and "non-flip" amplitudes and their relative phases (see eq. 2.26). Here, $d\sigma^{\uparrow(\downarrow)}$ denotes the cross section for spin-up(down) beam or target polarization.

In a 1978 publication, Kane, Pumplin, and Repko proposed transverse polarization effects as a significant test of Quantum Chromodynamics (QCD) and its pertur-

---

The journal model is *Physical Review D*.

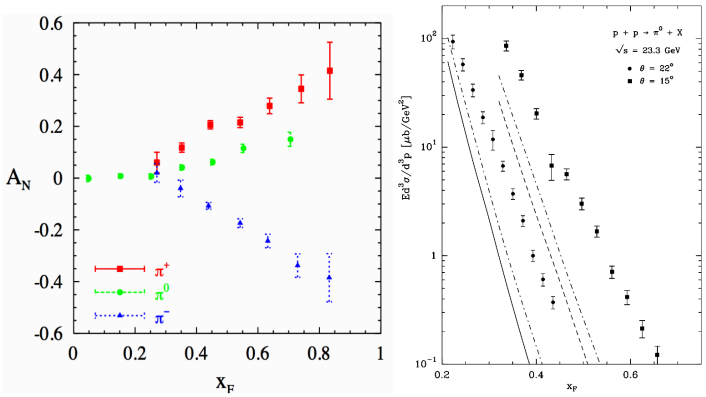


(a) (b)

Fig. 1.: (a) Analyzing powers for inclusive charged and neutral pions at $\sqrt{s} = 19.4$ GeV, as measured by FNAL-E704 [6]. (b) Measured and pQCD-predicted cross sections for inclusive $\pi^0$ production at $\sqrt{s} = 23.3$ GeV [7]. The measured cross sections are significantly enhanced relative to predictions.

bative assumptions at high transverse momentum ($p_T$) [3]. Perturbative QCD states that measured cross sections depend directly upon partonic cross-sections. Since, to first order, the partons are massless, and thus, conserve chirality, first-order helicity-flip amplitudes are zero. Beyond the first order, Kane, Pumplin, and Repko demonstrated that collinear pQCD predicts a vanishing asymmetry, $\hat{a}_N \propto \alpha_s m_q/\sqrt{s}$. Quite boldly, they stated, "the QCD prediction would be contradicted by observing large polarization effects."

By 1980 large $\pi^0$ asymmetries had been observed up to $p_T = 2.5$ GeV/$c$ from hadron collisions at $\sqrt{s} = 6.8$ GeV [4]. Antille et al. cautioned that the high-$p_T$ $\pi^0$'s were produced near the kinematic limit and that observed spin effects may be the result of something other than hard scattering. Nearly ten years later, Serpukhov reported large inclusive $\pi^0$ asymmetries up to $p_T = 3.2$ GeV/$c$ from $\pi^- + p^\uparrow$ collisions at $\sqrt{s} = 8.8$ GeV [5]. Their concluding statement proclaimed, "The epoch

of hard scattering models with trivial noncoherent dynamics is over in the quark phenomenology."

Into the 1990's, FNAL-E704 extended $p^{\uparrow} + p$ measurements out to $\sqrt{s} = 19.4$ GeV for charged and neutral pion production [6], reporting large asymmetries when the pion contains a high fraction of the maximum longitudinal momentum, which we denote $x_F = 2p_z/\sqrt{s}$. For example, E704 reported $A_N \sim \pm 0.4$ at $x_F \sim 0.8$ for $\pi^{\pm}$ (Fig. 1a). While on the surface this might seem to contradict the predictions of pQCD, cross-section measurements tell a different story. Bourrely and Soffer reported that cross sections for the E704 kinematic region are enhanced, relative to the collinear pQCD prediction, by up to an order of magnitude [7] (Fig. 1b). This opens reasonable questions about the applicability of pQCD in this kinematic region. It is also worth noting that E704 recognized that pQCD calculations may not apply in the kinematics of the 1991 publications.

Most recently, RHIC experiments reported $A_N$ for inclusive hadron production, this time, from a polarized-proton collider. STAR reported the first results from the RHIC spin program showing large asymmetries for inclusive $\pi^0$ production at forward scattering angles from polarized-proton collisions at $\sqrt{s} = 200$ GeV [8]. Further STAR measurements show these asymmetries persist at increasing transverse momentum and fixed $x_F$ [9]. BRAHMS reported large charged hadron asymmetries at $\sqrt{s} = 62.4$ GeV [10], and PHENIX [11] reported $\pi^0$ and charged hadron asymmetries consistent with zero at mid-rapidity for $\sqrt{s} = 200$ GeV across the range of $0.5 < p_T < 5.0$ GeV/$c$.

The size of the forward asymmetries is similar to those reported from E704 [6] across the same region of $x_F$ (Fig. 2a). However, unlike the FNAL-E704 case, forward $\pi^0$ cross sections at RHIC energies are in general agreement with collinear pQCD theory predictions [12] (Fig. 2b). This suggests if one wants to study the role

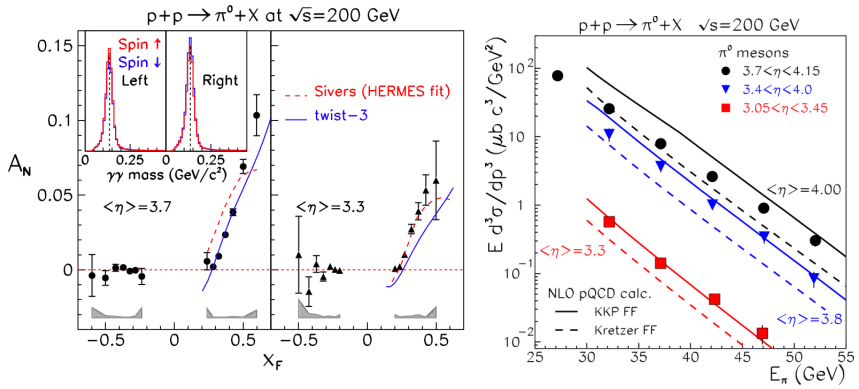


(a) (b)

Fig. 2.: (a) Analyzing powers [9] and (b) cross-sections [12] for inclusive-$\pi^0$ production at $\sqrt{s} = 200$ GeV. Measured cross-sections are in relative agreement with pQCD predictions.

of pQCD in large transverse single-spin asymmetries, clearly, the kinematic region of the STAR data is prime real estate.

## B. Non-zero Asymmetries and Transverse Momentum

Leader provides a simple way to visualize where the measured non-zero asymmetry may arise [13]. To calculate the polarized cross section one needs to consider the quark number densities, partonic cross sections, and fragmentation functions. The number densities, $f$, describe the probability to find within a parent hadron a quark with certain momentum fraction, $x$, of the parent hadron. The partonic cross sections, $\hat{\sigma}$, relate to the probability for a certain scattering process to occur. The fragmentation functions, $D$, describe the probability for a quark to fragment into a particular hadron with certain momentum fraction, $z$, of the scattered quark. For the reaction $A^{\uparrow(\downarrow)} + B \rightarrow C + X$, with $A$ and $B$ colliding along the $z$-axis and $A$ polarized along the

$y$-axis, assuming unit polarization transfer for simplicity, one can write

$$\begin{aligned} d\sigma^{\uparrow} &\sim f^{\uparrow}\left(a^{\uparrow}\right)\hat{\sigma}^{\uparrow}D\left(c^{\uparrow}\right) + f^{\uparrow}\left(a^{\downarrow}\right)\hat{\sigma}^{\downarrow}D\left(c^{\downarrow}\right) \\ d\sigma^{\downarrow} &\sim f^{\downarrow}\left(a^{\uparrow}\right)\hat{\sigma}^{\uparrow}D\left(c^{\uparrow}\right) + f^{\downarrow}\left(a^{\downarrow}\right)\hat{\sigma}^{\downarrow}D\left(c^{\downarrow}\right). \end{aligned} \tag{1.2}$$

Here, $f^{\uparrow}\left(a^{\uparrow}\right)$ and $f^{\uparrow}\left(a^{\downarrow}\right)$ are the number densities of quarks polarized up and down, respectively, in $A^{\uparrow}$; $\hat{\sigma}^{\uparrow(\downarrow)}$ is the cross-section for the partonic reaction $a^{\uparrow(\downarrow)} + b \rightarrow c^{\uparrow(\downarrow)} + d$; and $D(c^{\uparrow(\downarrow)})$ is the fragmentation function for parton $c$ polarized up or down. Now, to first order, $\hat{a}_N = 0$; so, one can take $\hat{\sigma}^{\uparrow} = \hat{\sigma}^{\downarrow} \equiv \hat{\sigma}$. The total quark number density in $A^{\uparrow}$ can be expressed, $f^{\uparrow} = f^{\uparrow}\left(a^{\uparrow}\right) + f^{\uparrow}\left(a^{\downarrow}\right)$. Another quantity of interest is the probability difference for quarks polarized parallel and anti-parallel to the parent hadron. This quantity is known as the transversity and can be expressed $h_1^{\uparrow} = f^{\uparrow}\left(a^{\uparrow}\right) - f^{\uparrow}\left(a^{\downarrow}\right)$. Furthermore, the unpolarized fragmentation function can be expressed, $D = \left(D(c^{\uparrow}) + D(c^{\downarrow})\right)/2$. Finally, one can define the quantity $H_1^{\perp}(c) = D\left(c^{\uparrow}\right) - D\left(c^{\downarrow}\right)$, and manipulate the expression to obtain for "spin-up" and "spin-down"

$$d\sigma^{\uparrow} \sim f^{\uparrow}\hat{\sigma}D + \frac{1}{2}h_1^{\uparrow}\hat{\sigma}H_1^{\perp}(c) \tag{1.3}$$

$$d\sigma^{\downarrow} \sim f^{\downarrow}\hat{\sigma}D + \frac{1}{2}h_1^{\downarrow}\hat{\sigma}H_1^{\perp}(c). \tag{1.4}$$

Therefore, the asymmetry can be expressed

$$\begin{aligned} A_N &= \frac{d\sigma^{\uparrow} - d\sigma^{\downarrow}}{d\sigma^{\uparrow} + d\sigma^{\downarrow}} \\ &\sim \frac{1}{2d\sigma}\left[\left(f^{\uparrow} - f^{\downarrow}\right)\hat{\sigma}D \right. \\ &\quad \left. + \frac{1}{2}\left(h_1^{\uparrow} - h_1^{\downarrow}\right)\hat{\sigma}H_1^{\perp}(c)\right]. \end{aligned} \tag{1.5}$$

Now, because of rotational invariance $f^{\uparrow}\left(a^{\uparrow}\right) = f^{\downarrow}\left(a^{\downarrow}\right)$, $f^{\uparrow}\left(a^{\downarrow}\right) = f^{\downarrow}\left(a^{\uparrow}\right)$, and, therefore, $h_1^{\uparrow} = -h_1^{\downarrow} \equiv h_1$. The final expression, then, is

$$A_N \sim \frac{1}{2d\sigma}\left[\tilde{\Delta}_N f \hat{\sigma} D + h_1 \hat{\sigma} H_1^{\perp}(c)\right]. \tag{1.6}$$

Leader's approach makes it clear, a transverse single-spin asymmetry may arise from two basic terms: one which depends on number densities, or parton distribution functions (PDF's), and one which depends on fragmentation functions. In the collinear parton model, $\tilde{\Delta}_N f = f^{\uparrow} - f^{\downarrow} = 0$, as there can be no difference in the number of partons with momentum fraction $x$ when the parent hadron is polarized up versus down. Likewise, when parton $c$ fragments collinearly, $H_1^{\perp} = D(c^{\uparrow}) - D(c^{\downarrow}) = 0$, as there can be no difference in the production of hadrons with momentum fraction $z$ when $c$ is polarized up versus down. Two leading theories address this situation with transverse momentum dependence (TMD).

Ordinarily, for such a reaction as $A + B \rightarrow C + X$ with respective partons $a$, $b$, $c$, and $d$, one considers cross sections

$$\begin{aligned} E_C \frac{d\sigma^{AB\rightarrow CX}}{d^3\vec{p}_C} &= \sum_{a,b,c,d} \int dx_a dx_b dz f_{a/A}\left(x_a, Q^2\right) f_{b/B}\left(x_b, Q^2\right) \\ &\quad \times \frac{d\hat{\sigma}^{ab\rightarrow cd}}{d\hat{t}} \frac{\hat{s}}{\pi z^2} \delta\left(\hat{s} + \hat{t} + \hat{u}\right) D_{C/c}\left(z, Q^2\right), \end{aligned} \tag{1.7}$$

where $f_{a/A}$ and $f_{b/B}$ denote the PDF's for $a$ and $b$ in nucleons $A$ and $B$, $D_{C/c}$ denotes the fragmentation function for parton $c$ into hadron $C$, and $Q^2$ is the scale at which the factorization of the cross-section into perturbative and non-perturbative parts is valid. In this case, the scale is taken to correspond to the momentum transfer, i.e. $Q^2 = -q^2$. However, these expressions do not explicitly consider intrinsic transverse momentum effects, which have been integrated up to $Q^2$. In general, one can write

[14]

$$E_C \frac{d\sigma^{AB\to CX}}{d^3\vec{p}_C} = \sum_{a,b,c,d} \int dx_a d^2\vec{k}_{\perp a} dx_b d^2\vec{k}_{\perp b} dz d^3\vec{k}_C \delta\left(\vec{k}_C \cdot \hat{p}_c\right) \hat{f}_{a/A}\left(x_a, \vec{k}_{\perp a}, Q^2\right) \times \hat{f}_{b/B}\left(x_b, \vec{k}_{\perp b}, Q^2\right) \frac{\hat{s}}{x_a x_b s} \frac{d\hat{\sigma}^{ab\to cd}}{d\hat{t}}\left(x_a, x_b, \hat{s}, \hat{t}, \hat{u}\right) \frac{\hat{s}}{\pi} \times \delta\left(\hat{s} + \hat{t} + \hat{u}\right) \frac{1}{z^2} J\left(z, |\vec{k}_C|\right) \hat{D}_{C/c}\left(z, \vec{k}_C, Q^2\right), \quad (1.8)$$

where $J\left(z, |\vec{k}_C|\right)/z^2$ is the proper invariant Jacobian factor for transforming from the parton momentum to the hadron momentum with the inclusion of transverse momentum effects. From this starting point are proposed two mechanisms from which the asymmetry could arise.

## C. Sivers and Collins Mechanism

The Sivers mechanism [15] is a model, where the transverse momentum ($k_\perp$) dependence of the PDF is correlated with the spin of the parent hadron, i.e.

$$f^\uparrow(x, k_\perp) = f(x, k_\perp) + \frac{1}{2}\tilde{\Delta}_N f^\uparrow(x, k_\perp)\hat{\mathcal{P}} \cdot \left(\hat{p} \times \hat{k}_\perp\right), \quad (1.9)$$

where, $\hat{\mathcal{P}}$ and $\hat{p}$ are the polarization and momentum direction, respectively, of the hadron. Isolating the PDF contribution to the asymmetry, one can consider

$$E_C \frac{d\sigma^\uparrow}{d^3\vec{p}_C} - E_C \frac{d\sigma^\downarrow}{d^3\vec{p}_C} = \sum_{a,b,c,d} \int dx_a d^2\vec{k}_{\perp a} dx_b d^2\vec{k}_{\perp b} dz d^3\vec{k}_C \delta\left(\vec{k}_C \cdot \hat{p}_c\right) \tilde{\Delta}_N \hat{f}^\uparrow_{a/A}\left(x_a, \vec{k}_{\perp a}, Q^2\right) \times \hat{f}_{b/B}\left(x_b, \vec{k}_{\perp b}, Q^2\right) \frac{\hat{s}}{x_a x_b s} \frac{d\hat{\sigma}^{ab\to cd}}{d\hat{t}}\left(x_a, x_b, \hat{s}, \hat{t}, \hat{u}\right) \frac{\hat{s}}{\pi} \times \delta\left(\hat{s} + \hat{t} + \hat{u}\right) \frac{1}{z^2} J\left(z, |\vec{k}_C|\right) \hat{D}_{C/c}\left(z, \vec{k}_C, Q^2\right). \quad (1.10)$$

If $\phi_{\mathcal{P}}$ and $\phi_{k_\perp}$ are, respectively, the azimuthal angles around $\hat{p}$ of $\hat{\mathcal{P}}$ and $\hat{k}_\perp$, then one can write

$$\begin{aligned}\tilde{\Delta}_N f\left(x, k_\perp\right) &= f^{\uparrow}\left(x, k_\perp\right) - f^{\downarrow}\left(x, k_\perp\right) \\ &= \tilde{\Delta}_N f^{\uparrow}\left(x, k_\perp\right) \hat{\mathcal{P}} \cdot \left(\hat{p} \times \hat{k}_\perp\right) \\ &= \tilde{\Delta}_N f^{\uparrow}\left(x, k_\perp\right) \sin\left(\phi_{\mathcal{P}} - \phi_{k_\perp}\right). \end{aligned} \tag{1.11}$$

Thus, the $k_\perp$ dependence produces an asymmetry in the PDF. The scattering of the asymmetrically distributed partons could then result in an azimuthal asymmetry in production of the jet or final-state hadron.

The Collins mechanism [16], on the other hand, considers the transverse momentum dependence of the fragmentation of a polarized scattered parton, $c$, into a hadron, $C$,

$$D\left(\vec{\mathcal{P}}_c; z, \vec{k}_{\perp C}\right) = D\left(z, k_{\perp C}\right) + \frac{1}{2}\Delta D\left(z, k_{\perp C}\right) \vec{\mathcal{P}}_c \cdot \left(\hat{p}_c \times \hat{k}_{\perp C}\right). \tag{1.12}$$

Here, $\vec{\mathcal{P}}_c$ and $\hat{p}_c$ are the polarization and momentum directions, respectively, of the scattered quark $c$; and $\hat{k}_{\perp C}$ is the transverse momentum of the final-state hadron $C$ relative to the scattered quark direction, i.e. $\hat{p}_c \cdot \hat{k}_{\perp C} = 0$. If one adopts the approach similar to Yuan [17] and only considers the explicit $\vec{k}_\perp$-dependence of the fragmentation function, the cross section can be expressed

$$\begin{aligned} E_C \frac{d\sigma^{\uparrow}}{d^3\vec{p}_C} - E_C \frac{d\sigma^{\downarrow}}{d^3\vec{p}_C} &= \sum_{a,b,c,d} \int dx_a dx_b dz d^2\vec{k}_{\perp C} h_{1a/A}\left(x_a, Q^2\right) f_{b/B}\left(x_b, Q^2\right) \\ &\quad \times \frac{d\hat{\sigma}^{ab\to cd}}{d\hat{t}} \frac{\hat{s}}{\pi z^2} \delta\left(\hat{s} + \hat{t} + \hat{u}\right) \tilde{\Delta}\hat{D}_{C/c}\left(z, k_{\perp C}, Q^2\right). \end{aligned} \tag{1.13}$$

If $\phi_{\mathcal{P}}$ and $\phi_{k_\perp}$ are, respectively, the azimuthal angles around $\hat{p}_c$ of $\hat{\mathcal{P}}_c$ and $\hat{k}_{\perp C}$, then

one can write

$$\begin{aligned}\tilde{\Delta}\hat{D}_{C/c}\left(z,k_{\perp C},Q^2\right) &= \Delta\hat{D}_{C/c}\left(z,k_{\perp C},Q^2\right)\vec{\mathcal{P}}_c\cdot\left(\hat{p}_c\times\hat{k}_{\perp C}\right)\\ &= \Delta\hat{D}_{C/c}\left(z,k_{\perp C},Q^2\right)|\vec{\mathcal{P}}_c|\sin\left(\phi_{\mathcal{P}}-\phi_{k_\perp}\right). \qquad (1.14)\end{aligned}$$

Thus, the Collins mechanism produces an azimuthal asymmetry in the fragmenting hadrons about the jet axis. Furthermore, it is clear an essential part of the asymmetry depends on the transfer of polarization from the incident parton to the scattered parton, i.e. $\hat{\mathcal{P}}_a \rightarrow \hat{\mathcal{P}}_c$. This can be calculated from the spin-transfer parameter, $\hat{d}_{TT}\left(\theta^*\right)$ [13] (Eqs. 2.33, 2.34, 2.35), which describes how much of the initial polarization normal to the beam is transferred through the collision to the outgoing parton in a direction normal to its momentum. For the relevant partonic subprocesses, as $\cos\theta^* \rightarrow 1$, $\hat{d}_{TT} \rightarrow 1$, (Fig. 3). This leads one to expect a larger Collins Effect in the forward kinematic region.

The scattered polarization can be expressed in the partonic center of mass [13]

$$\mathcal{P}_c^x = \hat{d}_{TT}\left(\theta^*\right)\sin\phi^*\cos\phi^*\left(\cos\theta^*-1\right) \qquad (1.15)$$

$$\mathcal{P}_c^y = \hat{d}_{TT}\left(\theta^*\right)\left(\sin^2\phi^*\cos\theta^*+\cos^2\phi^*\right) \qquad (1.16)$$

$$\mathcal{P}_c^z = -\hat{d}_{TT}\left(\theta^*\right)\sin\phi^*\sin\theta^*. \qquad (1.17)$$

One finds

$$\begin{aligned}\tilde{\Delta}\hat{D}_{C/c}\left(z,k_{\perp C},Q^2\right) &= \Delta\hat{D}_{C/c}\left(z,k_{\perp C},Q^2\right)|\vec{\mathcal{P}}_c|\sin\left(\phi_{\mathcal{P}}-\phi_{k_\perp}\right)\\ &= \Delta\hat{D}_{C/c}\left(z,k_{\perp C},Q^2\right)\hat{d}_{TT}\left(\theta^*\right)\sin\left(\phi_{\mathcal{P}}-\phi_{k_\perp}\right), \qquad (1.18)\end{aligned}$$

and, thus,

$$E_C\frac{d\sigma^\uparrow}{d^3\vec{p}_C}-E_C\frac{d\sigma^\downarrow}{d^3\vec{p}_C}$$

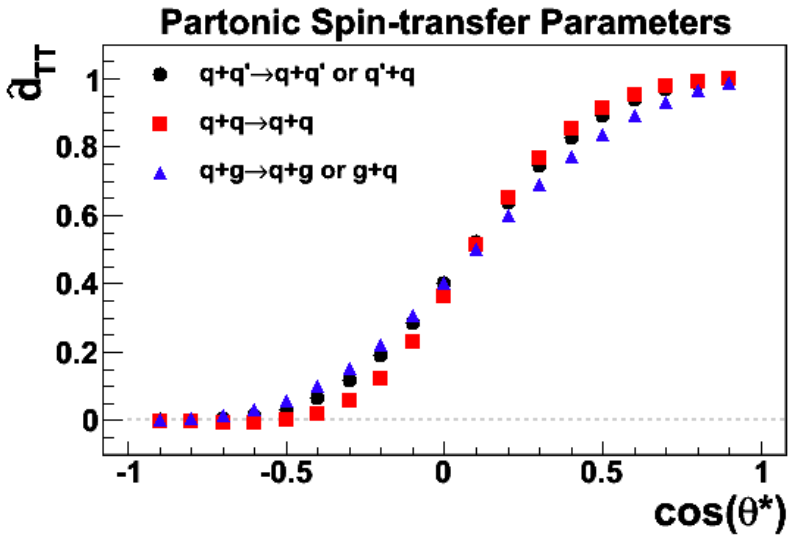


Fig. 3.: Partonic spin-transfer parameters, $\hat{d}_{TT}$, for the relevant subprocesses. Clearly, $\hat{d}_{TT}$ approaches unity as $\cos\theta^*$ approaces unity.

$$= \sum_{a,b,c,d} \int dx_a dx_b dz d^2\vec{k}_{\perp C} \frac{\hat{s}}{\pi z^2} \delta\left(\hat{s}+\hat{t}+\hat{u}\right) f_{b/B}\left(x_b, Q^2\right) h_{1a/A}\left(x_a, Q^2\right)$$
$$\times \Delta\hat{D}_{C/c}\left(z, k_{\perp C}, Q^2\right) \hat{d}_{TT}\left(\theta^*\right) \frac{d\hat{\sigma}^{ab\to cd}}{d\hat{t}} \sin\left(\phi_{\mathcal{P}} - \phi_{k_\perp}\right). \quad (1.19)$$

The key component of the Sivers effect is the correlation between the polarization of the initial parent hadron and the transverse momentum of the unpolarized internal parton, which can be either a quark or a gluon. Such a mechanism would provide an indirect signature of parton orbital motion [18]. For the Collins effect, the key component is the correlation between the scattered quark polarization and the transverse momentum of the fragmenting hadron. One should note that a nonzero Collins mechanism provides access to constrain the transversity, $h_1$. As gluons cannot have transverse polarization, there is no transversity or Collins function for gluons. Thus, both mechanisms provide access to critical internal structure information.

## D. Deciphering Mechanisms

The history of the Collins and Sivers mechanisms is a bit tumultuous, with both ideas experiencing various levels of disfavor. Initially, it was suggested that the Sivers mechanism was non-physical based on time-reversal symmetry [16]. This was, later, shown to be false, based on the inclusion of Wilson lines in the parton density operators; and the Sivers mechanism was welcomed out of exile [18, 19]. Later, calculations seemed to predict that the Collins mechanism was suppressed for the inclusive pion production shown in the STAR data [20]. It was discovered that a sign error in the gluon-Compton channel was responsible for the apparent suppression [17, 21]. For the time being, there is no reason to assume either mechanism would not contribute significantly to the large asymmetries. A remaining challenge is to disentangle these contributions. Success would provide insight on proton spin structure, namely, parton orbital motion and transversity. The question, then, is how to separate the Sivers and Collins contributions to non-zero $A_N$.

Much work has been devoted to studying the Sivers and Collins contributions to semi-inclusive deep inelastic scattering (SIDIS). As discussed in Ref. [22], the mechanisms can be distinguished from the process $l + p^{\uparrow} \rightarrow l^{'} + h + X$, where $l$ and $l^{'}$ denote the incident and scattered leptons, respectively, and $h$ denotes the measured hadron, by considering the various moments of the single-spin asymmetry. The moments involve two angles: $\phi_S$, which denotes the azimuthal angle of the nucleon spin polarization, and $\phi_h$, which denotes the azimuthal angle of the hadron, each measured relative to the lepton plane. By considering the $\sin(\phi_S + \phi_h)$ moment, the Collins effect is isolated. On the other hand, by considering the $\sin(\phi_S - \phi_h)$ moment, the Sivers effect is isolated.

For hadron-hardron collisions, one must turn to different measurements to dis-

entangle the Sivers and Collins effects [23]. The Sivers mechanism is an initial state effect, resulting in a left-right asymmetry in jet production. On the other hand, the Collins mechanism is a final state effect, contributing an asymmetry in the hadron fragmentation around the jet axis. If one can move beyond an inclusive pion analysis to a full jet analysis, one can separate the Sivers and Collins contributions to the asymmetries from hadron-hadron collisions. The STAR data [9, 12] could provide an opportunity to investigate jets in a region where not only are inclusive hadron asymmetries sizable, but also observed cross-sections are in reasonable agreement with collinear pQCD predictions. Furthermore, this kinematic region is also where one would expect the Collins effect to be maximal, due to the limit $\hat{d}_{TT} \rightarrow 1$ as $\cos\theta^* \rightarrow 1$.

Additionally, effort has been devoted to developing a generalization of the collinear framework by looking at higher-order calculations [24]. This approach utilizes a series of higher-order quark-gluon correlations and a class of universal non-perturbative, "twist-3" quark-gluon distribution and fragmentation functions. This so-called "twist-3" approach is able to predict large-$x_F$ asymmetries like those found in the STAR data [25]. As a higher-order effect, however, the predicted asymmetry is suppressed at high-$p_T$, which is not seen in the data [9]. The twist-3 approach and the transverse momentum-dependent (TMD) Sivers and Collins approaches are suited for separate kinematic regions. The twist-3 approach is robust with large $k_T$, while the TMD approach is suited for low $k_T$. As it turns out, the two approaches are unified in the overlapping region of intermediate $k_T$ [26].

Factorization theorems are difficult for TMD approaches and efforts to prove factorization for hadronic interactions are on-going [27, 28]. Factorization violation would imply non-universality of the Collins and Sivers functions. For SIDIS, factorization for both the TMD and twist-3 approaches has been proven [29]. Yuan has

argued in Ref. [30] that the Collins mechanism is, indeed, universal between SIDIS and hadronic interactions. On the other hand, it is argued the Sivers mechanism is process-dependent [19, 31], e.g. exhibiting a sign-flip between SIDIS and Drell-Yan Sivers asymmetries. Thus, disentangling the Sivers and Collins contributions in hadronic interactions is further interesting as a tool for testing the universality of the effects between the various types of interactions.

### E. Extractions and Predictions from SIDIS

In SIDIS the bulk of work on the Sivers and Collins effects has been carried out by the HERMES [32] and COMPASS experiments [33] examining both charged and neutral pion asymmetries. In addition, the BELLE collaboration has measured asymmetries in di-hadron correlations from $e^+ + e^- \rightarrow \pi^+ + \pi^- + X$ where the pions are measured in separate hemispheres [34]. As a fully electromagnetic process, calculations are free from scale ambiguities found in QCD processes. The polarizations of the outgoing quarks can be calculated absolutely and related to the convolution of quark and antiquark Collins functions. In addition, since initial nucleons are absent, these asymmetries decouple the Collins functions from transversity. Thus, by combining the HERMES and COMPASS measurements with the BELLE measurements, it is possible to isolate and extract the Sivers and Collins functions, as well as the transversity distributions.

Anselmino and company have provided one example of a method to carry out numerical predictions for the Sivers effect [35]. First, they assume the Sivers function, $\tilde{\Delta}_N f\left(x, k_\perp\right)$, can be factorized in the form

$$\tilde{\Delta}_N f^{\uparrow}_{q/p}\left(x, k_\perp\right) = 2\mathcal{N}_q\left(x\right) f_{q/p}\left(x, k_\perp\right) h\left(k_\perp\right), \tag{1.20}$$

with functional forms

$$\mathcal{N}_q(x) = N_q x^{a_q}(1-x)^{b_q}\frac{(a_q+b_q)^{(a_q+b_q)}}{a_q^{a_q}b_q^{b_q}} \quad (1.21)$$

$$h(k_\perp) = \sqrt{2e}\frac{k_\perp}{M_1}e^{-k_\perp^2/M_1^2}. \quad (1.22)$$

$N_q$, $a_q$, $b_q$, and $M_1$ are free parameters determined by fits to the data, and $|N_q| \leq 1$ and $h \leq 1$ to enforce the positivity bound for the Sivers function. Finally, they assert that the unpolarized distributions and fragmentation functions can be factorized with Gaussian form

$$f_{q/p}(x,k_\perp) = f_q(x)\frac{1}{\pi\langle k_\perp^2\rangle}e^{-k_\perp^2/\langle k_\perp^2\rangle} \quad (1.23)$$

$$D_{h/q}(z,p_T) = D_{h/q}(z)\frac{1}{\pi\langle p_T^2\rangle}e^{-p_T^2/\langle p_T^2\rangle}, \quad (1.24)$$

with $\langle k_\perp^2\rangle = 0.25$ (GeV/c)$^2$ and $\langle p_T^2\rangle = 0.20$ (GeV/c)$^2$ from analyzing the Cahn effect in SIDIS [36]. Anselmino and company consider the contributions of up, down, and strange quarks; utilize the set of fragmentation functions from de Florian, Sassot, and Stratmann (DSS) [37]; and utilize PDF's from GRV98LO [38] (they note that repeating the fit with the MRST01LO set of PDF's [39] leads to such negligible changes that the two fits are quite indistinguishable).

By tuning the free parameters to the HERMES and COMPASS data (Fig. 4), Anselmino and company are able to extract the Sivers functions for up, down, and strange quarks (Fig. 5a). These functions, then, may be used in a prediction for hadronic interactions at RHIC kinematics [21, 40]. While, the Anselmio prediction is consistent with the observed STAR data [9] (Fig. 5b), the limited kinematic coverage of the SIDIS data leads to rather sizable uncertainties at the STAR kinematics. Furthermore, Anselmino points out that the prediction is also limited by simplifying assumptions made to reduce the number of free parameters [21]. D'Alesio and com-

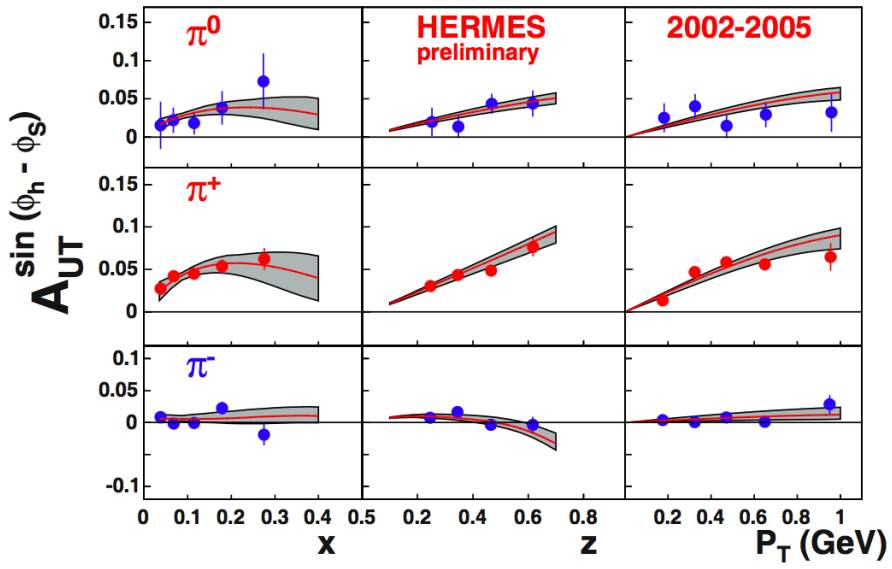


(a)

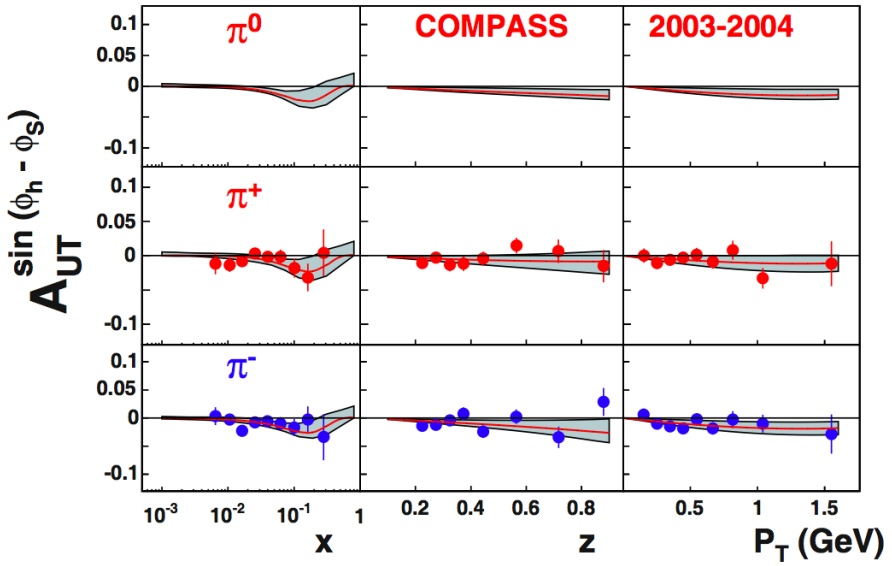


(b)

Fig. 4.: Sivers asymmetries from SIDIS measured by (a) HERMES [32] on a polarized hydrogen target and (b) COMPASS [33] on a polarized $^6$LiD target. The solid lines reflect the results of the Anselmino fit [35] to the SIDIS data with the shaded area corresponding to the statistical uncertainty of the parameters.

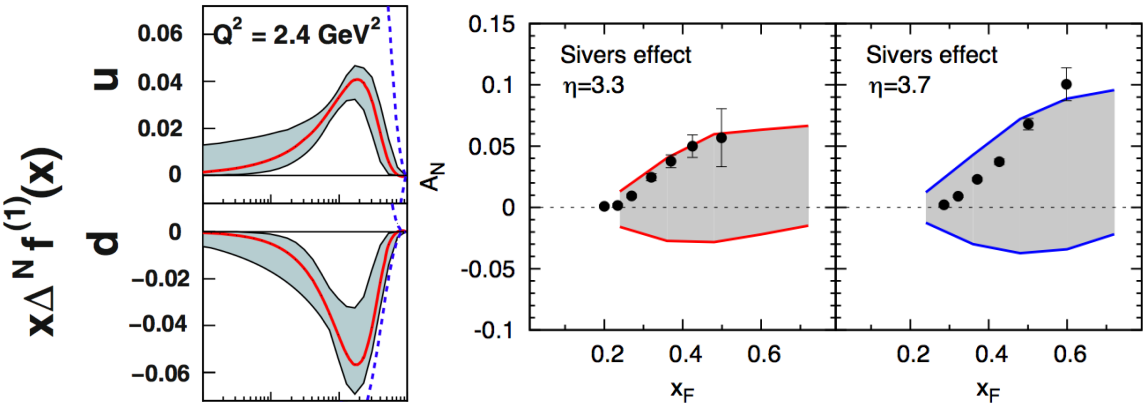


(a) (b)

Fig. 5.: (a) The first moment of the Sivers function from the Anselmino fit [35] to SIDIS data [32, 33]. The distribution is shown for up and down quark flavors at the evolution scale $Q^2 = 2.4$ (GeV/c)$^2$. The blue dashed lines indicate the positivity bound. (b) This extraction is applied to the STAR data [21, 40]. The band reflects fit uncertainties by varying the parameters found in Eqs. 1.21 and 1.22.

pany, also, demonstrate the maximized Sivers contribution for $p^{\uparrow} + p \rightarrow \text{jet} + \pi + X$ can be quite sizable [23].

Anselmino and company have also provided an example of how to carry out numerical calculations for the Collins effect [41]. Much like the Sivers case [35], they propose a factorized form for the transversity distribution and Collins function

$$h_{1q/p}(x, k_\perp) = \frac{1}{2}\mathcal{N}_q^T\left[f_{q/p}(x) + \Delta q(x)\right]\frac{e^{-k_\perp^2/\langle k_\perp^2\rangle_T}}{\pi\langle k_\perp^2\rangle_T} \tag{1.25}$$

$$\Delta\hat{D}_{h/q}(z, p_T) = 2\mathcal{N}_q^C D_{h/q}(z, p_T)\, h(p_T), \tag{1.26}$$

where $f_{q/p}(x, k_\perp)$ and $D_{h/q}(z, p_T)$ are have Gaussian factorization as in Eqs. 1.23 and 1.24. They take the helicity distributions, $\Delta q$, from Ref. [42] and, again, utilize the DSS fragmentation functions [37] and GRV98LO PDF's [38]. In analogy to the Sivers

case, Anselmino and company choose functional forms of

$$\mathcal{N}_q^T(x) = N_q^T x^{\alpha_q}(1-x)^{\beta_q}\frac{(\alpha_q+\beta_q)^{(\alpha_q+\beta_q)}}{\alpha_q^{\alpha_q}\beta_q^{\beta_q}} \quad (1.27)$$

$$\mathcal{N}_q^C(x) = N_q^C z^{\gamma_q}(1-z)^{\delta_q}\frac{(\gamma_q+\delta_q)^{(\gamma_q+\delta_q)}}{\gamma_q^{\gamma_q}\delta_q^{\delta_q}} \quad (1.28)$$

$$h(p_T) = \sqrt{2e}\frac{p_T}{M_h}e^{-p_T^2/M_h^2}, \quad (1.29)$$

with $-1 \leq N_q^T \leq 1$, $-1 \leq N_q^C \leq 1$, and $\langle k_\perp^2\rangle_T = \langle k_\perp^2\rangle$.

By tuning the free parameters to the HERMES, COMPASS, and BELLE datasets (Fig. 6), Anselmino and company can extract both the Collins fragmentation function and transversity distributions (Fig. 7a). As with the Sivers case, these functions can then be used to predict asymmetries for hadronic interactions at RHIC kinematics. One such example is shown in Fig. 7b. Again, such a fit suffers from large uncertainties for the STAR kinematics as well as strong dependence on simplifying assumptions to reduce the number of free parameters. Again, D'Alesio and company show that for RHIC kinematics, the maximized Collins contributions to $p^\uparrow + p \rightarrow \text{jet} + \pi + X$ can be quite sizable [23].

### F. A Third Option: Interference Fragmentation Functions

Ideally, then, one could consider reconstructing full jets in the kinematic region of the STAR asymmetries. Unfortunately, this is not always feasible, given detector constraints. In light of experimental realities, one can also consider the production of two hadrons within a jet [44, 45, 46], for example the coincidence of neutral and charged pions. Instead of considering correlations of the type

$$\vec{S}_T \cdot \left(\vec{k} \times \vec{P}_h\right), \quad (1.30)$$

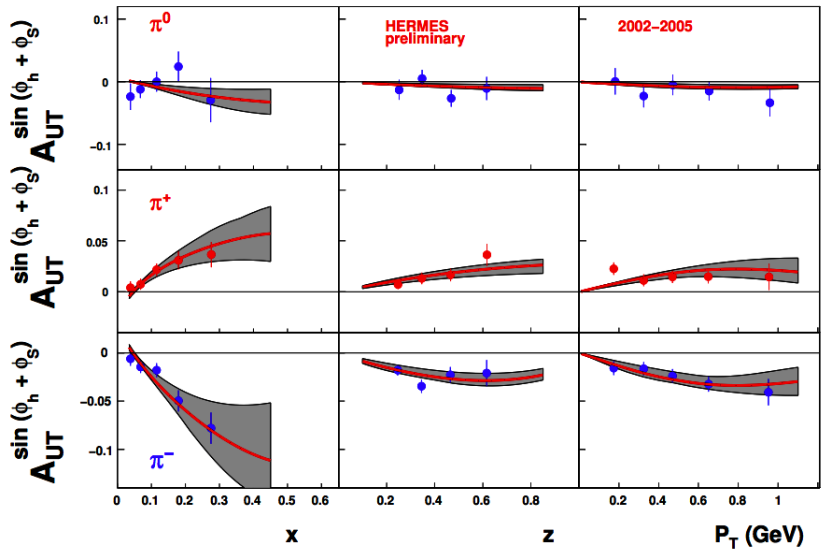


(a)

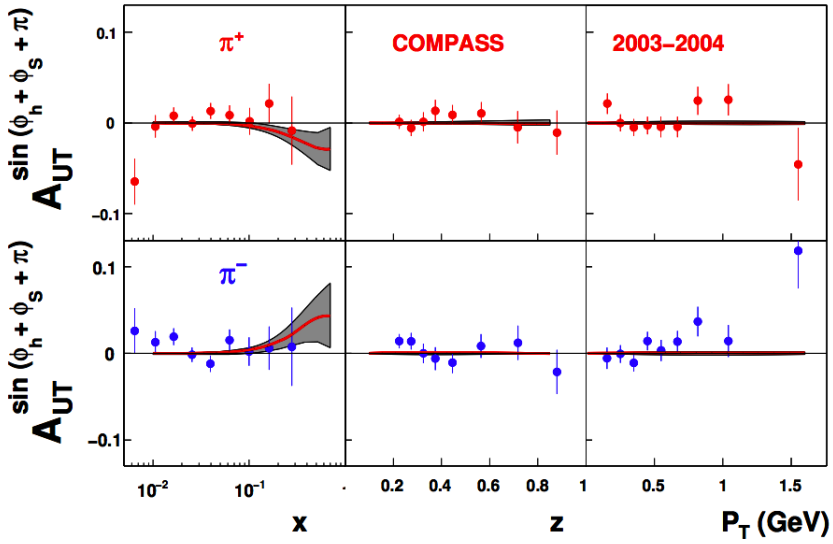


(b)

Fig. 6.: Collins asymmetries from SIDIS measured by (a) HERMES [32] on a polarized hydrogen target and (b) COMPASS [33] on a polarized $^6$LiD target. The solid lines reflect the results of the Anselmino fit [41] to the SIDIS data with the shaded area corresponding to the statistical uncertainty of the parameters. Note that HERMES and COMPASS utilize different conventions introducing a sign flip between the two.

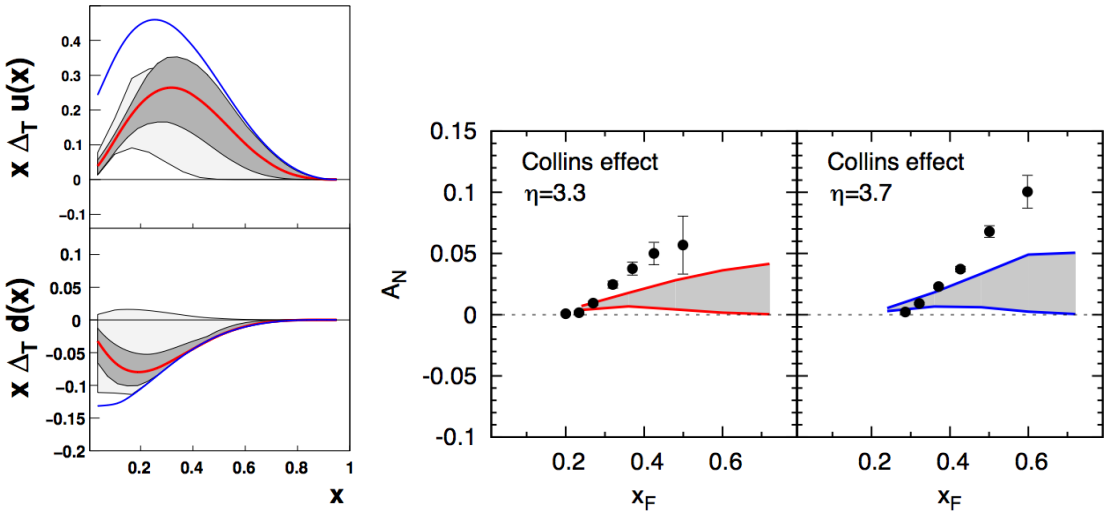


(a) (b)

Fig. 7.: (a) The transversity function from the Anselmino fit [41] to SIDIS data [32, 33]. The distribution is shown for up and down quark flavors at the evolution scale $Q^2 = 2.4$ (GeV/c)$^2$. The blue lines indicate the positivity bound described by Soffer [43]. (b) This extraction is applied to the STAR data [21, 40]. The band reflects fit uncertainties by varying the parameters found in Eqs. 1.27 and 1.29.

where $\vec{S}_T$ is the polarization of the fragmenting quark, $\vec{k}$ is the quark momentum, and $\vec{P}_h$ is the hadron momentum, one can consider correlations of the type

$$\vec{S}_T \cdot \left(\vec{R} \times \vec{P}_h\right), \tag{1.31}$$

where $\vec{R} = \vec{P}_1 - \vec{P}_2$ and $\vec{P}_h = \vec{P}_1 + \vec{P}_2$ with $\vec{P}_i$ the three-momentum of the produced hadrons. In this case, the asymmetry remains even in the collinear approximation.

As usual, the asymmetry for two hadrons in the same jet depends directly on the difference between the cross sections for spin "up" and spin "down." For the process $A + B^{\uparrow(\downarrow)} \to (C_1C_2)_C + X$, one can express the spin of incoming proton $B$ as $S_B$, the momentum of outgoing hadrons $C_i$ as $P_{C_i}$, the combined momentum as $P_C = P_{C_1} + P_{C_2}$, the relative momentum as $R_C = P_{C_1} - P_{C_2}$, and the invariant mass of the two-hadron system as $M_C$. Here, the approach follows that of Bacchetta and Radici [47], who switch to $A$ unpolarized and $B$ polarized. This keeps a consistency with a common approach for SIDIS, where $A$ corresponds to the virtual photon, which is taken to be unpolarized, and $B$ corresponds to the polarized target nucleon. The difference in cross sections can be expressed [47]

$$\begin{aligned} d\sigma_{UT} &= \frac{1}{2}\left(\frac{d\sigma^{\uparrow}}{d\eta_C d|\vec{P}_{C\perp}| d\cos\theta_C dM_C^2 d\phi_{R_C} d\phi_{S_B}}\right. \\ &\quad \left. -\frac{d\sigma^{\downarrow}}{d\eta_C d|\vec{P}_{C\perp}| d\cos\theta_C dM_C^2 d\phi_{R_C} d\phi_{S_B}}\right) \\ &= 2\left|\vec{P}_{C\perp}\right| \sum_{a,b,c,d} \left|\vec{S}_{BT}\right| \sin\left(\phi_{S_B} - \phi_{R_C}\right) \\ &\quad \times \int \frac{dx_a dx_b}{8\pi^2 z_c} f_1\left(x_a\right) h_1\left(x_b\right) \frac{d\Delta\hat{\sigma}_{ab^{\uparrow}\to c^{\uparrow}d}}{d\hat{t}} \frac{\left|\vec{R}_C\right|}{M_C} \sin\theta_C \\ &\quad \times H_1^{\sphericalangle_c}\left(\bar{z}_c, \cos\theta_C, M_C^2\right), \end{aligned} \tag{1.32}$$

where the azimuthal angles are defined relative to the event plane, $\eta_C$ is defined relative to $\vec{P}_A$, and $\theta_C$ is the center of mass polar angle of the hadron pair with

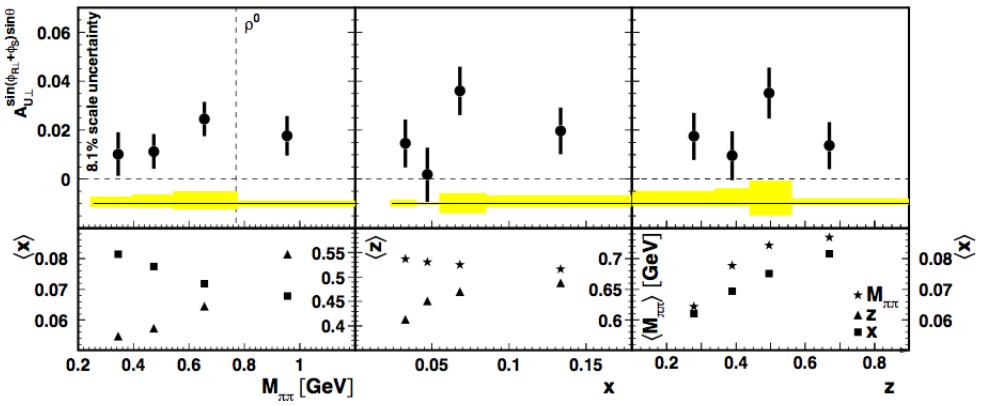


(a)

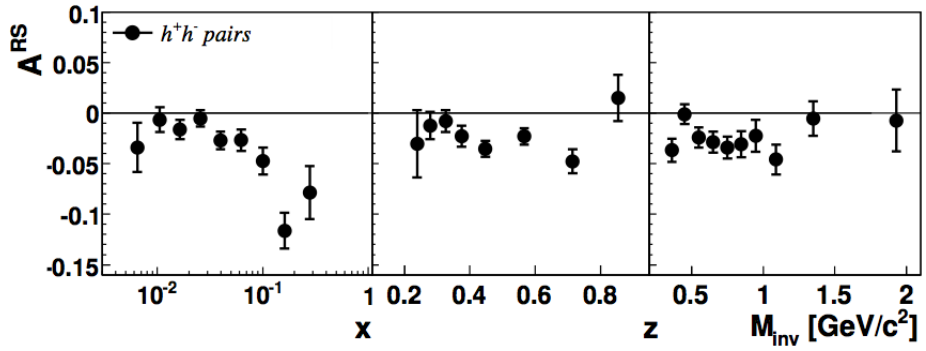


(b)

Fig. 8.: (a) HERMES data [49] and (b) COMPASS preliminary data [50] on di-hadron asymmetries from SIDIS. Note the difference in sign between the HERMES and COMPASS asymmetries. This stems from a difference in conventions of the same nature as in Fig. 6.

respect to $\vec{P}_C$ in any other frame. The partonic component can be expressed

$$\frac{d\Delta\hat{\sigma}_{ab^{\uparrow}\to c^{\uparrow}d}}{d\hat{t}} = \frac{1}{16\pi\hat{s}^2}\frac{1}{4}\sum_{(\text{all}\chi'\text{s})}\hat{M}_{\chi_c,\chi_d;\chi_a,\chi_b}\hat{M}^{*}_{\chi_a,-\chi_b;-\chi_c,\chi_d}, \tag{1.33}$$

where, here, $\hat{M}_{\chi_c,\chi_d;\chi_a,\chi_b}$ are the helicity amplitudes. The asymmetry is, then, a convolution of the transversity, $h_1$, and a new fragmentation function, $H_1^{\sphericalangle c}$.

These functions arise from the interference between various production amplitudes, so they are commonly referred to as interference fragmentation functions (IFF). For example, Collins and Ladinsky [44] have discussed the interference between two-pion production in a continuum state and a $\sigma$ resonance; while Jaffe, Jin, and Tang [46] analyzed the interference between the $s$ and $p$ wave of the two-pion system around the $\rho$ mass region. Bacchetta and Radici [47, 48] have utilized a partial wave analysis to demonstrate contributing channels. Expanding the function in terms of Legendre polynomials through the $\cos\theta_C$ dependence,

$$\begin{aligned} d\sigma_{UT} \;\approx\; & 2|\vec{P}_{C\perp}|\sum_{a,b,c,d}\left|\vec{S}_{BT}\right|\sin\left(\phi_{S_B}-\phi_{R_C}\right) \\ & \times\int\frac{dx_a dx_b}{8\pi^2 z_c}f_1\left(x_a\right)h_1\left(x_b\right)\frac{d\Delta\hat{\sigma}_{ab^{\uparrow}\to c^{\uparrow}d}}{d\hat{t}}\frac{\left|\vec{R}_C\right|}{M_C} \\ & \times\left(H_{1,ot}^{\sphericalangle c}\left(\bar{z}_c,M_C^2\right)\sin\theta_C+H_{1,lt}^{\sphericalangle c}\left(\bar{z}_c,M_C^2\right)\sin\theta_C\cos\theta_C\right). \end{aligned} \tag{1.34}$$

$H_{1,ot}^{\sphericalangle c}$ represents the interference between an $s$ wave, $L=0$, hadron pair and "transversely" polarized $p$ wave, $L=1$ pair; while $H_{1,lt}^{\sphericalangle c}$ represents the interference between a "longitudinally" polarized $p$ wave and a "transversely" polarized $p$ wave.

Recently, both HERMES [49] and COMPASS [50] have reported measurements of di-hadron asymmetries from SIDIS (Fig. 8). Much like the SIDIS Collins analysis, the IFF effect is isolated by considering moments of the single-spin asymmetry, where, essentially, $\phi_h$ is replaced by $\phi_R$. So, the moment of interest, here, for SIDIS is $\sin\left(\phi_S+\phi_R\right)$. It is noteworthy that the data do not exhibit the change in sign at the

$\rho$ mass predicted by Jaffe, Jin, and Tang [46] through relative phase shifts between the $s$ and $p$ wave channels. Again, in analogy to the Collins analysis, the transversity can be extracted by combining information from fits to the SIDIS di-hadron data, combined with fits of data from BELLE [51] (Fig. 9). Now, the BELLE data of interest involve measuring asymmetries of two sets of di-hadron pairs with one pair in each hemisphere. As in the Collins case, this process is fully electromagnetic, and outgoing quark polarization is exactly calculable. Thus, these asymmetries may be related to the convolution of quark and antiquark IFF's; and, as there is no initial-state nucleon, these IFF's are divorced from transversity. Using the fit information combined with estimations based on the MSTW08LO set of parton distribution functions [52] and assumptions based on isospin symmetry and charge conjugation, Bacchetta, Courtoy, and Radici [53] have presented the first extraction of transversity from IFF's (Fig. 10).

To date, no published di-hadron single-spin asymmetries exist from polarized proton data. However, PHENIX has presented preliminary data from 2006 and 2008 [54], which do not show significant di-hadron single-spin asymmetries at mid-rapidity ($|\eta| < 0.35$) from collisions at $\sqrt{s} = 200$ GeV. Nonetheless, it is useful to get some idea of the scale of the effects one might see from the STAR data.

If one considers a simple approximation, the asymmetry for the reaction $a + b \rightarrow c + X$ may be estimated

$$\begin{aligned} A &\sim \frac{f_b h_{1,a} d_{TT} d\sigma H_1^{\sphericalangle_c}}{f_b f_a d\sigma D_c} \\ &= \frac{h_{1,a}}{f_a} \times d_{TT} \times \frac{H_1^{\sphericalangle_c}}{D_c}, \end{aligned} \tag{1.35}$$

where $f_a$ and $f_b$ are the PDF's for $a$ and $b$, $h_{1,a}$ is the transversity for $a$, $d\sigma$ is the partonic cross section, $D_c$ is the unpolarized fragmentation function for the di-hadron

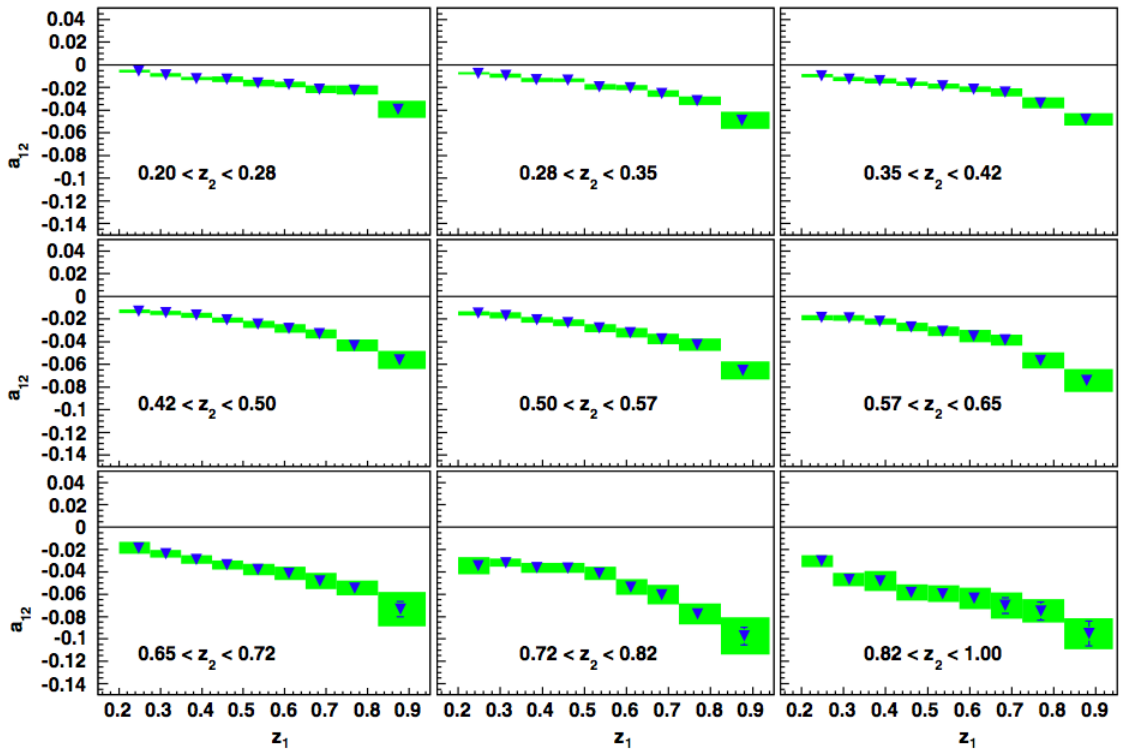


Fig. 9.: Asymmetries measured by BELLE [51] involving two sets of hadron pairs in separate hemispheres from $e^+ - e^-$ collisions. These asymmetries are void of QCD ambiguities and are interpreted as an isolation of a convolution of IFF's from transversity. Additionally, these asymmetries may be related to the ratio of the IFF to the unpolarized fragmentation function for the purposes of estimating the scale of asymmetries expected in hadronic interactions.

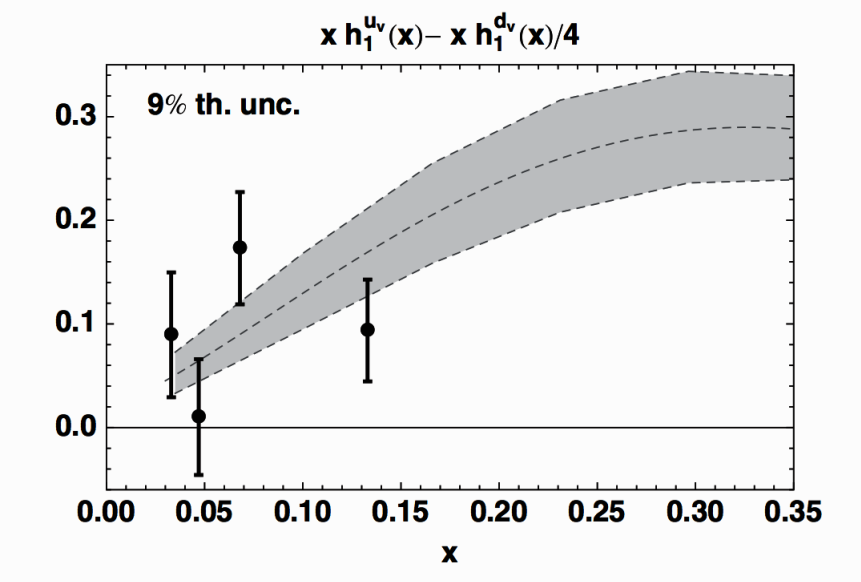


Fig. 10.: Extracted transversity by Bacchetta, et al. [53], from HERMES data [49].

decay of $c$, and $H_1^{\sphericalangle c}$ is the IFF for $c$. Now, for the forward angle production, $d_{TT} \approx 1$ is an appropriate approximation. The ratio $h_{1,a}/f_a$ can be estimated by referring to the recent Anselmino transversity extraction [41] as well as the GRV98LO set of PDF's [38] used in the transversity extraction. This analysis ultimately focuses on di-hadron correlations at $x_F \approx 0.44$ and 0.38, thus, the scale estimation should consider the values of the transversity and PDF's at these kinematics. Finally, since the scale is all that matters for this purpose, the BELLE asymmetries [51] can be interpreted as $\left(H_1^{\sphericalangle c}/D_c\right)^2$, since they involve the convolution of IFF's for the quark and antiquark.

At present, no SIDIS data exist on IFF's for $\pi^0 - \pi^{\pm}$. Since the scale is all that matters for this estimation, it is not unreasonable to expect that IFF's for $\pi^0 - \pi^{\pm}$ are on the same order as those for $\pi^+ - \pi^-$. By assuming the STAR data lie in the high-$z$ region of the BELLE data (Fig. 9), one can reasonably estimate an IFF contribution of 0.3 to the asymmetry scale. Also, at issue is which quark flavors in the transversity and PDF's correspond to the two types of hadron pairs. For such

a rough estimate it is not unreasonable to assume the up quark distributions set the scale for $\pi^0 - \pi^+$ and down quark distributions set the scale for $\pi^0 - \pi^-$. An additional issue is the appropriate evolution scale, $Q^2$, for the PDF's. For the STAR data, the kinematics imply $Q^2 \sim 10$ GeV$^2$ rather than the $Q^2 = 2.4$ GeV$^2$ for which the transversity is quoted. If one takes the values at 2.4 GeV$^2$ for consistency with the quoted transversity distribution, one can estimate a scale for IFF asymmetries at $x_{F,\mathrm{pair}} = 0.44$

$$A_{IFF}^{\pi^0-\pi^+} \sim 0.15 \tag{1.36}$$

$$A_{IFF}^{\pi^0-\pi^-} \sim -0.07, \tag{1.37}$$

and at $x_{F,\mathrm{pair}} = 0.38$

$$A_{IFF}^{\pi^0-\pi^+} \sim 0.15 \tag{1.38}$$

$$A_{IFF}^{\pi^0-\pi^-} \sim -0.08. \tag{1.39}$$

On the other hand, if one takes the PDF values at 10 GeV$^2$ and assumes the transversity evolves slowly, one can estimate at $x_{F,\mathrm{pair}} = 0.44$

$$A_{IFF}^{\pi^0-\pi^+} \sim 0.19 \tag{1.40}$$

$$A_{IFF}^{\pi^0-\pi^-} \sim -0.09. \tag{1.41}$$

and at $x_{F,\mathrm{pair}} = 0.38$

$$A_{IFF}^{\pi^0-\pi^+} \sim 0.18 \tag{1.42}$$

$$A_{IFF}^{\pi^0-\pi^-} \sim -0.10. \tag{1.43}$$

Thus, one might expect sizable IFF asymmetries for the STAR data with charge-sign dependence for pions.

# CHAPTER II

# FORMALISM

It is useful to have some idea from where the theory expressions are derived. The attempt, here, is to keep derivations appropriately concise. The approach follows that of Leader in Ref. [13].

## A. Relation of Final Spin to Initial Spin

A crucial step in any problem is to obtain an expression for the final-state system, which is to be measured, in terms of the initial-state system, which is to be controlled. For scattering problems, one typically (e.g. Ref. [55]) looks for asymptotic wave solutions, e.g.

$$\Psi \sim \left( e^{ikz} + \frac{e^{ikr}}{r} S \right) \chi_{\text{inc}}. \tag{2.1}$$

By straightforward methods [55], one can conclude

$$\frac{d\sigma}{d\Omega} = \left( S\chi_{\text{inc}} \right)^{\dagger} S\chi_{\text{inc}} = \chi_{\text{inc}}^{\dagger} S^{\dagger} S \chi_{\text{inc}}, \tag{2.2}$$

or more generally,

$$\frac{d\sigma}{d\Omega} = \text{Tr}\left( S\rho_{\text{inc}} S^{\dagger} \right). \tag{2.3}$$

So, to understand any scattering problem, one needs to understand the density matrix, $\rho$, and the scattering matrix, $S$.

Following the advice of Jacob and Wick [56] by taking advantage of the helicity quantum number, $\lambda$, one can consider a pure quantum state,

$$|\psi^{(i)}; \vec{p}\rangle = \sum_{\lambda=-s}^{s} c_{\lambda}^{(i)} |\vec{p}; \lambda\rangle, \tag{2.4}$$

with $c_{\lambda}^{(i)} = \langle \vec{p}; \lambda | \psi^{(i)}; \vec{p} \rangle$, distributed in an incoherent mixture with probability $p^{(i)}$.

The spin density matrix can be defined [13]

$$\rho = \sum_i p^{(i)} |\psi^{(i)}; \vec{p}\rangle\langle\psi^{(i)}; \vec{p}| \tag{2.5}$$

$$\rho_{\lambda\lambda'} = \sum_i p^{(i)} c_\lambda^{(i)} c_{\lambda'}^{(i)*}. \tag{2.6}$$

More accurately, this is the spin density matrix in the particle's helicity rest frame. Furthermore, in an inital-state system $A + B$, the pure state, Eq. 2.4, can be generalized as

$$|\psi^{(i)}(A,B)\rangle = \sum_{\lambda_A=-s_A}^{s_A} \sum_{\lambda_B=-s_B}^{s_B} |s_A,\lambda_A;s_B,\lambda_B\rangle\langle s_A,\lambda_A;s_B,\lambda_B|\psi^{(i)}(A,B)\rangle. \tag{2.7}$$

The initial spin density matrix (Eq. 2.5) is now generalized

$$\rho_{\mathrm{i}} = \sum_i p^{(i)} |\psi^{(i)}(A,B)\rangle\langle\psi^{(i)}(A,B)\,|. \tag{2.8}$$

Now, consider the reaction $A + B \rightarrow C + D$, with helicities $a$, $b$, $c$, and $d$, respectively. If the probability amplitudes to find the final helicities, $c$ and $d$, from initial helicities, $a$ and $b$, are $M_{cd;ab}$, the final-state can be expressed in terms of the initial-state (Eq. 2.7):

$$|\psi^{(i)}(C,D)\rangle = M|\psi^{(i)}(A,B)\rangle. \tag{2.9}$$

Note, here, $\psi^{(i)}$ denotes a pure quantum state with probability $p^{(i)}$. Now, utilizing Eqs. 2.9 and 2.8, the final-state spin density matrix can take the form [13]

$$\begin{aligned}
\rho'(C,D) &= \sum_i p^{(i)} |\psi^{(i)}(C,D)\rangle\langle\psi^{(i)}(C,D)\,| \\
&= \sum_i p^{(i)} M|\psi^{(i)}(A,B)\rangle\langle\psi^{(i)}(A,B)\,|M^\dagger \\
&= M\left[\sum_i p^{(i)} |\psi^{(i)}(A,B)\rangle\langle\psi^{(i)}(A,B)\,|\right] M^\dagger \\
&= M\rho_{\mathrm{i}}(A,B)\,M^\dagger
\end{aligned} \tag{2.10}$$

$$\rho'_{cd;c'd'}\left(C,D\right) \;=\; \sum_{a,b,a',b'} M_{cd;ab}\rho_{\mathrm{i}ab;a'b'}\left(A,B\right)M^{*}_{c'd';a'b'}, \tag{2.11}$$

where $\rho_{\mathrm{i}ab;a'b'}\left(A,B\right)$ represents the components of the initial-state spin density matrix (Eq. 2.8). For $\rho_{\mathrm{i}ab;a'b'}(A,B)$ normalized such that $\mathrm{Tr}\rho_{\mathrm{i}}(A,B)=1$, then

$$\mathrm{Tr}\rho'\left(C,D\right)=\mathrm{Tr}\left[M\rho_{\mathrm{i}}M^{\dagger}\right]=\mathrm{Tr}\left[M^{\dagger}M\rho_{\mathrm{i}}\right]=\langle|M|^{2}\rangle_{\mathrm{i}}. \tag{2.12}$$

The elements $M_{cd;ab}$ are the elements of the scattering matrix when taken between final and initial helicity states. Of course, $|M|^2$ is related to the cross section, thus, they can be normalized as [13]

$$\langle|M|^{2}\rangle_{\mathrm{i}}=2\pi\frac{d^{2}\sigma}{dtd\phi}\left(\rho_{\mathrm{i}}\right). \tag{2.13}$$

So, the final-state spin density matrix can be normalized by dividing by the trace:

$$\rho\left(C,D\right)=\frac{\rho'\left(C,D\right)}{\mathrm{Tr}\rho'\left(C,D\right)}. \tag{2.14}$$

In general, one can expand the density matrix by so-called spherical tensor operators and multipole parameters [13]. For the case of spin-1/2, it is well-known [55] that one can expand the density matrix as

$$\rho=\frac{1}{2}\left(I+\vec{\mathcal{P}}\cdot\vec{\sigma}\right)=\frac{1}{2}\sum_{\alpha}\mathcal{P}^{\alpha}\sigma_{\alpha}, \tag{2.15}$$

where $\vec{\mathcal{P}}=\mathrm{Tr}\left[\rho\vec{\sigma}\right]=\langle\vec{\sigma}\rangle$ is the polarization vector and $\sigma_\alpha$ are the Pauli matrices. For the case at hand, the inital-state density matrix (Eq. 2.8) can be expressed

$$\rho_{\mathrm{i}}\left(A,B\right)=\frac{1}{2\times2}\times\sum_{\alpha\beta}\mathcal{P}^{\alpha\beta}\left(A,B\right)\sigma_{\alpha\beta}\left(A,B\right). \tag{2.16}$$

From Eqs. 2.10, 2.14, and 2.16, one can write

$$\rho\left(C,D\right)2\pi\frac{d^{2}\sigma}{dtd\phi}\left(\rho_{\mathrm{i}}\right) \;=\; M\rho_{\mathrm{i}}\left(A,B\right)M^{\dagger}$$

$$= \sum_{\alpha\beta} \frac{1}{4} \mathcal{P}^{\alpha\beta}(A,B)\, M \sigma_{\alpha\beta}(A,B)\, M^{\dagger}. \tag{2.17}$$

By multiplying by $\sigma_{\alpha'\beta'}(C,D)$ and taking the trace, Eq. 2.17 becomes [13]

$$\begin{aligned} 2\pi \frac{d^2\sigma}{dt d\phi}(\rho_{\mathrm{i}})\, \mathcal{P}^{\alpha'\beta'}(C,D) &= \sum_{\alpha\beta} \mathcal{P}^{\alpha\beta}(A,B)\, \frac{1}{4} \mathrm{Tr}\left[ M \sigma_{\alpha\beta}(A,B)\, M^{\dagger} \sigma_{\alpha'\beta'}(C,D) \right] \\ &= \left( \frac{d\sigma}{dt} \right) \sum_{\alpha,\beta} \mathcal{P}^{\alpha\beta}(A,B)\, (\alpha,\beta|\alpha',\beta')_{\phi}. \end{aligned} \tag{2.18}$$

Thus, the final-state polarization can be expressed in terms of the inital-state polarization. The key components are the "dynamical reaction parameters," defined as [13]

$$(\alpha,\beta|\alpha',\beta')_{\phi} \equiv \frac{1}{4} \left( \frac{d\sigma}{dt} \right)^{-1} \mathrm{Tr}\left[ M \sigma_{\alpha\beta}(A,B)\, M^{\dagger} \sigma_{\alpha'\beta'}(C,D) \right] \tag{2.19}$$

$$= \mathcal{R}^{z}_{\alpha\alpha''}(\phi)\, \mathcal{R}^{z}_{\beta\beta''}(-\phi)\, (\alpha''\beta''|\alpha'\beta'), \tag{2.20}$$

where

$$\mathcal{R}^{z}(\phi) = \begin{bmatrix} 1 & 0 & 0 & 0 \\ 0 & \cos\phi & -\sin\phi & 0 \\ 0 & \sin\phi & \cos\phi & 0 \\ 0 & 0 & 0 & 1 \end{bmatrix}. \tag{2.21}$$

B. The Analyzing Power

For an example, consider the reaction $A^{\uparrow(\downarrow)} + B \rightarrow C + D$ with $\vec{\mathcal{P}}^{A\uparrow} = (\mathcal{P}_x, \mathcal{P}_y, 0)$ and $\vec{\mathcal{P}}^{A\uparrow} = -\vec{\mathcal{P}}^{A\downarrow}$. Using Eqs. 2.18, 2.19, 2.20, and 2.21 one can write

$$\begin{aligned} \frac{d^2\sigma}{dt d\phi} &= \frac{1}{2\pi} \left( \frac{d\sigma}{dt} \right) \sum_{\alpha} \mathcal{P}^{\alpha}(A)\, (\alpha, 0|0,0)_{\phi} \\ &= \frac{1}{2\pi} \left( \frac{d\sigma}{dt} \right) \left\{ 1 + \mathcal{P}_x (X, 0|0,0)_{\phi} + \mathcal{P}_y (Y, 0|0,0)_{\phi} \right\} \\ &= \frac{1}{2\pi} \left( \frac{d\sigma}{dt} \right) \left\{ 1 + (\mathcal{P}_x \cos\phi + \mathcal{P}_y \sin\phi)\, (X, 0|0,0) \right. \end{aligned}$$

$$
\begin{aligned}
& + \left(\mathcal{P}_y \cos\phi - \mathcal{P}_x \sin\phi\right)(Y, 0|0, 0)\} \\
= \; & \frac{1}{2\pi}\left(\frac{d\sigma}{dt}\right)\{1 + \mathcal{P}\,(X, 0|0, 0)\cos\left(\phi_S - \phi\right) \\
& + \mathcal{P}\,(Y, 0|0, 0)\sin\left(\phi_S - \phi\right)\}\,, \qquad (2.22)
\end{aligned}
$$

where $\phi_S$ denotes the azimuthal angle of $\mathcal{P}$. At this point, consider $(X, 0|0, 0)$. From Eq. 2.19,

$$
(X, 0|0, 0) \;=\; \frac{1}{4}\left(\frac{d\sigma}{dt}\right)^{-1} \mathrm{Tr}\left[M\sigma_x M^\dagger\right], \qquad (2.23)
$$

for which one finds $(X, 0|0, 0) = 0$ [13]. Now, Eq. 2.22 simplifies to

$$
\frac{d^2\sigma}{dtd\phi} = \frac{1}{2\pi}\left(\frac{d\sigma}{dt}\right)\{1 + \mathcal{P}\,(Y, 0|0, 0)\sin\left(\phi_S - \phi\right)\}\,. \qquad (2.24)
$$

Now, since $d^2\sigma^\uparrow/dtd\phi + d^2\sigma^\downarrow/dtd\phi = (d\sigma/dt)\,2/2\pi$, Eq. 2.24 can be used to write

$$
\frac{1}{\mathcal{P}}\left(\frac{d^2\sigma^\uparrow}{dtd\phi} - \frac{d^2\sigma^\downarrow}{dtd\phi}\right) \Big/ \left(\frac{d^2\sigma^\uparrow}{dtd\phi} + \frac{d^2\sigma^\downarrow}{dtd\phi}\right) = (Y, 0|0, 0)\sin\left(\phi_S - \phi\right). \qquad (2.25)
$$

It is clear, now, $(Y, 0|0, 0)$ is the "analyzing power," $A_N$. Specifically, one can write [13]

$$
\begin{aligned}
(Y, 0|0, 0) \;&=\; \frac{1}{4}\left(\frac{d\sigma}{dt}\right)^{-1} \mathrm{Tr}\left[M\sigma_y M^\dagger\right] \\
&=\; \left(\frac{d\sigma}{dt}\right)^{-1} \Im\left[M^*_{++;-+}\left(M_{++;++} + M_{+-;+-}\right)\right. \\
&\quad \left. - M^*_{++;+-}\left(M_{++;--} - M_{+-;-+}\right)\right]. \qquad (2.26)
\end{aligned}
$$

One immediately sees that the analyzing power directly depends on so-called "helicity-flip" amplitudes, $M_{++;-+}$ and $M_{++;+-}$. As discussed in chapter 1, this is tantalizing insight which has drawn many into the tumultuous waters of spin physics.

## C. The Spin Transfer Parameters

As discussed in chapter 1, one of the keys to the Collins and IFF effects is the transfer of spin from an incoming quark to an outgoing quark. Consider the partonic reaction $a^{\uparrow} + b \rightarrow c^{\uparrow} + d$ with initial polarization $\vec{\mathcal{P}}_a$ and final polarization $\vec{\mathcal{P}}_c$. The components of $\vec{\mathcal{P}}_c$ can be expressed in terms of cartesian dynamical reaction parameters (Eq. 2.18) [13]

$$\mathcal{P}_c^x = (X,0|X,0)\sin\phi^* \tag{2.27}$$

$$\mathcal{P}_c^y = (Y,0|Y,0)\cos\phi^*, \tag{2.28}$$

where $^*$ denotes the partonic center of mass. In terms of the helicity amplitudes, $M$, (Eq. 2.19) [13]

$$\begin{aligned}(Y,0|Y,0)\frac{d\hat{\sigma}}{d\hat{t}} &= \frac{1}{4}\mathrm{Tr}\left[M\sigma_y(A)\,M^{\dagger}\sigma_y(C)\right] \\ &= \Re\left(M_{++;++}M^*_{+-;+-} - M_{++;--}M^*_{+-;-+}\right) \\ &\quad +|M_{++;+-}|^2 + |M_{++;-+}|^2,\end{aligned} \tag{2.29}$$

and

$$\begin{aligned}(X,0|X,0)\frac{d\hat{\sigma}}{d\hat{t}} &= \frac{1}{4}\mathrm{Tr}\left[M\sigma_x(A)\,M^{\dagger}\sigma_x(C)\right] \\ &= \Re\left(M_{++;++}M^*_{+-;+-} + M_{++;--}M^*_{+-;-+}\right) \\ &\quad +|M_{++;+-}|^2 - |M_{++;-+}|^2.\end{aligned} \tag{2.30}$$

Now, since to first order, partonic helicity-flip amplitudes are zero, Eqs. 2.29 and 2.30 become

$$(Y,0|Y,0)\frac{d\hat{\sigma}}{d\hat{t}} = \Re\left(M_{++;++}M^*_{+-;+-}\right) \tag{2.31}$$

$$(X,0|X,0)\frac{d\hat{\sigma}}{d\hat{t}} = \Re\left(M_{++;++}M^*_{+-;+-}\right), \tag{2.32}$$

and one can define $(X,0|X,0) = (Y,0|Y,0) = \hat{d}_{TT}(\theta^*)$. These are the partonic spin-transfer parameters. For this analysis the relevant subprocesses are $q+q' \to q+q'$, $q+q \to q+q$, and $q+g \to q+g$. For these subprocesses, [30, 13]

$$q+q \to q+q \qquad \hat{d}_{TT}\frac{d\hat{\sigma}}{d\hat{t}} = g_s^4\frac{2}{9}\left[\frac{4\hat{s}\hat{u}}{-\hat{t}^2} - \frac{1}{3}\frac{4\hat{s}}{-\hat{t}}\right] \tag{2.33}$$

$$q+q' \to q+q' \qquad \hat{d}_{TT}\frac{d\hat{\sigma}}{d\hat{t}} = g_s^4\frac{2}{9}\frac{4\hat{s}\hat{u}}{-\hat{t}^2} \tag{2.34}$$

$$q+g \to q+g \qquad \hat{d}_{TT}\frac{d\hat{\sigma}}{d\hat{t}} = g_s^4\left[\frac{8}{9} + \frac{1}{2}\frac{-4\hat{u}\hat{s}}{\hat{t}^2}\right]. \tag{2.35}$$

As shown in Fig. 3, in the limit $\cos\theta^* \to 1$, one finds $\hat{d}_{TT} \to 1$, suggesting larger Collins and IFF effects at forward kinematics.

# CHAPTER III

# EXPERIMENTAL SETUP

Spin effects would be pointless to discuss had one no means to produce the polarized beams necessary to observe them. As discussed in chapter 1, large spin effects have been observed at a variety of facilities [2, 4, 5, 6, 10, 9]. One of the facilities at which large spin effects have been observed in correlation with cross sections in agreement with predicted collinear pQCD cross sections [9, 12] is the Relativistic Heavy Ion Collider (RHIC) at Brookhaven National Laboratory (BNL) (Fig. 11).

## A. A History of the Relativistic Heavy Ion Collider

The concept of RHIC dates back to 1983, when the DOE/NSF Nuclear Science Advisory Committee identified "a relativisitic heavy ion collider as the highest priority for the next major facility to be constructed" [57]. The original goal was the investigation of nuclear matter at extreme temperature and density, specifically, to create and study quark-gluon plasma.

The notion to utilize RHIC as a "spin collider" was discussed at a November 1990 Polarized Collider Worshop at Pennsylvania State University [58]. Born out of this meeting was the RHIC Spin Collaboration which submitted a letter of intent to the BNL Program Advisory Committee in August 1991. The formal proposal [59] was submitted in October 1992 gaining approval the following year. In September 1995, RIKEN agreed to provide additional funding for accelerator components and spin-physics upgrades for the PHENIX detector.

Construction for the RHIC project began in 1991 and lasted eight years. On June 12, 2000, the first $Au + Au$ collisions, at $\sqrt{s} = 56$ GeV took place, followed by additional collisions at $\sqrt{s} = 130$ GeV. Finally, on July 18, 2001, heavy-ion collisions

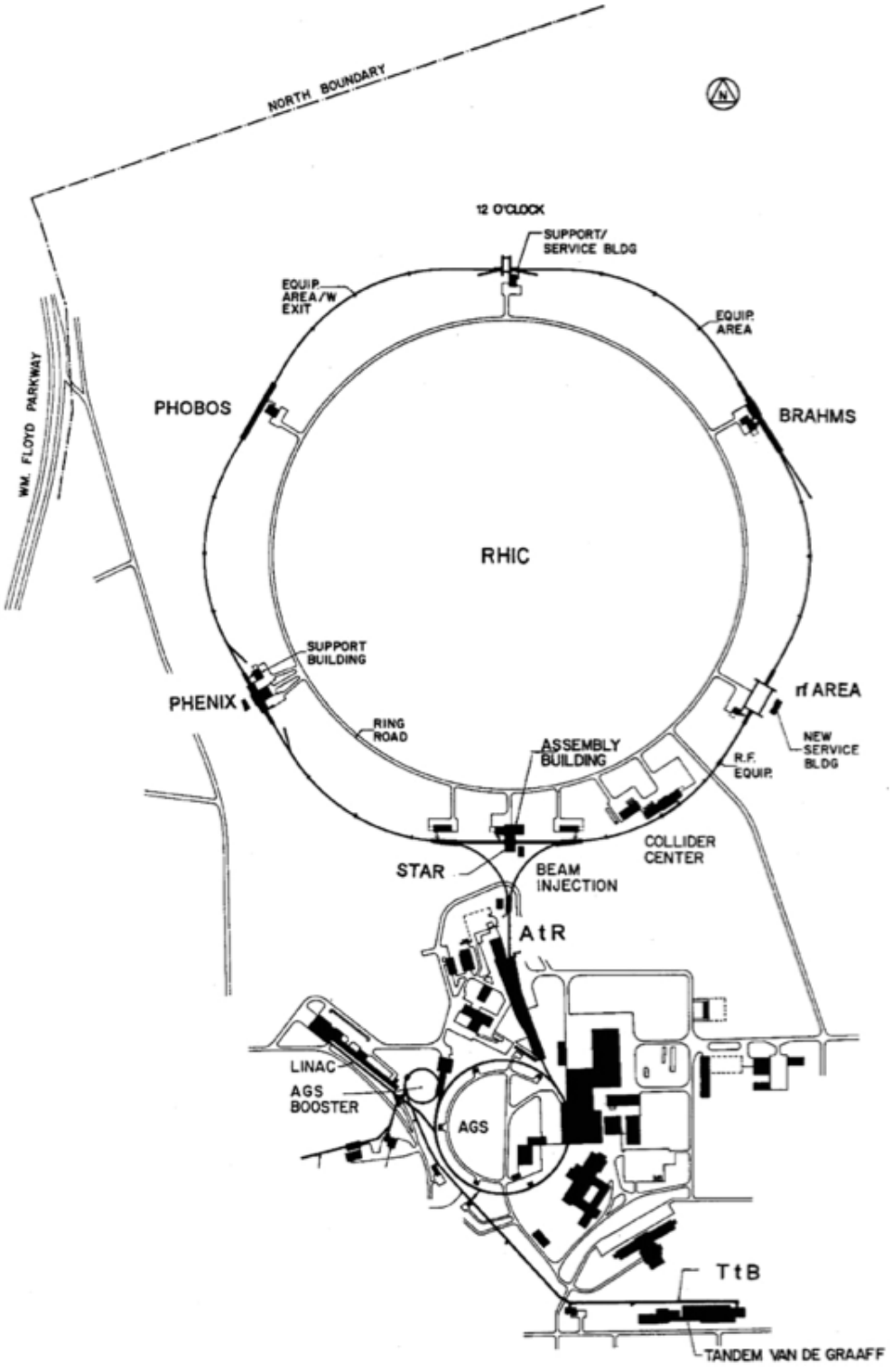


Fig. 11.: The RHIC facility.

reached the design energy of $\sqrt{s} = 200$ GeV.

RHIC as a spin collider became a reality on December 20, 2001, with the first $\vec{p} + \vec{p}$ collisions at $\sqrt{s} = 200$ GeV. A further milestone was achieved on February 12, 2009, with the first collisions at $\sqrt{s} = 500$ GeV.

## B. The Polarized Beam

Achieving polarized-proton collisions at energies as high as $\sqrt{s} = 200$ and 500 GeV is a complicated, multi-step process. The initial polarized protons are generated from an Electron Cyclotron Resonance (ECR) type Optically-Pumped Polarized Ion Source (OPPIS) constructed at TRIUMF from the KEK OPPIS [60]. $H^+$ ions are produced with a 28 GHz ECR source and passed into a Rb neutralization cell. Electron-spin polarized Rb atoms are created by absorption of circularly-polarized light from dye lasers tuned to the wavelength of the D1 line. Interaction between the $H^+$ ions and the optically-pumped Rb vapor neutralizes some of the $H^+$ ions with a polarized electron. As the resulting fast $H^0$ passes to the Na ionizing cell, a short period of low magnetic field polarizes the $H^0$ nucleus via the hyperfine interaction. A Na-jet ionizing cell produces the final $H^-$ ions ready for the acceleration process.

The pulse of polarized $H^-$ is initially accelerated to 200 MeV by a radio-frequency quadrupole and the 200 MHz LINAC. This pulse is strip-injected into the AGS Booster, where it undergoes acceleration to 1.5 GeV before being transferred to the AGS for acceleration to 25 GeV. After transport to RHIC via the AGS to RHIC (AtR) transfer line the beams can be accelerated to the collision energies of 100 GeV or 250 GeV in each beam [61].

During acceleration, the spin polarization, $\vec{P}$ is directed by the Thomas-BMT

equation [62]

$$\frac{d\vec{P}}{dt} = -\left(\frac{e}{\gamma m}\right)\left[G\gamma\vec{B}_{\perp} + (1+G)\,\vec{B}_{\parallel}\right] \times \vec{P}, \tag{3.1}$$

where, for the purpose, here, $m$ is the mass of the proton, $G = 1.7928$ is the anomalous magnetic moment of the proton, and $E = \gamma m$. Comparing this equation to the Lorentz force law

$$\frac{d\vec{v}}{dt} = -\left(\frac{e}{\gamma m}\right)\left[\vec{B}_{\perp}\right] \times \vec{v}, \tag{3.2}$$

one sees that in a vertical field the polarization vector rotates $G\gamma$ times for every orbit. One can refer to $\nu_{sp} = G\gamma$ as the "spin tune."

The main problem surrounding acceleration of polarized beams is overcoming depolarization resonances, in particular, imperfection resonances and intrinsic resonances. Imperfection resonances are achieved when $\nu_{sp} = n$, where $n$ is an integer; and intrinsic resonances are achieved when $\nu_{sp} = kP \pm \nu_y$, where $k$ is an integer, $P$ is the number of identical accelerator sections (superperiodicity), and $\nu_y$ is the betatron tune. To overcome these resonances, RHIC utilizes "Siberian Snakes" [63], which rotate the polarization 180° through a horizontal axis. As the snake introduces a half-integer spin tune, the requirements for depolarization resonances cannot be met, as long as the betatron tune is not half-integer [61].

In the AGS Booster, three imperfection resonances are overcome by harmonic corrections to the vertical closed orbit. Acceleration in the AGS crosses forty-one imperfection resonances and seven strong intrinsic resonances. These are crossed with a 5.9% partial snake and a 15% partial snake. For 2008, eighty-two horizontal resonances were uncorrected, resulting in a $\sim 10\%$ loss of polarization. Finally, two pairs of full snakes, are positioned at opposite positions on the RHIC ring to avoid the myriad of depolarization resonances encountered during acceleration to collision energies [64].

The polarization of the RHIC beam is determined by Coulomb-Nuclear Interference (CNI) polarimetry. CNI polarimetry measures the elastic scattering asymmetry due to the interference of spin-flip and non-flip terms of the electromagnetic and hadronic amplitudes, i.e.

$$A_N \sim \frac{\phi^{\mathrm{em}\,*}_{\mathrm{flip}}\phi^{\mathrm{had}}_{\mathrm{non-flip}} + \phi^{\mathrm{em}}_{\mathrm{non-flip}}{}^{*}\phi^{\mathrm{had}}_{\mathrm{flip}}}{\left|\phi^{\mathrm{em}}\right|^2 + \left|\phi^{\mathrm{had}}\right|^2} \tag{3.3}$$

Relative polarization is quickly determined with a $p + C$ polarimeter, which is later normalized to a $H$-jet polarimeter for absolute polarization. In addition, both STAR and PHENIX utilize local polarimetry, with PHENIX utilizing the spin-dependence of forward neutrons and STAR detecting forward hadrons in the STAR Beam-Beam Counter (BBC) [65].

In a typical run, such as the 2008 $p^{\uparrow}+p^{\uparrow}$ run, each ring is divided into 120 bunches of protons, numbering from 0 to 119. The rings are then tuned in such a way that a particular bunch from the clockwise beam, denoted as the "blue" beam, crosses the experimental halls with a particular bunch from the counter-clockwise beam, denoted as the "yellow" beam. This procedure is termed "cogging" the beam. As an example, in 2008, the beam was cogged in such a way that bunch 0 for each beam crossed the 2 o'clock and 8 o'clock positions on the RHIC ring. This resulted in bunch 0 from the blue beam intersecting with bunch 80 from the yellow beam at the STAR interaction point at the 6 o'clock position on the ring. The intersections of the bunches are termed "bunch-crossings" and are also assigned an index from 0 to 119. Each time the RHIC ring is filled, the bunches are filled with a particular pattern to the spin orientation. These patterns ensure that the interactions experience each possible combination of polarization directions. Thus, by knowing the particular bunch crossing and the spin pattern for the given fill, one can deduce the polarization orientation in each beam for a particular event.

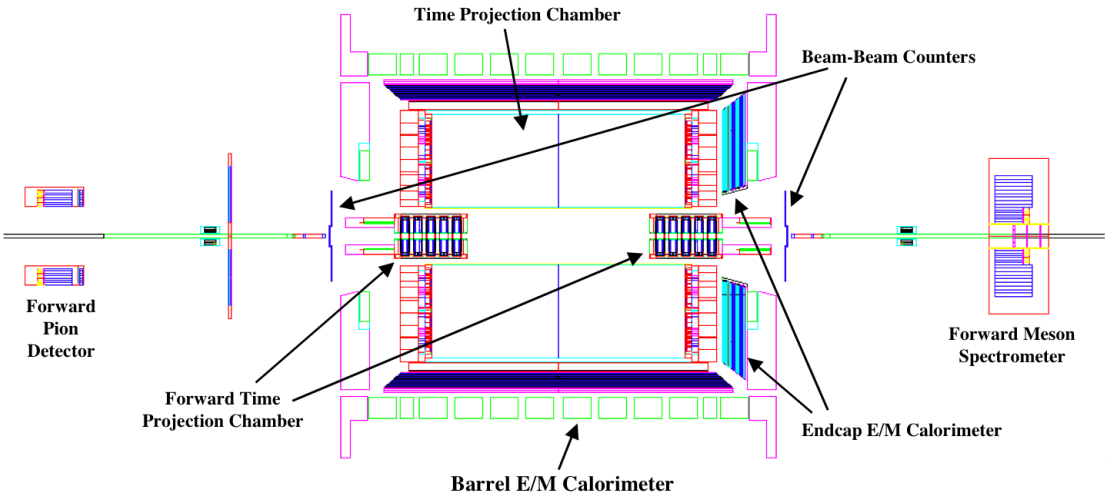


Fig. 12.: The Solenoidal Tracker at RHIC in 2008.

## C. The Solenoidal Tracker at RHIC

One of the large detectors equipped to utilize the polarized beam is the Solenoidal Tracker at RHIC (STAR) (Fig. 12). Designed to handle the large particle multiplicity from central heavy ion collisions over a large acceptance [66], STAR is outfitted with a large Time Projection Chamber (TPC) [67], spanning $|\eta| < 1.8$ over the full azimuth. Surrounding the TPC, the Barrel Electromagnetic Calorimeter (BEMC) [68] provides large acceptance for neutral and electromagnetic energy, extending STAR's capability to measure neutral-decay mesons, such as $\pi^0$'s and $\eta$ mesons, as well as extending STAR efficiency for jet reconstruction. Tracking at forward angles is achieved by means of the Forward Time Projection Chamber (FTPC) [69], spanning $2.5 < |\eta| < 4$ over the full azimuth. Forward calorimetry is extended with the Endcap Electromagnetic Calorimeter (EEMC) [70] over the range of $1 < \eta < 2.0$ and the Forward Meson Spectrometer (FMS) [71] over the range of $2.5 < \eta < 4$ each over the full azimuth. The aforementioned BBC's [65] consist of hexagonal tiles of scintillator annuli situ-

ated 3.7 m from the interaction point, covering $2.1 < |\eta| < 5.0$. Each BBC module is composed of two groups of hexagonal tiles: two rings of small tiles surrounded by two rings of large tiles. The BBC modules equip STAR with local polarimetry, luminosity information, as well as coincidence information for tagging non-singly diffractive events.

Because STAR includes subsystems with widely varying read-out times, the trigger system [72] utilizes a multi-layered system. So-called "fast detectors," such as the BEMC, EEMC, BBC, and FMS, are digitized every crossing ($\sim$ 10 MHz). The first three trigger layers, L0, L1, and L2, utilize data from these fast detectors to determine whether or not to read out the "slow detectors." At L0, fast detector information is sent to a tree of Data Storage and Manipulation (DSM) modules which propagate this information to a Trigger Control Unit (TCU). If the information matches trigger requirements and the requested detectors are live, L0 is satisfied. The slow detectors, then, begin the digitization process. During the slow detector digitization, raw fast detector data is analyzed with different levels of granularity for L1 and L2. If the data satisfy this level, the event is sent to the STAR DAQ [73]. The L0, L1, and L2 decisions can be made in 1.5 $\mu$s, 100 $\mu$s, and 5 ms, respectively. A fourth level, L3, is a software trigger utilizing slow detector data. Decisions at L3 can be made in 200 ms.

### D. The Forward Time Projection Chamber

The FTPC [69] (Fig. 13) was constructed with the goal of 1-2 mm track separation capability in the limited space available inside the STAR TPC. To make use of this space, a radial drift configuration with curved readout chambers was used. The anode wires were, first, glued to a flat pad plate with conductive epoxy. Between

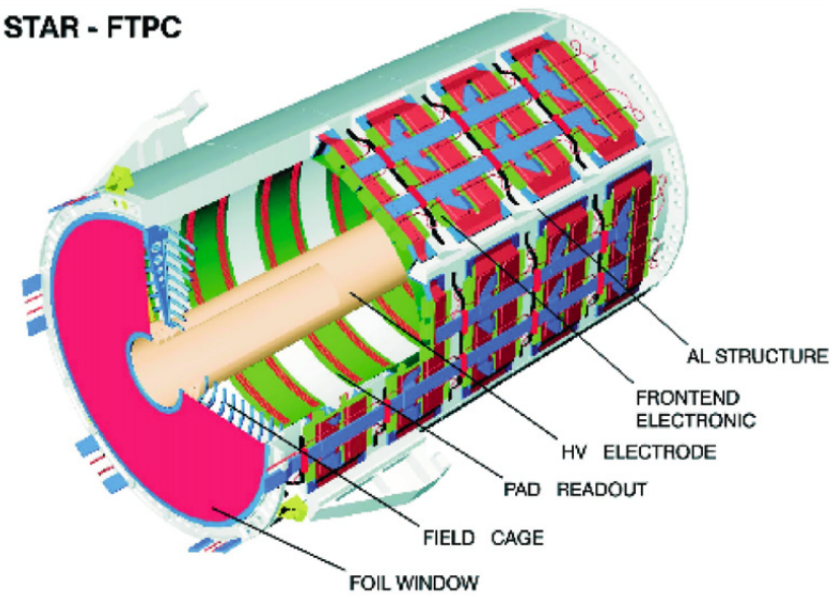


Fig. 13.: The STAR Forward Time Projection Chamber [69].

three rollers, the plate was then bent to the desired radius of 305 mm. Because of the short drift length (23 cm.), an $Ar/CO_2$ gas mixture is used.

The physical arrangement of the FTPC is organized into five rings of two padrows each. Further, the rings are subdivided into six azimuthal readout chambers (sectors). The field cage is composed of an inner high-voltage electrode and the outer cylinder wall at ground voltage. The sensitive volumes span 93.7 cm in length ($162.75 < |z_{\mathrm{STAR}}| < 256.75$ cm) with an inner radius of 7.73 cm and an outer radius of 30.03 cm.

A total of 19,200 channels of electronics are used in the FTPC. The drift time, 50 $\mu$s for 23 cm, is divided into 256 time bins. A shaping time of 350 ns is used. All told, this results in a 5 MHz sampling rate.

The FTPC is equipped with a laser system to provide straight tracks of known position. These can be used to correct for spatial distortions, calibrate drift velocities,

and test the detector in the absence of collider activity.

Data reconstruction is accomplished in a two-step process. First, a cluster-finding algortithm [74] is used to determine hit coordinates. The cluster finder reads in the electronics signal, finds areas of non-zero charge, deconvolutes clusters, and fits the coordinates. Second, a track-reconstruction algorithm [75] determines charged-particle tracks and their momenta. The track-reconstruction algorithm utilizes a conformal mapping procedure. Tracks are determined by a straight-line fit to the cluster hits in helical coordinates. Extrapolating the tracks to an intersection determines a primary collision vertex. The momenta of the tracks are then determined by utilizing the magnetic field and the primary vertex.

### E. The Forward Meson Spectrometer

The FMS (Fig. 14) was constructed with the goal of studying nuclear gluon densities, parton saturation, and proton spin [71]. Extending calorimetry to forward angles allows STAR to access low-x gluon processes and forward pion production critical to these goals.

The physical arrangement of the FMS is two lead-glass (PbGl) arrays surrounding the beam pipe at a distance of 706 cm from the interaction point. The two arrays are arranged as follows: an inner calorimeter of 476 "small cells" ($3.8 \times 3.8 \times 45$ cm$^3$) and an outer calorimeter of 788 "large cells" ($5.8 \times 5.8 \times 60$ cm$^3$). The full stack spans an area of $34 \times 34$ large cells. Metal spacers (depicted as green cells in Fig. 14) sit in the place of 28 large cells in each corner. The inner calorimeter spans an area of $24 \times 24$ small cells, utilizing plastic spacers to fit smoothly within a $16 \times 16$ large cell space around the beam. Within the inner calorimeter sits an aluminum spacer of an area equal to $10 \times 10$ small cells surrounding the beam pipe. The FMS stack

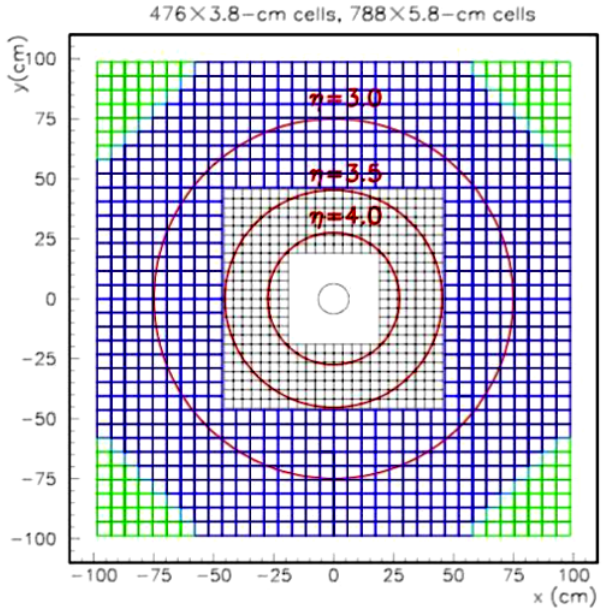


Fig. 14.: The STAR Forward Meson Spectrometer.

is physically separated into two halves, left and right of the beam, and situated on a movable track, allowing the two halves to close toward and separate from around the beam pipe.

Large cells are fitted with 10-stage Amperex XP2202 phototubes with 1200 V/mA resistive dividers and zener diodes on the last four stages to control rate dependence. Small cells, on the other hand are fitted with two different types of phototubes. 224 small cells are outfitted with 12-stage FEU-84 phototubes with Cockroft-Walton bases utilizing a diode-chain and chopper boards. The remaining small cells are fitted with 10-stage Amperex XP2972 phototubes with Cockroft-Walton bases.

The FMS is equipped with an LED monitoring system to test detector response and monitor gains during a run when the enclosure is inaccessible. The system is composed of a box with optical fibers attached to a lucite mixer bar and LED's. The fibers are routed to holes in the face of the box positioned to distribute the LED light

to each FMS cell.

Construction of the detector was completed in February of 2007. Because of limited numbers of detectors, it was necessary to repair some detectors with varying levels of damage, e.g. radiation damage and bad optical connections. Large cell phototubes were fixed with an optical cookie to an aluminum can and phenolic block assembly. This assembly was then glued to the PbGl with a two-part optical epoxy. Small cell phototubes were glued directly to the PbGl face. Each cell was cleaned with ethanol and wrapped in aluminized mylar to improve light containment and limit cross-talk between detectors. After wrapping, each detector was measured for length and width. Large cell phototube I/V curves were evaluated for faulty zener diodes, and each cell was also LED tested to determine an optimal position relative to the beam. Low gain cells were positioned closer to the beam, and high gain cells were positioned farther from the beam to try to balance the response across the coverage area.

Readout of the FMS is governed by so-called QT electronics. An eight-channel QT-8 daughter card records ADC information from eight different cells. Four such cards each send to a thirty-two channel QT-32 motherboard a three-bit ID and twelve-bit ADC value for the highest ADC cell of the eight covered. Each QT-32, then, finds the highest of the four values and passes this information along with a five bit ID to DSM boards in the STAR trigger system [72].

For 2008, the FMS utilized a so-called "high-tower" trigger, firing when an individual cell reported ADC's above a certain threshold. In 2008, the thresholds were 200 for large cells and 400 for small cells. The trigger was applied over three "layers" in the DSM tree. The first layer compared ADC values to the two thresholds and OR'ed the results with a "mask" bit which determined if the ADC value was to contribute to the trigger. These results were OR'ed together as they were propagated

through the other layers.

Photon reconstruction in the FMS is accomplished by means of a cluster-finding algorithm [76]. The towers from each event are divided into clusters, and a moment analysis is performed to determine the number of photons within a cluster. A shower shape function is used to fit the tower response from which photon location and energy can be extracted.

PMT gains are calibrated using $\pi^0$'s constructed from the reconstructed photons. First, the $\pi^0$'s are associated with the highest energy tower in the event. Then, for each tower, the gains are scaled by the ratio of the reconstructed mass to the known value of 135 MeV. The procedure is iterated until the gains converge. A further correction is applied to the photons, themselves, to account for an energy-dependent shift in the mass of the pion after calibration.

# CHAPTER IV

# EVENT LEVEL CUTS

Not all events are of interest to this analysis. For that matter, not all of the events in the data are physical. What one needs is a series of cuts to weed out useless events, and, ultimately, trim away events that cause more trouble than they are worth (e.g. too much background and not enough signal).

## A. Trigger

For a correlation analysis involving multiple subsystems, one needs to access events from triggers which simultaneously read out data from the desired subsystems. In this case, I desire to correlate events from the FMS and FTPC. In 2008, STAR defined a trigger known as FMS-slow. This trigger read out the slow detectors, such as the TPC and FTPC, for a prescaled subset of the events that satisfied the FMS trigger condition. FMS-slow triggers for the 2008 $p+p$ run can be accessed in the data files by way of a trigger ID. In the early portion of the run (runs 9043035 to 9050071) the FMS-slow ID was labeled 220980, while in the latter portion of the run (runs 9050072 to 9070007) the trigger ID was labeled 220981. The 2008 FMS-slow data are stored in a separate data stream, known as st_fmsslow, from the general STAR physics triggers, typically labeled st_phys. One might assume that all of the data in the st_fmsslow stream satisfy the FMS-slow trigger ID, however, investigation shows that $\approx 5\%$ of events within the stream do not satisfy either of the documented trigger ID's from the 2008 polarized-proton run. Thus, it is necessary to implement a trigger ID cut to ensure selection of the relevant data for this analysis.

As discussed in chapter 3, the 2008 FMS trigger condition was a "high-tower" trigger, where an ADC requirement was imposed on the individual towers of the FMS,

above which the data are read out. For $< 0.5\%$ of events, communication or timing errors occurred, manifesting themselves as events without a tower above the trigger threshold. It is trivial to veto those events which do not appear to satisfy the trigger requirement.

Unfortunately, the high-tower trigger in 2008 suffers from severe non-uniformity in the gains (Fig. 15). This was exacerbated by what turned out to be insufficient magnetic shielding around the phototubes. The close proximity to the RHIC DX magnet coupled with the STAR magnet fringe field tended to reduce the phototube gains, thus raising the effective energy threshold needed to satisfy the high-tower requirement. As a result, the 2008 triggers are dominated by two low-threshold towers, which account for nearly one-third of all triggers. Including these two towers, the top ten most frequent trigger towers account for over half of the triggers from the data set. Six of these towers are located in the outer calorimeter at lower $\eta$, where one would expect lower multiplicity. Furthermore, around 12% of the towers account for none of the triggers. Altogether, this is a substantial problem in terms of trigger acceptance; and, so, it is necessary to mask out the top two towers. Without such an action, acceptance effects are quite dramatic and difficult to correct, both for the unpolarized correlation signal as well as the acceptance complications to the spin asymmetries. To do this, I assign in the software an ADC of zero to the top two most frequent trigger towers. This is a sizeable loss of data, but necessary for any hope of a meaningful measurement.

As I will show in a forthcoming section, the gain non-uniformity can lead to an energetic charged hadron leaving sufficient energy in the calorimeter to satisfy the high-tower condition. Since I am only interested in events triggered by a $\pi^0$, these events are not of interest. In addition to the energy deposited in the FMS, these events will also leave a track in the FTPC. These "auto-correlations" input

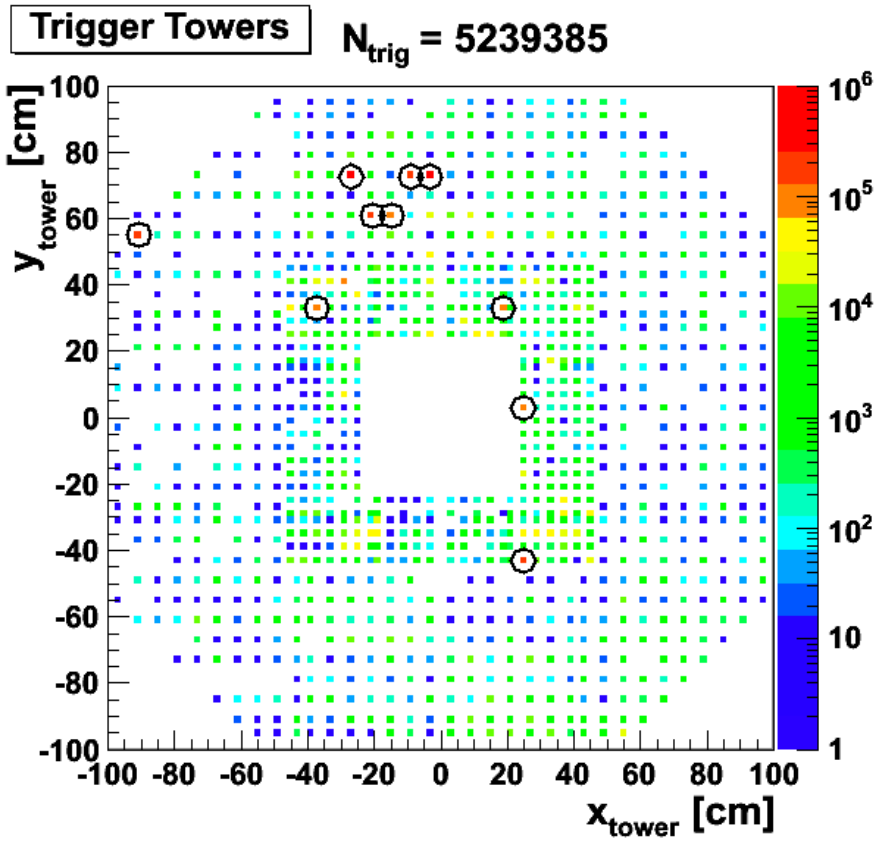


Fig. 15.: The location of each trigger tower is shown. It is clear that the trigger is represented in a non-uniform manner with a handful of towers accounting for the bulk of the triggers and others never represented in the trigger. The top ten most frequent towers, accounting for over half of the triggers, are circled in black. Note that six of the ten are from the outer calorimeter (i.e. lower $\eta$), where one does not expect significantly high multiplicity.

significant dilution into the desired signal of a correlation of two different particles from the event. Thus, it is necessary to cut auto-correlations from the trigger. Here, I require that the event have at least one FMS tower above the high-tower threshold which does not have an auto-correlated track in the FTPC. I leave open the possibility for additional towers satisfying the trigger with auto-correlated tracks, as long as one uncorrelated trigger tower is present in the event. The procedure for this veto will be discussed in a forthcoming section.

## B. LED Veto

As I discussed in the previous chapter, the FMS is equipped with an LED monitoring system, which distributes LED light to each tower. LED-triggered events are non-physical and distort the reconstruction of trigger pions which I correlate to tracks. Additionally, LED's can induce "after-pulsing," which is commonly described as a "false" signal appearing after a "true" signal. One of the ways these after-pulses can occur is by an electron slipping out of the dynode and ionizing gas within the PMT vacuum. If these ions perturb the photocathode, this can lead to electron multiplication within the dynode chain creating a pulse well after the LED signal. This LED after-pulsing needs to be rejected along with the LED events.

While LED events can be excluded simply by referring to the LED trigger bit, a more involved method is needed to veto LED after-pulsing events in the FMS-slow data. First, a full pass over the FMS-slow data is used to log run number, event number, and bunch-crossing number when the LED bit in the trigger is "on." From this pass, a list for each run is compiled of bunch-crossings corresponding to an LED event. After-pulsing events are excluded by referring to the LED lists. Events are excluded when the current bunch-crossing is within three bunch-crossings before or

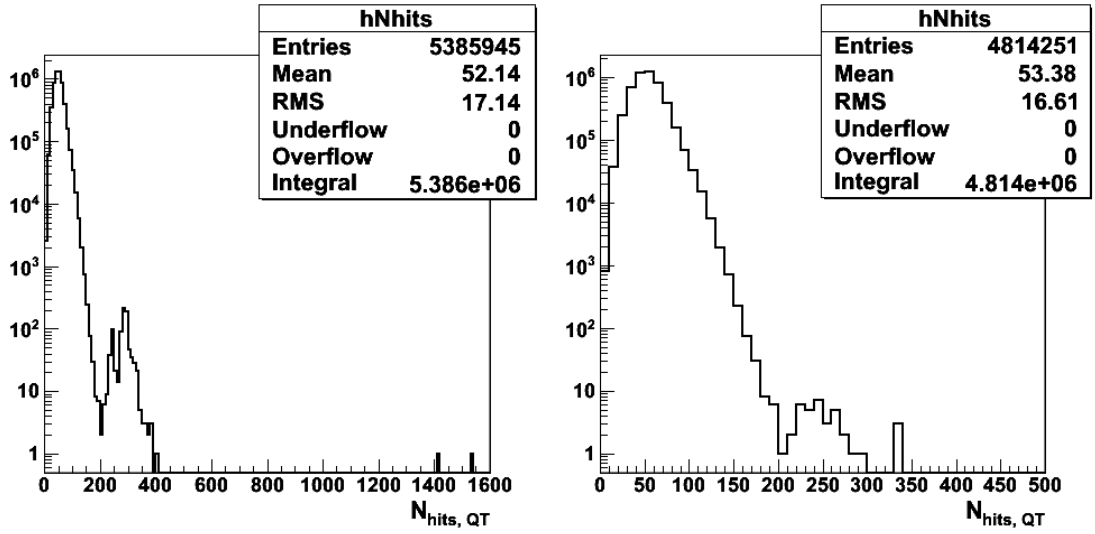


(a) (b)

Fig. 16.: QT hit distributions (a) after rejecting LED and LED after-pulse bunch crossings, and (b) after exclusion of problematic runs. Each step reduces the number of LED-like events, yet LED-like events still remain. Remaining events are excluded by way of a cut on summed FMS tower energy.

ten bunch-crossings after an LED event.

Evaluating the distribution of FMS QT hits from events passing the bunch-crossing cuts (Fig. 16a) reveals that a small number of LED and after-pulsing events remain after the bunch-crossing cut. Most of these events, apparently, correspond to hardware issues during the run. Among the runs with $N_{\rm hits} > 200$, three runs (run 9045006 containing 165 such events, run 9045014 containing 23, and run 9068063 containing 581) appear to have timing issues. Logs from each run show that past a certain point in the run, no LED or after-pulsing events are tagged, but high $N_{\rm hits}$ events persist. One possible explanation is that after a certain point in the run the trigger clock began to go out of sync with the RHIC clock. In addition to these high-$N_{\rm hits}$ runs, three runs (9065027, 9068081, and 9049048) contain many events with

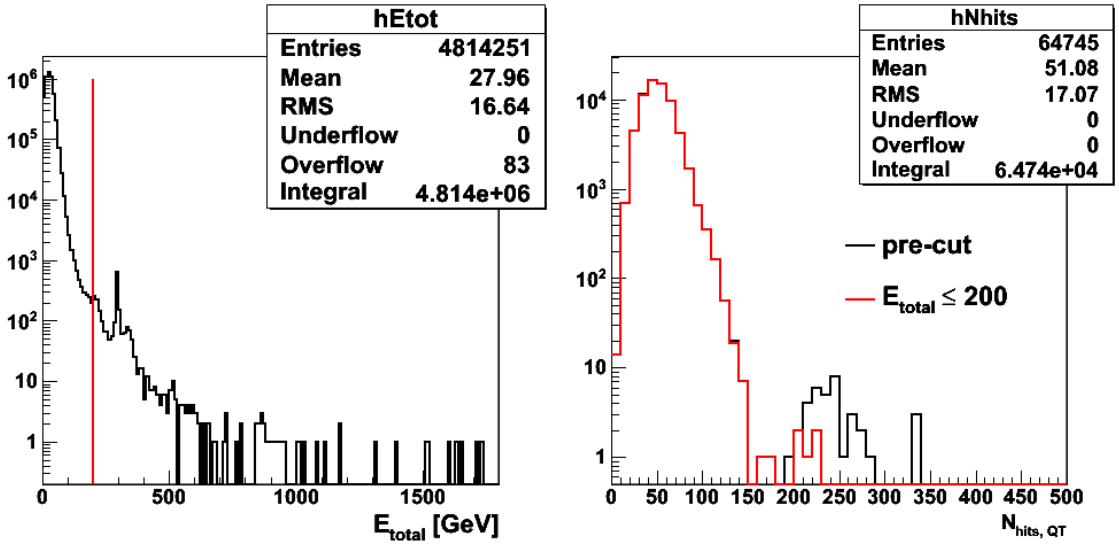


(a) (b)

Fig. 17.: (a) The energy spectrum for the sum of all FMS tower energy deposition shows a small ($\approx 0.08\%$) number of events above the collision energy of 200 GeV (denoted with a red line). Exclusion of these events accounts for the final cut in the LED veto. After the summed energy cut (b), the QT hit spectrum shows considerable reduction in the number of high $N_{\text{hits}}$ events. (b) shows a subset of runs used in (a) to focus on those with high $N_{\text{hits}}$.

unusually high numbers of reconstructed trigger photons in the FMS. The logs for these runs have similar structure to the high-$N_{\text{hits}}$ runs, where, after a certain point in the run, no LED events register, but high-$N_{\text{trig}}$ events persist. The most efficient way to deal with these issues is to exclude events from these troublesome periods.

The LED leak-through is quite small after excluding the troubled runs (Fig. 16b). Remaining leak-through is accounted for by imposing an upper-limit of 200 GeV on the summed energy of all FMS towers (Fig. 17). As a sanity-check, the invariant mass spectrum of di-photons satisfying the trigger is much cleaner after the LED veto. Particularly, the spectrum for events when both photons satisfy the trigger

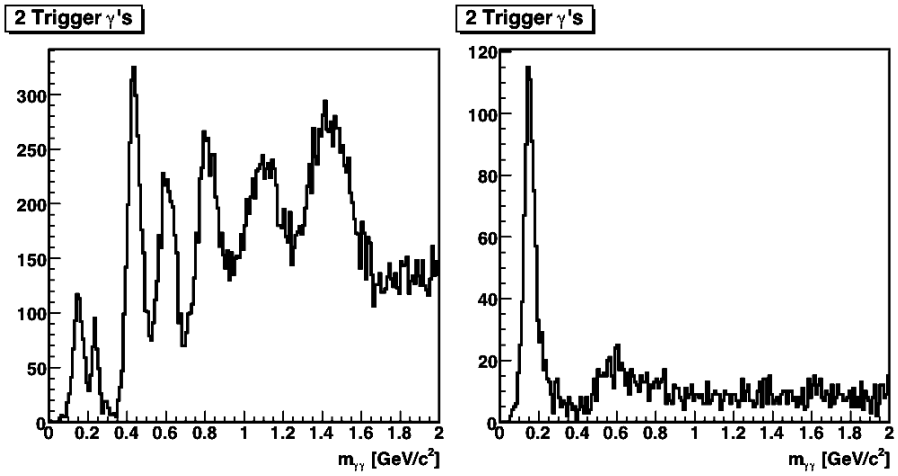


(a) (b)

Fig. 18.: The invariant mass distribution for two-trigger photon events (a) before LED exclusion and (b) after LED exclusion. The LED veto leaves most of the events in the $\pi^0$ peak, while eliminating most of the high-mass structure from the LED's. The cuts also appear to reveal the presence of an $\eta$ peak.

(Fig. 18) shows marked improvement. The cuts seem to preserve entirely the $\pi^0$ peak while excluding the LED-induced structures at higher mass. Furthermore, evidence of an $\eta$ peak is revealed after the LED cuts.

### C. FTPC Detector State

Essential to this correlation analysis is the reliability of the FTPC data. One of the standard methods within STAR is the detector state flag. The status for each detector is stored event-by-event within the data file and can be referenced offline to determine the reliability of the data for a particular subsystem. For this analysis, the event is rejected if the west FTPC does not return a "good" detector state or if the state is returned as "bad." These events correspond to voltage trips in the west FTPC and account for $< 5\%$ of the data.

### D. Vertex

Tracks from the FTPC are only stored with information from the vertex corresponding to the event's collision ("primary vertex"). Furthermore, the efficiency of the FTPC strongly depends on the quality of the reconstructed vertex as well as its location in STAR. Requiring a primary vertex is a negligible cut, excluding $< 0.1\%$ of events. To evaluate the quality of the event vertex, reconstructed vertices are given a "rank." Vertices of low quality or non-collision vertices are given a negative rank. About 38% of the remaining events have negative rank, representing the largest event-level cut. Following previous FTPC analyses [77, 81, 82], I have restricted the $z$-location of the vertex to $-50$ cm $< z_{\mathrm{vertex}} < 50$ cm (Fig. 19). This cut excludes about 37% of the remaining events with a primary vertex with positive rank.

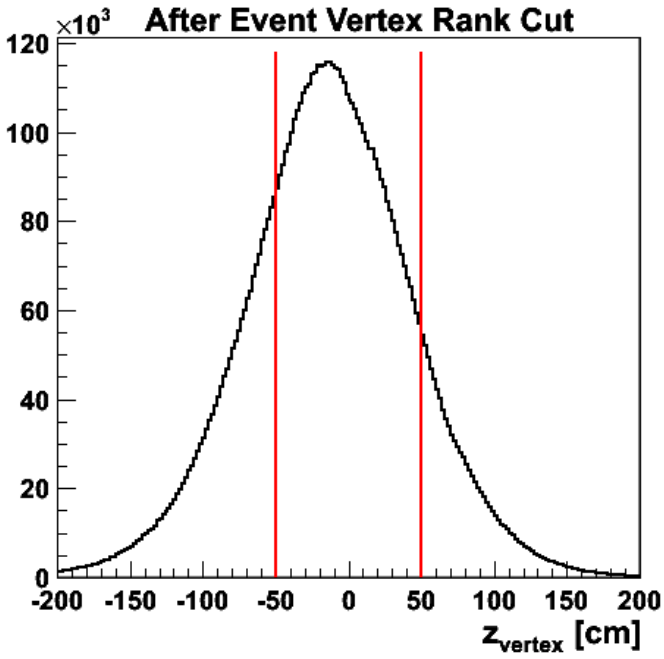


Fig. 19.: Event vertex distribution after cutting on vertex rank. The distribution is biased toward negative $z$ since the event triggers on a high-energy event in the forward direction. The restriction $-50 < z_{\text{vertex}} < 50$ cm excludes $\approx 37\%$ of events.

## E. Auto-correlation

When one is studying two-particle correlations from overlapping subsystems, it is important to remove "auto-correlation" events, where one particle registers hits in both detectors. In the specific case of the FMS and the FTPC, this could occur when a charged particle leaves a track in the FTPC and deposits sufficient energy in the FMS to reconstruct as a "photon." In 2008, the FMS gain was sufficiently non-uniform that in certain low-threshold towers a hadronic shower could leave enough energy to satisfy the high-tower ADC condition. These events are not of interest to this correlation analysis, and an auto-correlation veto has been developed to exclude them.

As a charged particle traverses the FTPC, it experiences the STAR solenoidal magnetic field. For the 2008 run, the solenoidal field was "reversed full field," i.e. full strength of 0.5 T in the $-z$-direction. This solenoidal field introduces an azimuthal progression to the charged particle trajectory. As the charged particle approaches the pole-tip, it experiences a radial fringe field, which counters the azimuthal kick of the solenoidal field. The net azimuthal kick of the charged particle results in a $\phi$-offset between events reconstructed in the FMS and the identical events reconstructed in the FTPC.

If one only considers the azimuthal kick for the solenoidal field, one can use the well-known formula

$$\begin{aligned} p_T &= cqBR \\ \gamma m R \frac{d\phi}{dt} &= cqBR \\ \Delta\phi &= cqB\Delta t/\gamma m, \end{aligned} \tag{4.1}$$

where $p_T$ is the momentum component in units of GeV/c transverse to the magnetic

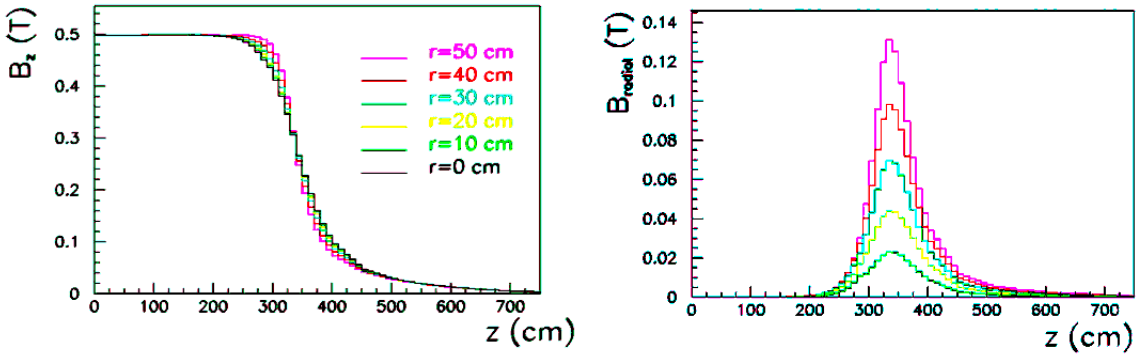


(a) (b)

Fig. 20.: The $z$-dependence of the STAR (a) solenoidal field and (b) radial field.

field, $c$ is the speed of light in m/ns, $q$ is the charge of the particle in units of positron charge, $B$ is the magnetic field in Teslas, and $R$ is the radius of curvature in meters. To determine the amount of time ($\Delta t$) the charged-particle is in the magnetic field, one can utilize the fact that the axial field has no effect on the axial motion of the particle, i.e. $dp_z/dt = 0$, and, thus,

$$\Delta z = p_z \Delta t / \gamma m. \tag{4.2}$$

Equation 4.1 can, then, be expressed

$$\Delta \phi = cqB\Delta z / p_z. \tag{4.3}$$

Thus, the expectation is a $1/p_z$-like dependence to the azimuthal kick in the charged-particle trajectory.

Referring to field maps of the STAR magnetic field (Fig. 20), one can also work out a more informed numerical prediction. If one approximates the solenoidal field as a step-wise function from $0 < z < 350$ m and the fringe field as a step-wise function

from $300 < z < 400$ cm,

$$\begin{aligned}
\Delta\phi &= c\left(\int B_z dr - \int B_r dz\right)/p_r \\
&\approx c(0.5 \text{ T} \times (p_r/p_z) \times 3.5 \text{ m} \\
&\quad - (3.5/0.4)\,(p_r/p_z) \times 0.1 \text{ T} \times 1 \text{ m})/p_r \\
&\approx (0.53 - 0.26)\,/p_z \\
&\approx 0.27/p_z. \qquad (4.4)
\end{aligned}$$

Since I am only interested in events which are triggered by a $\pi^0$, I need to weed out events where the trigger is fired by a charged hadron, happening upon a low-threshold tower. The first task toward this end is to mask out the two towers which account for nearly one third of the triggers, as discussed in a previous section. Beyond that, I can examine the auto-correlation between charged tracks and the location of the FMS towers. I, then, require that the event contain at least one tower above trigger threshold which does not have an auto-correlated track.

The first step in the auto-correlation veto for towers, is to examine the relation of tower energy to track momentum. Figure 21 demonstrates that the calorimeter response as a function of track momentum seems to separate into two classes of response. This is suggestive of a hadronic-like response for lower energy separating from electromagnetic-like response for higher energy. I set a threshold of 6.5 GeV for outer-calorimeter cells and 8.5 GeV for inner-calorimeter cells below which I define as "hadron-like" and above which I call "electron-like" auto-correlations.

The second step is to examine the angular correlation spectra (Figs. 22 and 23). I define a sample of events (denoted in the figures by blue circles) which I will investigate for $1/p_z$-dependence. It is clear that this sample exhibits offsets from zero in both $\Delta\eta$ and $\Delta\phi$, which I quantify with gaussian fits to the peak. The $\Delta\eta$ offset is

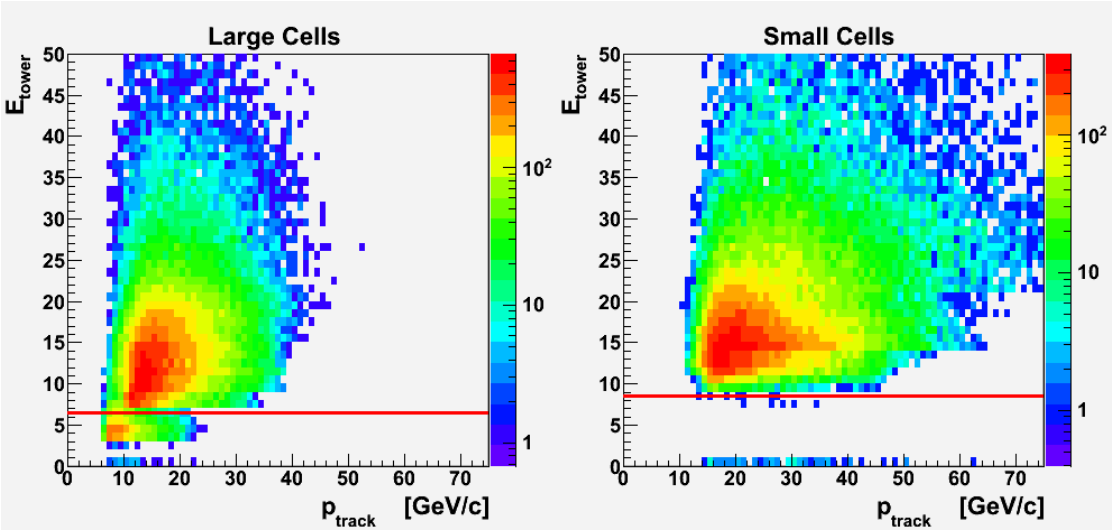


(a) (b)

Fig. 21.: Tower energy as a function of charged-track momentum for (a) outer FMS calorimeter towers and (b) inner FMS calorimeter towers. The appearance of two bands is suggestive of hadronic-like response and electromagnetic-like response in the calorimeter. A red line denotes the cut separating the two responses.

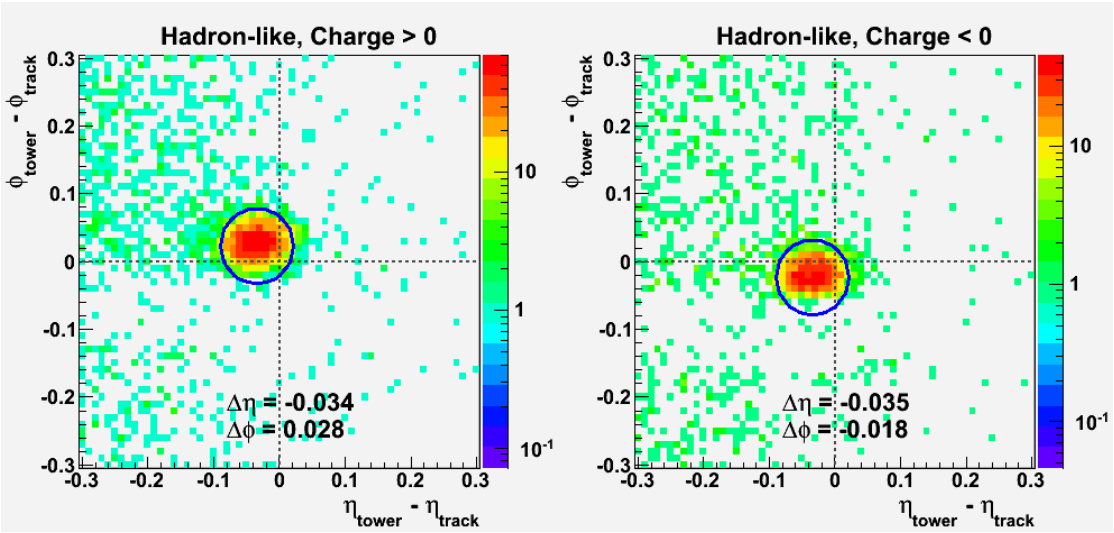


(a) (b)

Fig. 22.: Tower-track correlation spectra for (a)positively charged and (b) negatively charged tracks with hadron-like response. The angles are defined between the track coordinates and tower centroid coordinates relative to the event vertex. Blue circles define the auto-correlation sample to be studied for $1/p_z$-dependence. It is clear that the auto-correlations are offset in $\Delta\eta$ independent of charge sign as well as in $\Delta\phi$ with charge-sign dependence. The labels reflect the centroids of Gaussian fits to the $\Delta\eta$ and $\Delta\phi$ projections of the auto-correlation peaks.

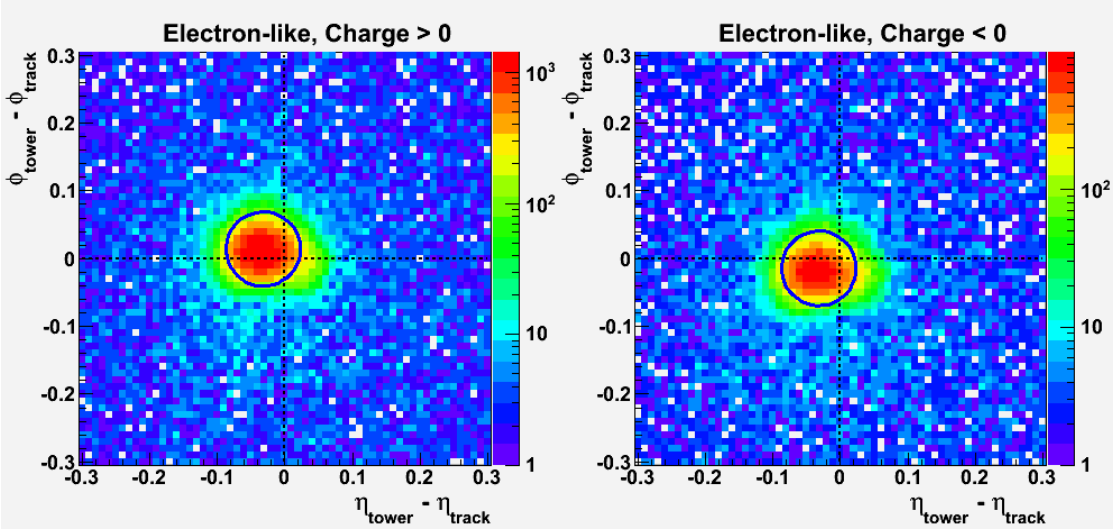


(a) (b)

Fig. 23.: Tower-track correlation spectra for (a) positively charged and (b) negatively charged tracks with electron-like response. The angles are defined between the track coordinates and tower centroid coordinates relative to the event vertex. Blue circles define the auto-correlation sample to be studied for $1/p_z$-dependence. As in Fig. 22, it is clear that the auto-correlations are offset in $\Delta\eta$ independent of charge sign as well as in $\Delta\phi$ with charge-sign dependence. The Gaussian fits to (a) reflect offsets of $\Delta\eta = -0.032$ and $\Delta\phi = 0.0097$, while Gaussian fits to (b) reflect offsets of $\Delta\eta = -0.032$ and $\Delta\phi = -0.019$.

not charge-sign dependent and is of similar order between hadron-like and electron-like samples. The $\Delta\phi$ offset is charged-sign dependent, in the direction expected for correct discrimination of charge sign. The $\Delta\phi$ offset in hadron-like events is larger than that of the electron-like events. This is consistent with expectation of a sample of lower $p_z$ events.

The final piece to the auto-correlation veto is to evaluate the $1/p_z$-dependence of the $\Delta\phi$ spectra. In Fig. 24 I show the azimuthal auto-correlation, defined by the circular cuts in Figs. 22 and 23, as a function of $p_{z,\ \mathrm{track}}$ scaled by the longitudinal distance traveled in the magnetic field. To extract the dependence, I use a linear fit to a profile of the 2-D histogram for each charge sign, averaging the absolute values of the fitted slopes. The fit is constrained to pass through the origin. I tune the dependence by focusing on data within a width of $\pm 0.04$ of the linear fit. Using the average $z_{\mathrm{vertex}}$ position, the average dependence becomes

$$\langle|\Delta\phi_{\mathrm{hadron}}|\rangle = 0.25/p_z \tag{4.5}$$

$$\langle|\Delta\phi_{\mathrm{electron}}|\rangle = 0.28/p_z. \tag{4.6}$$

Thus, the dependence is very close to the field map calculation (Eq. 4.4).

This procedure works equally well considering reconstructed photons. It is certainly possible for an energetic hadron to leave a cluster of energy which reconstructs in the FMS as a photon. Thus, it is useful to exclude photons with an auto-correlated track. Following the same procedure used with the FMS trigger towers, I can evaluate the $1/p_z$-dependence of photon-track auto-correlations (Fig. 25). The dependence is similar to that observed in the trigger towers. Using the average $z_{\mathrm{vertex}}$ position, the average dependence becomes

$$\langle|\Delta\phi_{\mathrm{hadron}}|\rangle = 0.25/p_z \tag{4.7}$$

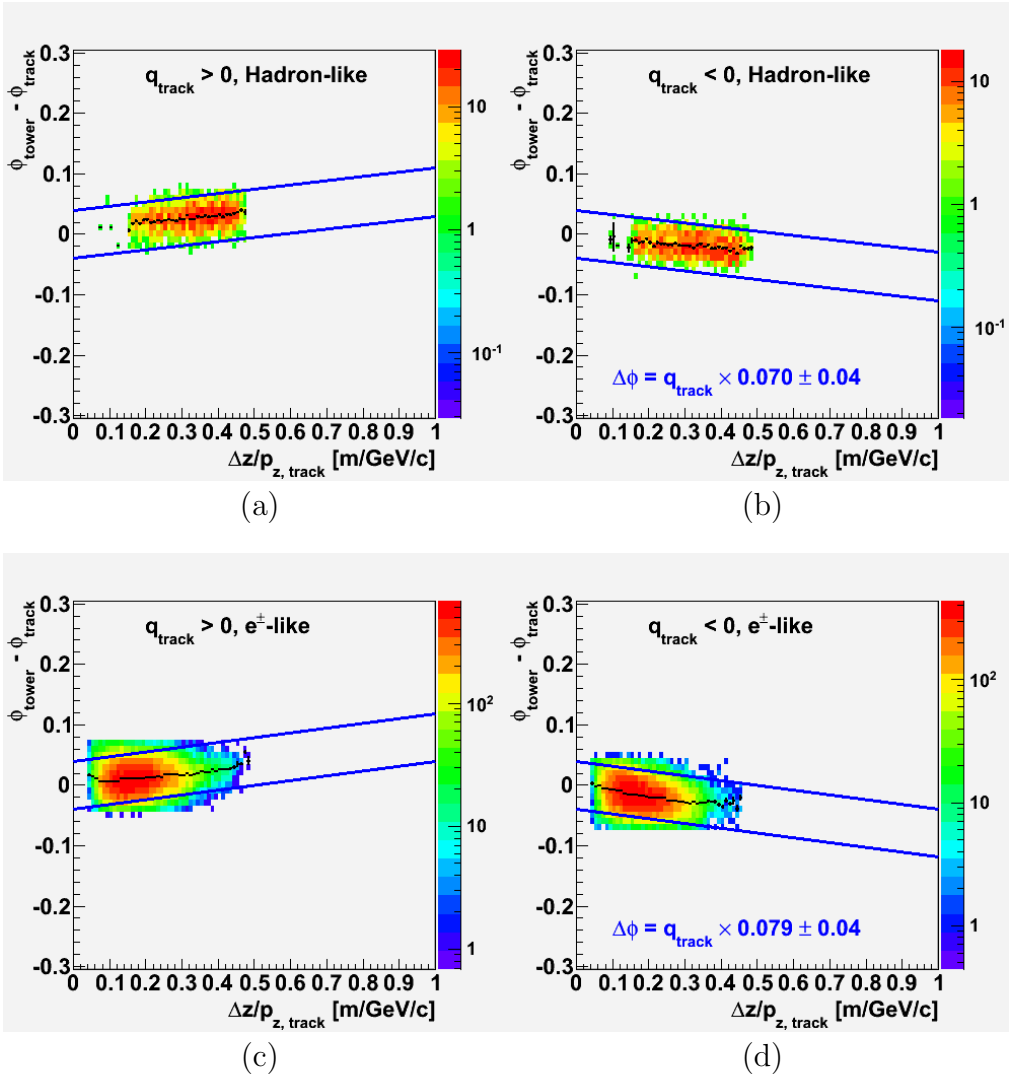


Fig. 24.: $\Delta\phi = \phi_{\text{tower}} - \phi_{\text{track}}$ as a function of $\Delta z/p_{z,\text{track}}$, where $\Delta z$ is the effective longitudinal distance traversed through the STAR solenoidal field for hadron-like response of (a) positively charged and (b) negatively charged tracks as well as electron-like response of (c) positively charged and (d) negatively charged tracks. There is clear charge-sign dependence. The dependence is determined by means of a linear fit to a profile of the 2-D histogram (black points). The absolute value of the slope is averaged across the charge signs. The fit is tuned by focusing on data within a width of $\pm 0.04$ (blue lines) around the linear fit.

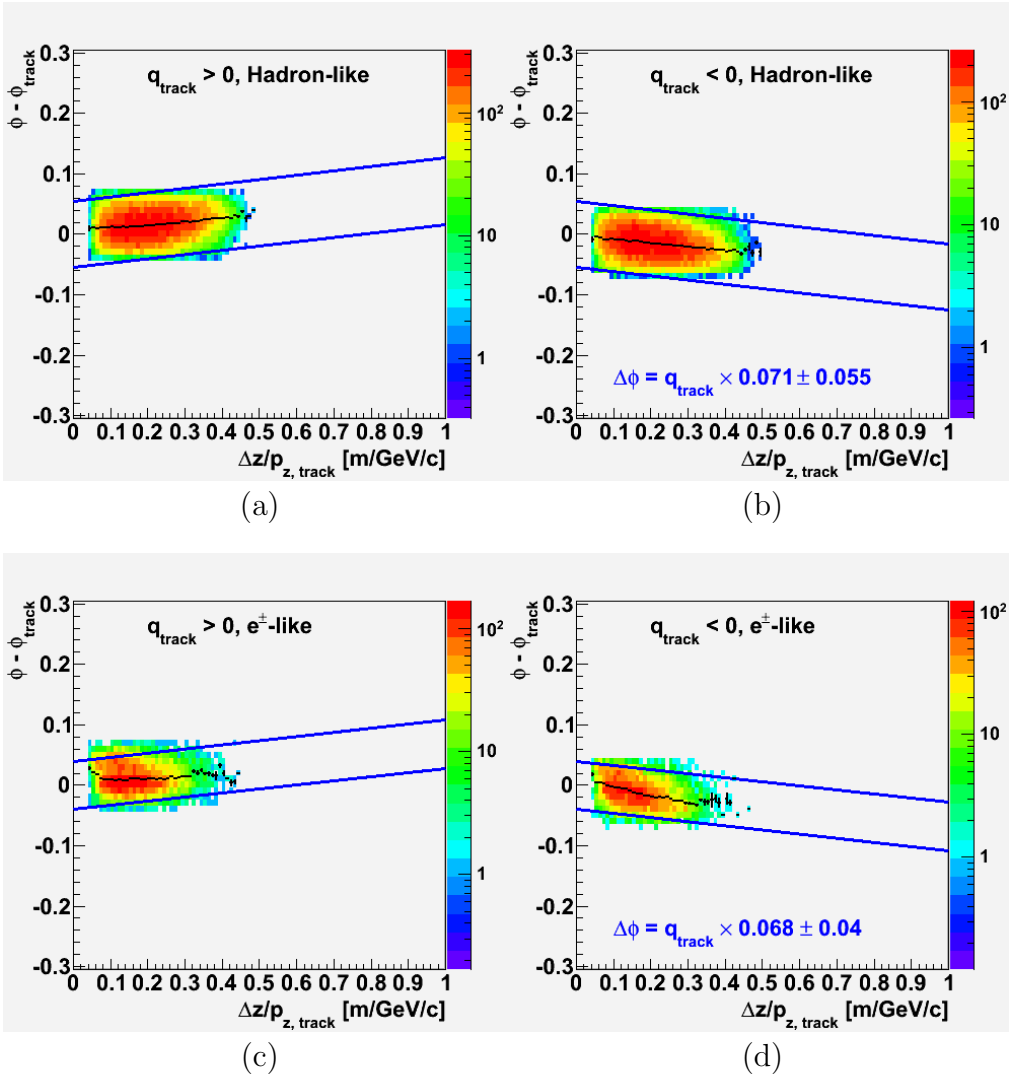


Fig. 25.: $\Delta\phi = \phi_\gamma - \phi_{\rm track}$ as a function of $\Delta z/p_{z,{\rm track}}$, where $\Delta z$ is the effective longitudinal distance traversed through the STAR solenoidal field for hadron-like response of (a) positively charged and (b) negatively charged tracks as well as electron-like response of (c) positively charged and (d) negatively charged tracks. There is clear charge-sign dependence. The dependence is determined by means of a linear fit to a profile of the 2-D histogram (black points). The absolute value of the slope is averaged across the charge signs. The fit is tuned by focusing on data within a width of $\pm 0.04$ (blue lines) around the linear fit.

$$\langle|\Delta\phi_{\text{electron}}|\rangle \;=\; 0.24/p_z. \tag{4.8}$$

Again, the dependence is very close to the field map prediction (Eq. 4.4).

The offset in $\Delta\eta$ is somewhat perplexing. One possibility is to consider the implications of an $\eta$-offset on the $z$-coordinate between the photon and the track. If the reconstruction code misplaces the $z$-location of the photon, this would translate into an $\eta$-offset. There is some ambiguity on the proper $z$-location of the photon within an FMS tower. Nominally, the location has been assumed to be the shower-maximum location. If the real location is further down the tower, one should observe $\eta_{\text{reco}} - \eta_{\text{real}} < 0$. Moreover, the offset for hadron-like events should be different from electron-like events. Hadronic showers should evolve slower in the FMS towers than electromagnetic showers, pushing the real $z$-location even further down the beam leading to smaller reconstructed $\eta$. Examining the $\Delta\eta$ offset for all towers, regardless of whether they could fire the trigger, I find offsets of

$$\langle\Delta\eta_{\text{hadron}}\rangle \;=\; -0.040 \tag{4.9}$$

$$\langle\Delta\eta_{\text{electron}}\rangle \;=\; -0.031. \tag{4.10}$$

This translates to an effective $z$-shift of 31 cm for hadron-like towers and 24 cm for electron-like towers. If the issue is, indeed, misplaced photon $z$-location, then the results in Eqs. 4.9 and 4.10 are consistent with hadronic showers developing slower than electromagnetic showers. However, the magnitude of such a misplacement is quite large and remains something of a mystery.

### F. Spin Sorting

RHIC is able to store polarized beams in both rings, allowing one to study single-spin effects as well as double-spin effects. Furthermore, RHIC has the capability

to control the spin direction in either beam from bunch to bunch within a beam. This allows one to utilize cross-section differences and cross-ratio formulations in studying spin-effects. These methods are useful for canceling out non-physical effects like instrumental or luminosity asymmetries. Thus, to utilize RHIC's capability as a "spin-collider" in isolating how changes in the spin direction relate to changes in the observed particle production, one must be able to determine the polarization orientation for each collision.

One important task to assure the quality of the data is to verify that the bunch-crossing distributions make sense. To do this, I compare the measured bunch-crossing distributions to what one expects based on the measured fill patterns. The measured fill patterns are accessible from the RHIC wall-clock monitors, which are able to determine if a particular bunch was actually populated for a particular fill. Nominally, each beam contains one unpopulated or "kicked bunch" and a string of nine consecutive unfilled bunches called the "abort gap." If the bunch crossings are sensible, the measured distribution should be invariant when shifted by the relative offset between the blue and yellow beams. In the case of STAR in 2008, the intended offset was 80 bunch-crossings. To check this offset, the expected fill pattern is compared to the measured distribution when shifted by different offsets. The measured offset is determined by the lowest $\chi^2$ between the expected and measured bunch-crossing distributions.

The bunch-crossing quality check finds that the first several days of the 2008 polarized-proton run contain multiple runs exhibiting an offset of 79 rather than the intended offset of 80. Deeper investigation finds a tight correspondence between these runs of bunch-crossing offset 79 and the exclusion from the STAR trigger mix of a particular configuration called TOF-TPX. No explanation has been found for this feature, but the correlation is undeniable. Since a confident understanding of the

bunch-crossings is essential for a spin analysis, these early runs must be excluded from the analysis. Since these runs happen to correspond to a period of relatively low RHIC luminosity, the effect on statistics is not significant.

Further investigation finds that a file containing information for trigger readout, known as a tier-1 file, was changed during the early part of the polarized-proton run. Examining FMS photon distributions reveals the FMS exhibited highly suppressed photon population in the north half of the detector prior to the change in tier-1 file. No documented explanation for the change has been found, but the use of such runs would introduce even more severe instrumental asymmetries into the data. Thus, runs prior to the change in tier-1 file must be excluded from the analysis. Once again, however, these runs correspond to a relatively low RHIC luminosity period. Thus, the effect on statistics is relatively minor.

As a sanity check, it is useful to examine the resulting pion asymmetries for the runs passing the bunch-crossing quality assurance. Since slow detector information is not necessary for this check, the much larger data set known as FMS-fast, which only demands readout of the fast detectors, is available. I have calculated the asymmetry as a function of $x_F$ (Fig. 26) for $\pi^0$'s satisfying the 2008 FMS high-tower trigger condition. The pions are required to satisfy a transverse momentum constraint of $2 < p_T < 5$ GeV/c. These pions show an average pseudorapidity of $\langle\eta\rangle = 3.2$. These asymmetries are small for low $x_F$ and rise quickly at high $x_F$. Asymmetries for $x_F < 0$ are consistent with zero. In Fig. 26, I show these asymmetries in comparison with published asymmetries from the Forward Pion Detector (FPD), a modular predecessor to the FMS, taken in 2006 at $\langle\eta\rangle = 3.3$ [9]. While the FPD data are at similar pseudorapidity to the FMS data, the FPD data have a different set of transverse momentum constraints. Furthermore, the effective $p_T$-$x_F$ coverage of the two detectors is quite different, as the FPD is a modular detector while the FMS is near-hermetic.

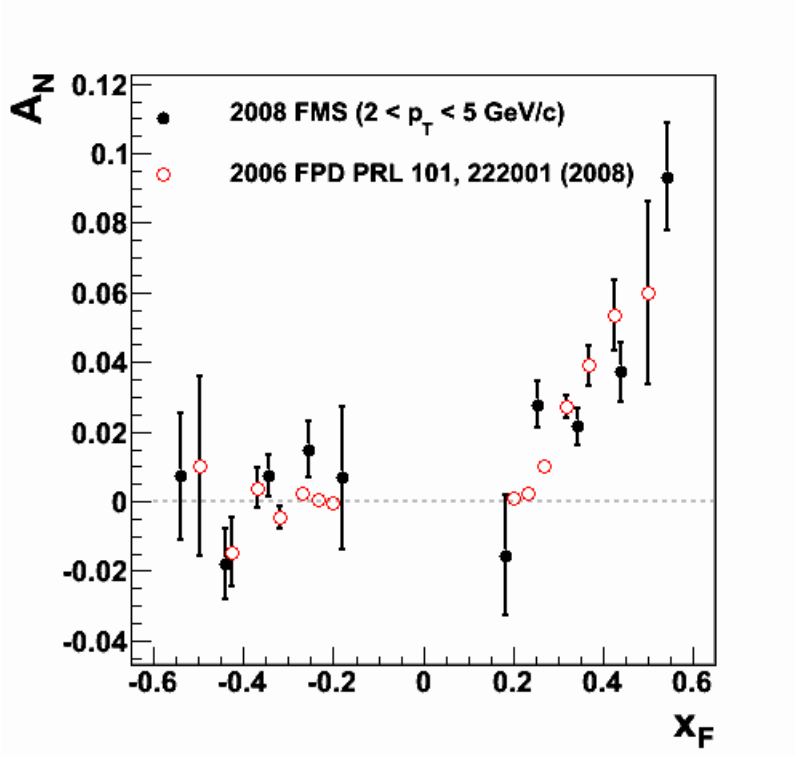


Fig. 26.: $A_N$ in $x_F$ bins for $\pi^0$'s satisfying the 2008 FMS high-tower trigger condition. The FMS data are shown in comparison with published FPD data taken in 2006 [9]. FMS $\pi^0$'s are required to satisfy $2 < p_T < 5$ GeV/c and have an average pseudorapidity of 3.2, compared to the FPD data with an average pseudorapidity of 3.3 and a different set of $p_T$ constraints.

Nevertheless, the 2008 FMS data show rather sensible agreement with the previous FPD result [9], suggesting the spin states are well understood.

# CHAPTER V

## EVENT-LEVEL ANALYSIS

Prior to correlating particles from the desired events, it is important to develop a set of appropriate single-particle cuts to select the desired correlation constituents. For the FTPC, one should consider cuts to optimize the tracking capability as well as reduce pile-up due to the slow-detector readout. For FMS events, one should focus in part on minimizing the effects of the non-uniform trigger.

### A. Track Flag

Within the STAR computing framework one of the standard methods for selecting tracks from a particular subsystem is the track flag. The track flag is a four-digit number where the first digit distinguishes pile-up tracks from real tracks, the second digit describes the detectors included in the fit, and the final two digits describe the status of the fit. For the purpose, here, tracks of interest are those from the FTPC where the primary vertex is included in the track fit. Specifically, these tracks are denoted with a track flag of 0801. The first 0 corresponds to real tracks. The 8 denotes FTPC tracks with the primary vertex. The final 01 denotes a track with a "good fit." For this analysis, tracks are required to return a flag of 801.

### B. Track Fit Quality

The quality of the track fit depends on the number of available points in the fit. The number of available fit points is equivalent to the number of hits in the FTPC plus the primary vertex. One way to select the most reliable tracks is to set a lower limit on the ratio of the number of fitted hit points to the number of possible hit points

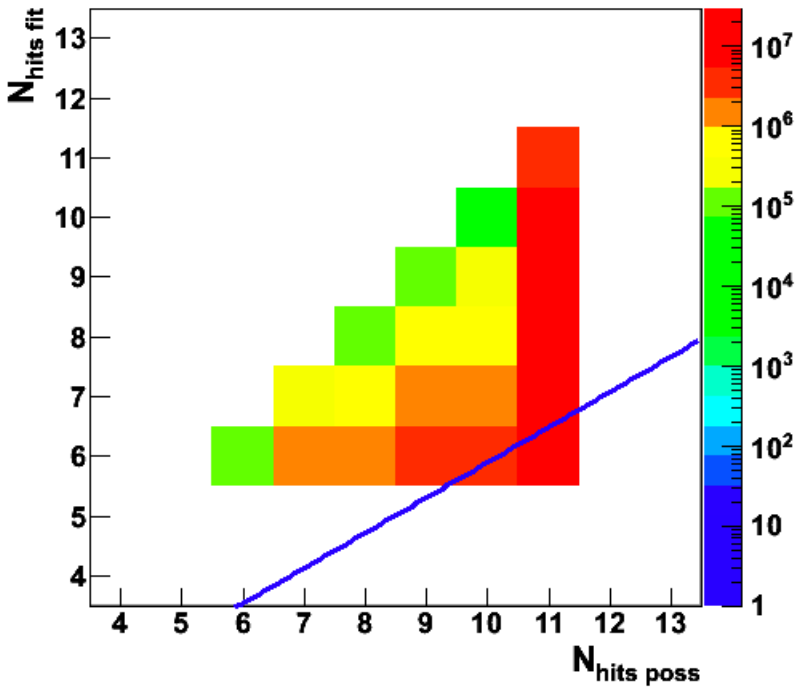


Fig. 27.: Number of hit points fit as a function of the number of possible hit points in a reconstructed track. The blue line denotes the minimum number of fit points, $N_{\text{hits fit}}/N_{\text{hits poss}} > 0.59$. The cut effectively excludes only the case where 6 points are fitted out of a possible 11.

for the event. Specifically, I have required $N_{\text{hits fit}}/N_{\text{hits poss}} > 0.59$, where $N_{\text{hits fit}}$ is the number of hit points fit and $N_{\text{hits poss}}$ is the number of possible hits (Fig. 27).

### C. Distance of Closest Approach to the Event Vertex

One of the largest concerns with a slow-readout detector such as the FTPC is the presence of pile-up tracks. These occur when a particle track from an out-of-time collision reconstructs as though it occurred during the current collision. One possible situation for this is a non-trigger collision leaving drifting ions in the FTPC. This

collision is followed by a triggering collision which reads out the current, or "prompt," tracks as well as those formed by the drifting ions from the previous event. One way to reduce the amount of pile-up in a sample is to restrict the distance of closest approach (DCA) of the track to the primary event vertex. The DCA is the closest distance to the event vertex of an extrapolation of the measured track helix. Since the track reconstruction applies the drift calibration according to the triggered event, pile-up tracks will tend to reconstruct farther from the collision vertex than prompt tracks, typically resulting in a larger DCA.

To get some idea of an appropriate DCA cut for these data, I make two assumptions. First, I assume each yield is a sum of a luminosity-independent signal and a luminosity-dependent background. Second, I assume the luminosity dependence in the background is linear in the event collision rate. Thus, by pulling data from two different runs with two different collision rates from the same fill, I can construct a data-driven background subtraction to evaluate the DCA signal as a function of track transverse momentum. Consider

$$\begin{aligned} N_{\text{meas}}^{\text{Low}} &= N_{\text{true}} + C \times R^{\text{Low}} \\ N_{\text{meas}}^{\text{High}} &= N_{\text{true}} + C \times R^{\text{High}} \\ N_{\text{true}} &= N_{\text{meas}}^{\text{Low}} - \frac{\Delta N_{\text{meas}}}{R^{\text{High}}/R^{\text{Low}} - 1}, \end{aligned} \tag{5.1}$$

where $N_{\text{meas}}^{\text{Low}}$ and $N_{\text{meas}}^{\text{High}}$ denote the measured yield for low and high collision rates, $\Delta N_{\text{meas}} = N_{\text{meas}}^{\text{High}} - N_{\text{meas}}^{\text{Low}}$, $N_{\text{true}}$ denotes the rate-independent signal or "true" yield, $R^{\text{High}}$ and $R^{\text{Low}}$ denote the rates of the two samples, and $C$ is the constant of proportionality. Figure 28 shows the results of the aforementioned procedure. The measured yields have been normalized to match the number of events in each sample. The results suggest a $p_T$-dependent DCA cut is appropriate. Conservatively, I

Table I.: DCA cut as a function of $p_T$ (Fig. 29).

| Range of $p_T$ | Upper Limit on $r_{\mathrm{DCA}}$ |
|---|---|
| $p_T < 0.3$ GeV/c | $r_{\mathrm{DCA}} < 2$ cm |
| $0.3 < p_T < 1.0$ GeV/c | $r_{\mathrm{DCA}} < 349/140 - (23/14) \times p_T$ cm |
| $p_T > 1.0$ GeV/c | $r_{\mathrm{DCA}} < 0.85$ cm |

estimate upper limits of 2.5 cm below $p_T = 0.5$ GeV/c, 1.5 cm from $0.5 < p_T < 1.5$ GeV/c, and 1 cm above $p_T = 1.5$ GeV/c. Furthermore, it is clear from Fig. 28 that above $p_T = 3$ GeV/c, the yield is entirely background. The data-driven cut can be tuned to optimize removal of the pile-up background, which is critical to this analysis. Figure 29 shows the DCA as a function of transverse momentum with a tuned cut summarized in Table I.

### D. Pseudorapidity

For this correlation analysis, the relevant events are those with two particles from the same jet. Thus, the associated tracks need to cover a pseudorapidity range similar to that of the trigger. To this end, tracks are selected from the west FTPC, which roughly covers the range of $2.5 < \eta < 4.0$ (Fig. 30). Due to the physical layout of the detectors, a cut of $\eta_{\mathrm{track}} > 0$ is sufficient to select the west FTPC.

### E. Azimuthal Sector

Throughout the course of the 2008 run, the FTPC was afflicted with various hardware issues. In particular, one of the ten read-out (RDO) boards was dead for the duration of the $p + p$ run. This restricted one $\phi$-sector to a maximum of six detector hits and

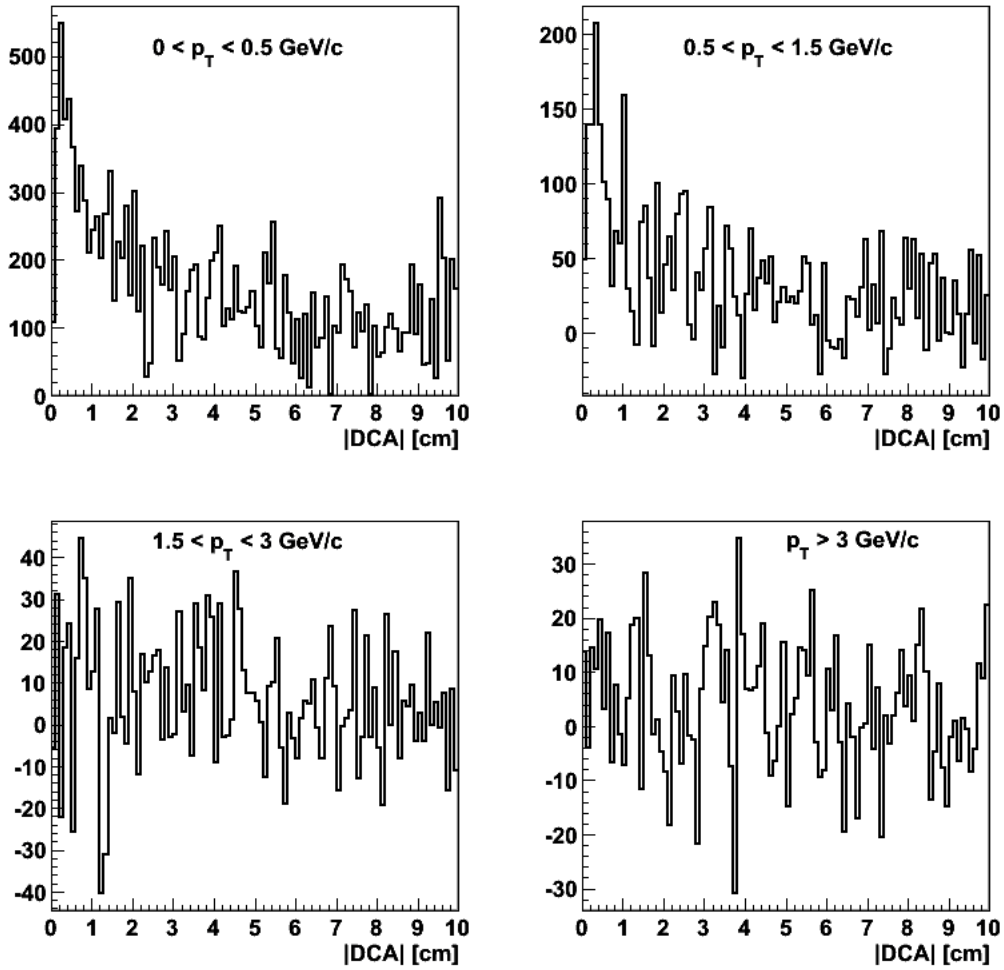


Fig. 28.: Data-driven background-subtracted yields as a function of track DCA for four different bins of track transverse momentum. Above $p_T > 3$ GeV/c, it appears the yield is entirely background. The other panels suggest a $p_T$-dependent DCA cut, which tightens as $p_T$ increases.

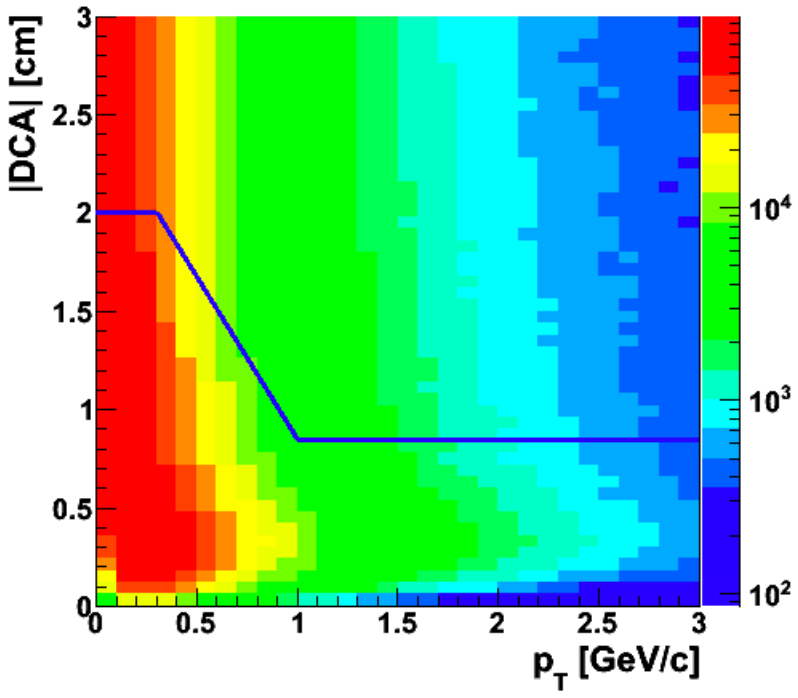


Fig. 29.: DCA magnitude as a function of transverse momentum. The $p_T$-dependent cut used in the analysis is denoted by a blue line and summarized in Table I.

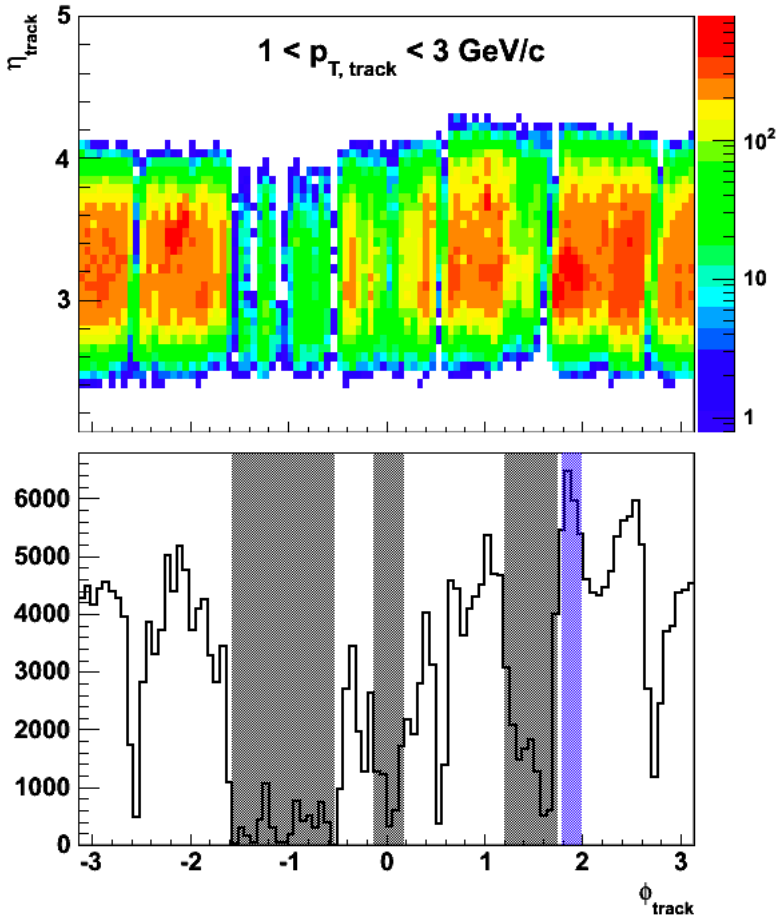


Fig. 30.: Charged-particle track $\eta - \phi$ distribution for tracks reconstructed within the range of $1 < p_T < 3$ GeV/c. The shaded regions denote cuts in $\phi$ from hardware failures. The blue shaded region is excluded for runs 9065034 and following. These cuts are summarized in Table II

Table II.: Regions of $\phi_{\text{track}}$ excluded due to hardware failures in the FTPC (Fig. 30).

| Range of Runs | Regions of $\phi$ Excluded |
|---|---|
| All Runs | $-1.571 < \phi < -0.524$ |
| All Runs | $1.2 < \phi < 1.75$ |
| All Runs | $-0.125 < \phi < 0.188$ |
| Runs 9065034 and Following | $1.795 < \phi < 1.995$ |

an additional sector to a maximum of eight detector hits. Furthermore, starting from run 9065034, a front-end module in an additional sector was dead. This and further hardware issues suggest a cut on track $\phi$ to exclude troublesome electronics regions (Fig. 30). The cuts implemented are summarized in Table II.

## F. Embedding

To quantify the tracking efficiency of the FTPC, one needs to understand the detector response including the effects of pile-up. Simple Monte Carlo simulations are limited in the degree to which pile-up effects can be simulated. One way to incorporate these effects is to generate Monte Carlo tracks and embed the simulated detector response into real data files. The track reconstruction code does not distinguish between simulated ADC's and real data ADC's, allowing the code to recover some fraction of the simulated ("thrown") tracks. Reconstructed tracks which correspond to a thrown track are termed "matched" tracks. The ratio of the number of matched tracks to thrown tracks is the calculated tracking efficiency. Because the real data files contain pile-up effects, backgrounds, etc., this embedding procedure is not limited in the ways of pure Monte Carlo simulations. To calculate the FTPC efficiency, 40,000

Monte Carlo charged pions have been generated for each charge state and six bins of thrown $p_T$: 0.2-0.5 GeV/c, 0.5-1.0 GeV/c, 1.0-1.5 GeV/c, 1.5-2.0 GeV/c, 2.0-3.0 GeV/c, and 3.0-4.0 GeV/c. Studies [77] have shown the efficiency of the FTPC does not begin to drop appreciably in $Au+Au$ collisions until centralities pass 40%, where the multiplicity approaches $dN/d\eta \approx 50$ in the west FTPC region [78]. Including secondary tracks, raw multiplicity approaches $dN/d\eta \approx 38$ in the FTPC for FMS-triggered $p+p$ data. The addition of six Monte Carlo tracks across two units of pseudorapidity per event, thus, keeps the multiplicity below the point where the FTPC efficiency decreases. In order to save computing resources, one track from each $p_T$ bin is embedded in each event. The Monte Carlo tracks are embedded into a representative sample of FMS-slow triggered data. The simulation is generated flat within the $p_T$ bins as well as the angular range of $2.25 < \eta < 4.45$ and $-\pi < \phi < \pi$.

As a means of quality control, embedding-to-data comparisons have been performed on a sample of embedding with tracks thrown within the range of $1 < p_T < 2$ GeV/c. Out of the box, the matched-track distributions show substantial difference from real-data distributions. In particular, distributions for the number of fitted hit points tend to be much higher in the embedded tracks. Also, regions of low efficiency in the $\phi$ distributions tend to be less exaggerated in the embedding. Further, intra-sector fluctuations in the embedding do not agree with those seen in the real data. Investigation by FTPC experts has shown that gain tables used in both the real data and simulation are not properly optimized for the $p+p$ run. Additionally, they have discovered that the ADC conversion used in the simulation is also not properly optimized. Application of the new gain tables would require a full reproduction of the 2008 FMS-slow dataset. The impact of this analysis simply cannot justify the allocation of resources necessary for this task, as the estimated gain in statistics is $\approx 30\%$.

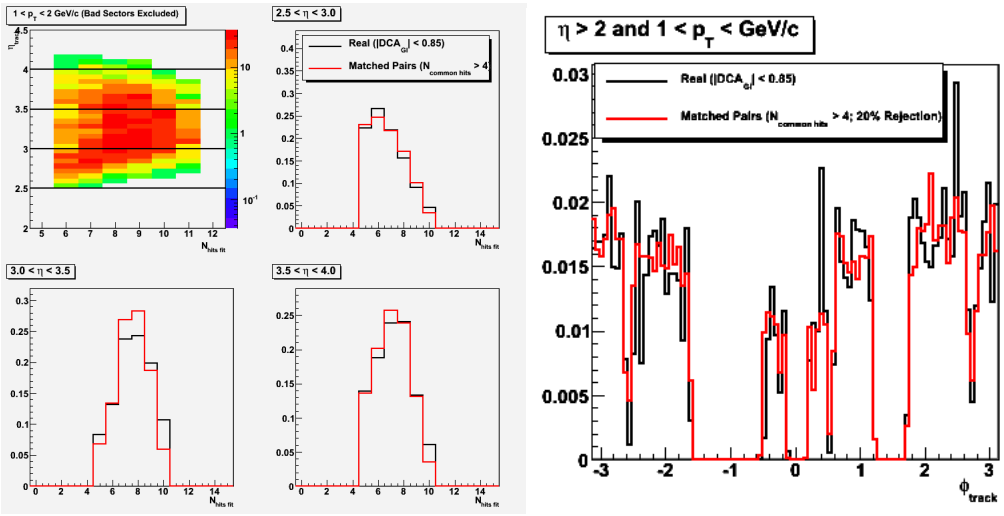


(a) (b)

Fig. 31.: (a) $N_{\text{fit}}$ distribution and (b) $\phi$ distribution for real data tracks and matched embedding tracks. The $N_{\text{fit}}$ distribution is shown for three bins of pseudorapidity utilizing a 25% rejection scheme. The $\phi$ distributions utilize a 20% rejection scheme. The $\phi$ distribution has been corrected for trigger bias in the FMS.

Without the justification to perform a full reproduction of the data, a "quick fix" has been developed. The true hit efficiency can be estimated by randomly rejecting a certain fraction of hits in each event. In Fig. 31, I show comparisons of matched tracks to real data for $N_{\text{fit}}$ and $\phi$ distributions utilizing the random rejection scheme. The comparisons utilizing the rejection scheme are greatly improved over the out-of-the-box distributions. In addition to the hit rejection, the $\phi$ distributions are corrected for FMS trigger bias. By convoluting the raw trigger spectrum with the acceptance-corrected correlation distribution (Fig. 44), one can produce the expected fluctuations in the track distribution due to the trigger prior to FTPC acceptance effects. Dividing this distribution out of the measured data distribution effectively removes the effects of the trigger from the comparison of data to matched embedding tracks.

It is necessary, then, to optimize the hit-rejection percentage for the best comparison between matched-embedding tracks and real data. A procedure has been developed to maximize the agreement for the $N_{\text{fit}}$ distributions and the $\phi$ distributions. First, the matched track and real data distributions are normalized. Then, absolute values of the differences between the various bins are fitted with a constant. The values of these constants are then plotted in relation to the hit-rejection percentage. This relation is fit with a quadratic, the minimum of which is taken as the optimum rejection percentage. Examples of this procedure are shown for $N_{\text{fit}}$ distributions in Fig. 32 and $\phi$ distributions in Fig. 33. The $\phi$ optimization has been performed four times, rebinning the histograms by factors of 4, 6, 8, and 10 to ensure binning fluctuations are stable. The final $\phi$ optimization is taken as an average of the four values. The final optimized hit-rejection percentage is taken as an average of the $N_{\text{fit}}$ optimization and the $\phi$ optimization and is reported as $21.6 \pm 3\%$.

Since the embedding is generated flat in $\eta$ and flat within the various thrown

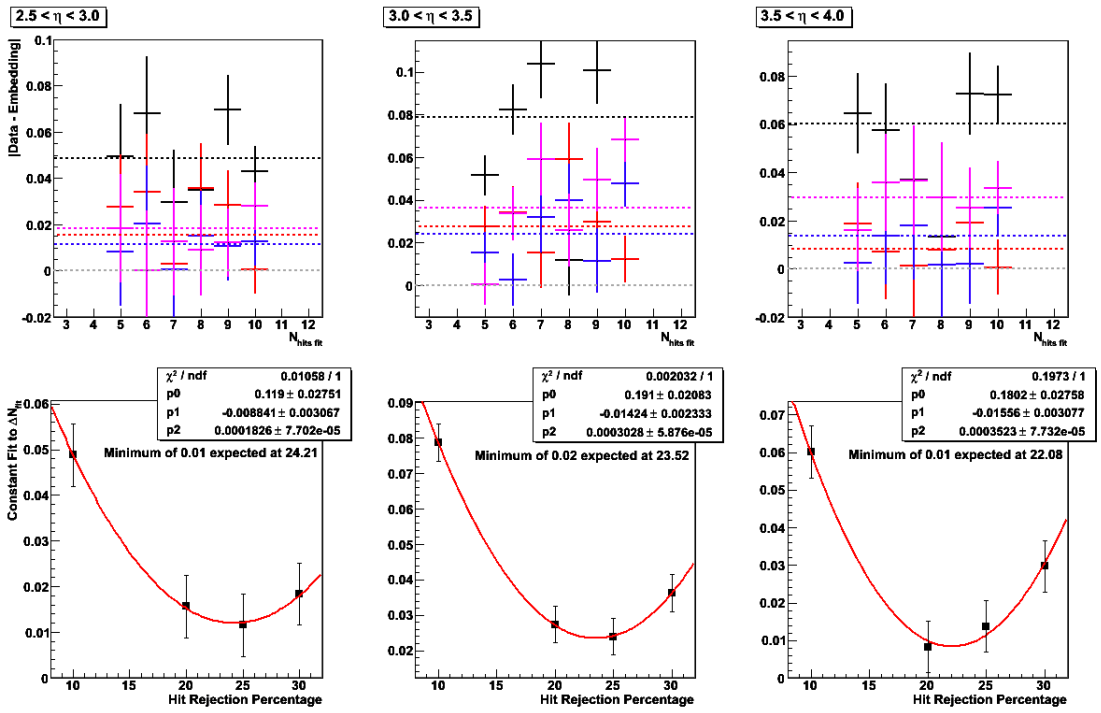


Fig. 32.: Optimization of the hit rejection efficiency for $N_{\rm fit}$. Combining $N_{\rm fit}$ and $\phi$ optimization (Fig. 33), the optimized rejection percentage is found to be $21.6 \pm 3\%$.

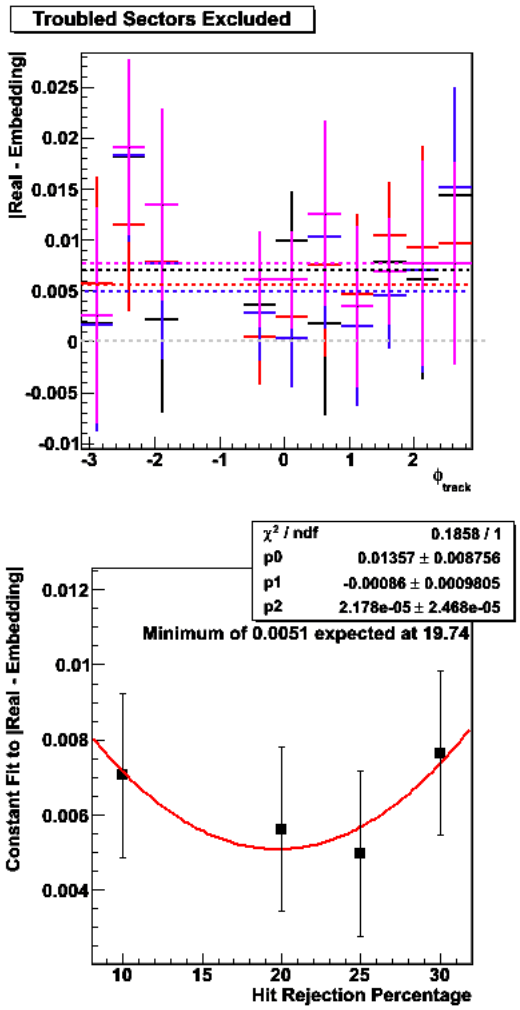


Fig. 33.: Optimization of the hit rejection efficiency for $\phi$. Combining $N_{\text{fit}}$ (Fig. 32) and $\phi$ optimization, the optimized rejection percentage is found to be $21.6 \pm 3\%$.

$p_T$ bins, for efficiency calculations, a weighting procedure must be used to simulate realistic distributions for thrown $\eta$ and $p_T$. First, a simple scaling is used to correct for the non-uniform bin densities. Since the number of tracks thrown in each bin is constant, this is simply scaling by the relative width of the bins. For $\eta$ and $p_T$, I assume the $p_T$ spectrum to be exponential

$$\frac{d^2N}{d\eta dp_T} = A(\eta) \times p_T \mathrm{e}^{-B(\eta)p_T}. \tag{5.2}$$

If I assume $p_T$ does not depend strongly on $\eta$, then I can simply factorize the problem into an $\eta$ weight and a $p_T$ weight. However, if I consider the dependence of $\eta$ on $p_T$, I can utilize the average $p_T$ as a function of $\eta$ to obtain $B(\eta)$

$$\begin{aligned}
\langle p_T \rangle (\eta) &= \frac{\int dp_T \frac{d^2N}{d\eta dp_T} p_T}{\int dp_T \frac{d^2N}{d\eta dp_T}} \\
&= \frac{\int dp_T A(\eta) \times p_T \mathrm{e}^{-B(\eta)p_T} p_T}{\int dp_T A(\eta) \times p_T \mathrm{e}^{-B(\eta)p_T}} \\
&= \frac{2A(\eta)/B^3(\eta)}{A(\eta)/B^2(\eta)} \\
&= \frac{2}{B(\eta)}.
\end{aligned} \tag{5.3}$$

Thus, the pseudorapidity dependence of average transverse momentum will yield $B(\eta)$. To obtain $A(\eta)$, I consider $dN/d\eta$

$$\begin{aligned}
\frac{dN}{d\eta} &= \int dp_T \frac{d^2N}{d\eta dp_T} \\
&= \int dp_T A(\eta) p_T \mathrm{e}^{-B(\eta)p_T} \\
&= \frac{A(\eta)}{B^2(\eta)}.
\end{aligned} \tag{5.4}$$

Thus, given $B(\eta)$ from the average transverse momentum, I can obtain $A(\eta)$ from the distribution of $dN/d\eta$.

Since nearly all $p+p$ data which exist for the FTPC are those I am analyzing, I

turn to peripheral nuclear data to approximate the shapes of the spectra of interest. An initial value for $B(\eta)$ is obtained by performing a linear fit to $\langle p_T \rangle$ as a function of $\eta$ for peripheral (40-60% centrality) $Au + Au$ minimum-bias data [79]. To obtain an initial value for $A(\eta)$, a power-law fit is performed to peripheral (50-60% centrality) $Cu + Cu$ minimum-bias data [80]. To tune the expression to reflect the harder $p_T$ spectrum from FMS-triggered data, I have varied the linear dependence of $\langle p_T \rangle$ on $\eta$. I, then, compare the resulting mean $\eta$ and $p_T$ for matched track distributions to those from real data. I have selected for the weighting distribution the linear dependence which achieves the best agreement between reconstructed embedding and measured data in terms of $\eta$ and $p_T$. The final expression used to weight the thrown embedding tracks is

$$\begin{aligned} \frac{d^2N}{d\eta dp_T} &= \frac{19}{(\eta_{\text{thrown}} - 1.9)^{0.66}} \left( \frac{2}{0.71 - 0.06\eta_{\text{thrown}}} \right)^2 \\ &\quad \times p_{T,\text{thrown}} \exp\left( -\frac{2}{0.71 - 0.06\eta_{\text{thrown}}} p_{T,\text{thrown}} \right). \end{aligned} \tag{5.5}$$

So, in evaluating distributions of matched tracks, the entries are weighted by Eq. 5.5, based on the thrown values of $\eta$ and $p_T$.

With a sensible expression to simulate physical underlying distributions, track cuts and efficiencies can be evaluated. Critical to the correlation asymmetry analysis is the reliability of charge separation. Figure 34 shows the fraction of tracks reconstructed with incorrect charge sign as a function of transverse momentum. Below 2 GeV/c, the fraction stays below 25%. Above 2 GeV/c, this fraction approaches 35%. Thus, 2 GeV/c serves as a reasonable upper-limit on track $p_T$. Furthermore, this upper-limit is consistent with prior analyses of FTPC data [77, 82].

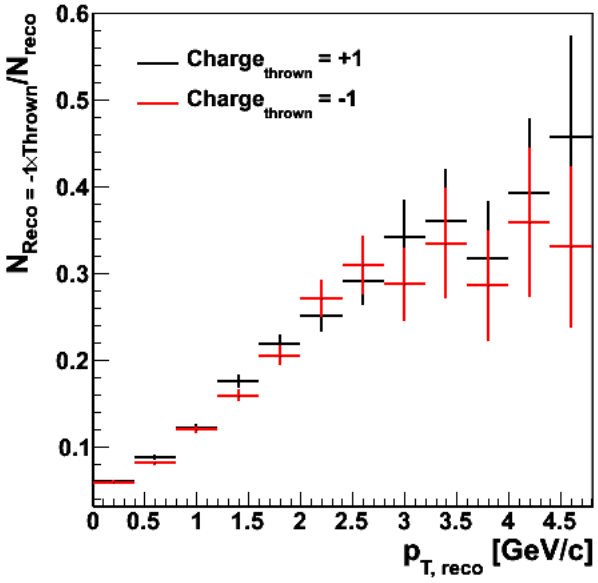


Fig. 34.: The fraction of tracks reconstructed with incorrect charge sign as a function of $p_T$. Above 2 GeV/c, the ratio approaches 35%, setting a sensible upper-limit on reliable FTPC tracking.

## G. Transverse Momentum Windows

It is useful to understand the efficiency of the FTPC in terms of pseudorapidity and transverse momentum. To this end, I divide the sample into two bins of transverse momentum: a "low-$p_T$" bin for $0.5 < p_T < 1.0$ GeV/c and a "high-$p_T$" bin for $1.0 < p_T < 2.0$ GeV/c. Finer binning than this is not practical for the amount of real data statistics available.

One way to visualize the efficiency is in how it relates to "real" values and "measured" values. For instance,

$$\frac{dN_{\text{meas}}}{d\eta} = \epsilon\left(\eta\right)\frac{dN_{\text{real}}}{d\eta}, \tag{5.6}$$

where $\epsilon\left(\eta\right)$ denotes the efficiency as a function of pseudorapidity. In terms of the embedding, then, the efficiency as a function of pseudorapidity can be calculated by dividing the matched track $\eta$ distribution by the thrown $\eta$ distribution. In Fig. 35, I show the calculated efficiency distributions as a function of pseudorapidity for "low-$p_T$" and "high-$p_T$" tracks. For "low-$p_T$" tracks the efficiency peaks around 45% and falls rapidly at the edges of the FTPC acceptance. For "high-$p_T$" tracks, the efficiency peaks around 50%. Equation 5.6 can be used to express the average efficiency as

$$\begin{aligned}\langle\epsilon\rangle &= \frac{\int d\eta\epsilon\left(\eta\right)dN_{\text{real}}/d\eta}{\int d\eta dN_{\text{real}}/d\eta} \\ &= \frac{\int d\eta dN_{\text{meas}}/d\eta}{\int d\eta dN_{\text{real}}/d\eta}.\end{aligned} \tag{5.7}$$

Similar techniques can be used on the FMS-triggered data. In Fig. 36 I show the measured and efficiency-corrected $\eta$ distributions for "low-$p_T$" and "high-$p_T$" tracks. The average efficiency across the range of pseudorapidity (in this case $2.5 < \eta < 4.0$) is the ratio of the integrated measured yield and the integrated corrected yield. This turns out to be 34.5% for "low-$p_T$" and 38.4% for "high-$p_T$" tracks across the range

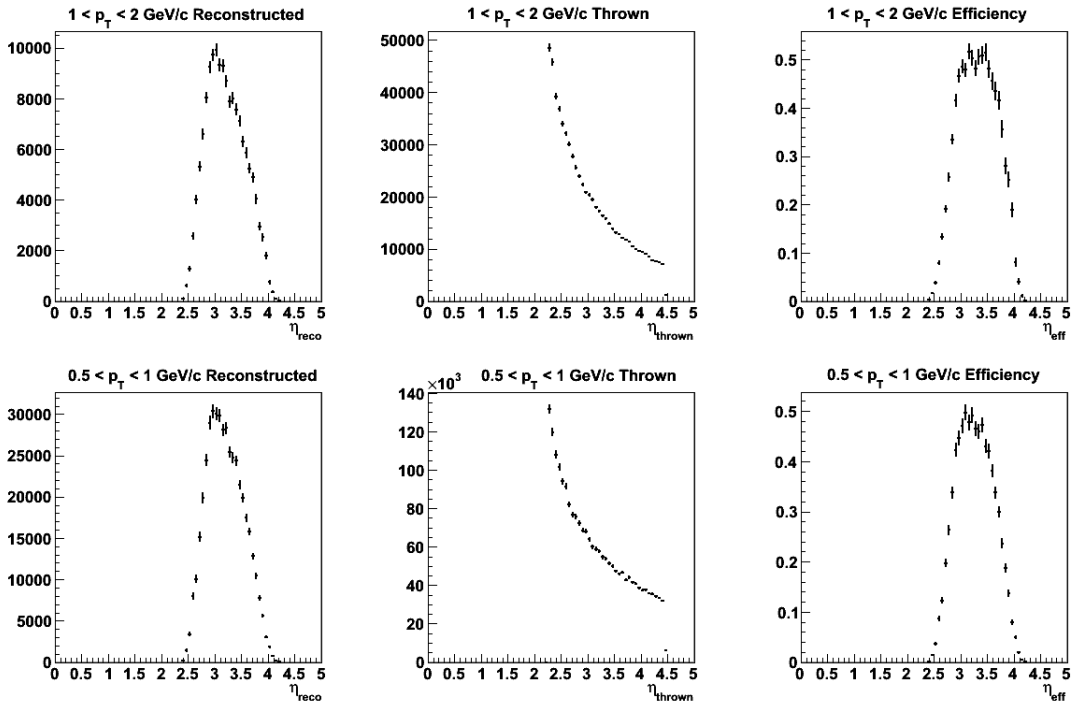


Fig. 35.: Reconstructed matched track (left), thrown track (center), and efficiency (right) $\eta$ distributions for Monte Carlo tracks embedded in FMS-triggered data and reconstructed $1.0 < p_T < 2.0$ GeV/c (top) and $0.5 < p_T < 1.0$ GeV/c (bottom).

of $2.5 < \eta < 4.0$. Below $\eta = 2.9$ the corrected distributions show a dip. This is not what one would expect for a physics distribution, particularly given the weighting used in the embedding sample. No explanation has been found, and it appears this reflects the limitations of the hit-rejection embedding technique.

## H. Corrected Track Energy

It is also important to understand the systematic shift in reconstructed track energy. First, one needs to understand how the true values relate to the reconstructed values. Using the embedding sample, it is possible to evaluate the matched-track distributions as they depend on the thrown-track distributions. In Fig. 37 I show the $p_T$-resolution,

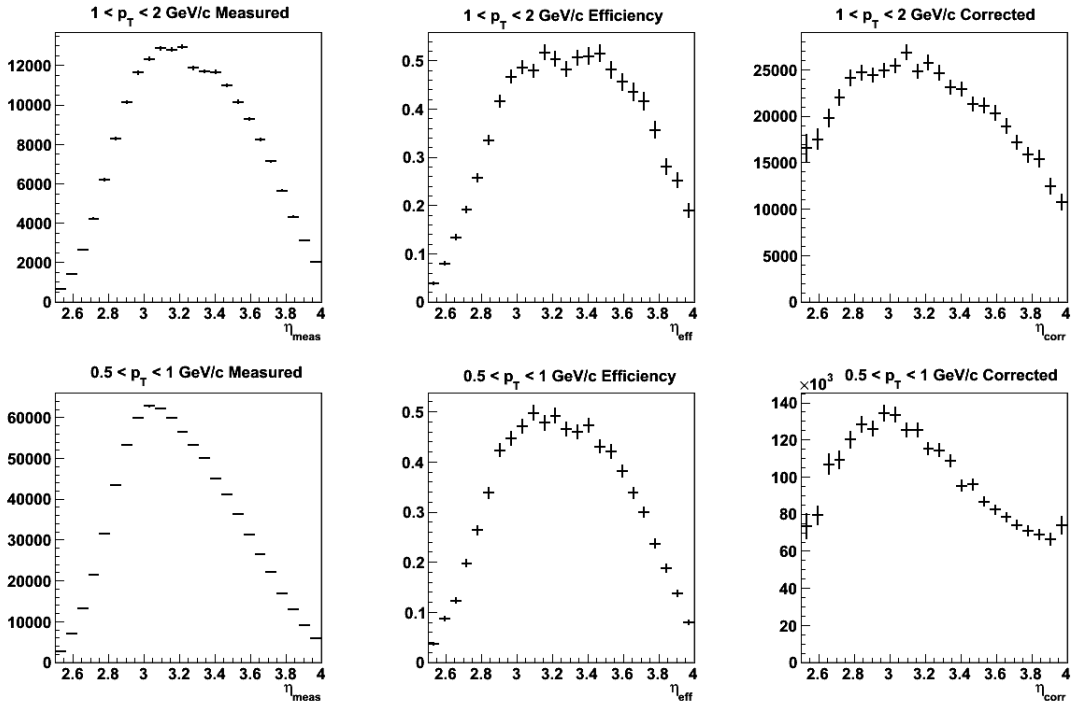


Fig. 36.: Measured (left), efficiency (center), and efficiency-corrected (right) $\eta$ distributions for FMS-triggered FTPC tracks measured with $1.0 < p_T < 2.0$ GeV/c (top) and $0.5 < p_T < 1.0$ GeV/c (bottom). Across 1.5 units of pseudorapidity, the FTPC reflects an average efficiency of 38.4% for tracks with $1.0 < p_T < 2.0$ GeV/c and 34.5% for tracks with $0.5 < p_T < 1.0$ GeV/c. Below $\eta = 2.9$, the corrected distributions show an unexpected dip reflecting the limitations of the hit-rejection embedding procedure.

$p_{T,\text{reco}} - p_{T,\text{thrown}}$, for six bins of reconstructed $p_T$. As reconstructed $p_T$ increases, the distributions become less Gaussian with a tail consistent with increasing contributions from tracks with $p_{T,\text{true}} < p_{T,\text{reco}}$. Above $p_{T,\text{reco}} = 2$ GeV/c, it appears a majority of tracks within the bin come from the tail rather than the peak. This ambiguity in true $p_T$ sheds light on the inability to separate charge sign at high $p_T$ (Fig. 34) and, again, suggests that the 2 GeV/c upper limit is a sensible cut. Because these distributions are far from Gaussian, the RMS is a better approximation of the resolution. According to the RMS, the resolution for tracks reconstructed with $0.5 < p_T < 1.0$ GeV/c is 0.16 GeV/c, while the resolution for tracks reconstructed with $1.0 < p_T < 1.5$ GeV/c is 0.28 GeV/c, and the resolution for tracks reconstructed with $1.5 < p_T < 2.0$ GeV/c is 0.47 GeV/c. Combining tracks reconstructed with $1.0 < p_T < 2.0$ GeV/c, the resolution is 0.35 GeV/c. This finite resolution tends to shift the measured $p_T$-distribution higher than reality. This is because lower $p_T$ tracks, with a relatively large cross-section, are of greater significance rolling "downhill" onto the lower cross-section of higher $p_T$ tracks than are higher $p_T$ tracks rolling "uphill" onto lower $p_T$ tracks.

In Fig. 38 I show the reconstructed $\eta$ and $p_T$ distributions for "low-$p_T$" and "high-$p_T$" tracks. In Fig. 39 I show the underlying thrown distributions for these reconstructed tracks. One can immediately see that a fraction of the yield arises from tracks thrown with momentum outside of the reconstructed $p_T$ window. The shift in $\eta$ is quite small, so I ignore it.

To quantify the relation of thrown to reconstructed $p_T$, I fit a linear regression through the reconstructed average-$p_T$ values as a function of the corresponding thrown averages. The resulting expression turns out to be

$$p_{T,\text{reco}} = 1.393 \times p_{T,\text{thrown}} - 0.276 \text{ GeV/c}. \tag{5.8}$$

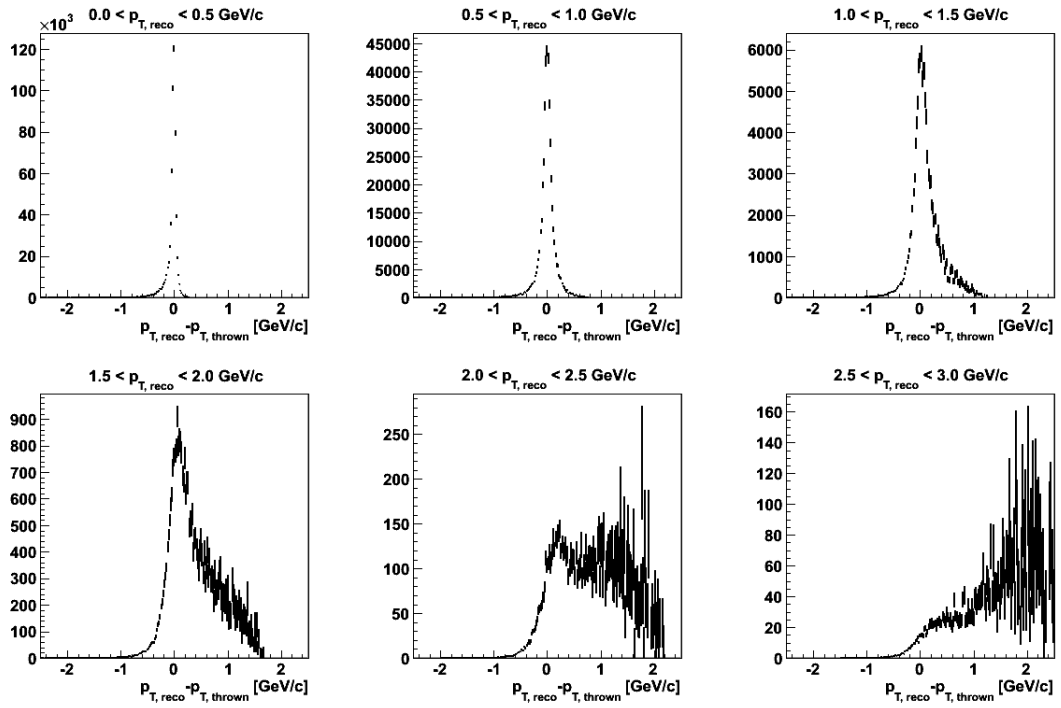


Fig. 37.: Transverse momentum resolution distributions in bins of reconstructed $p_T$. Above $p_{T,\mathrm{reco}} = 2$ GeV/c it appears most of the tracks populate the tail of the distribution. For $0.5 < p_{T,\mathrm{reco}} < 1$ GeV/c, the RMS suggests a resolution of $\approx 0.16$ GeV/c; while for $1.0 < p_{T,\mathrm{reco}} < 2$ GeV/c the RMS suggests a resolution of $\approx 0.35$ GeV/c.

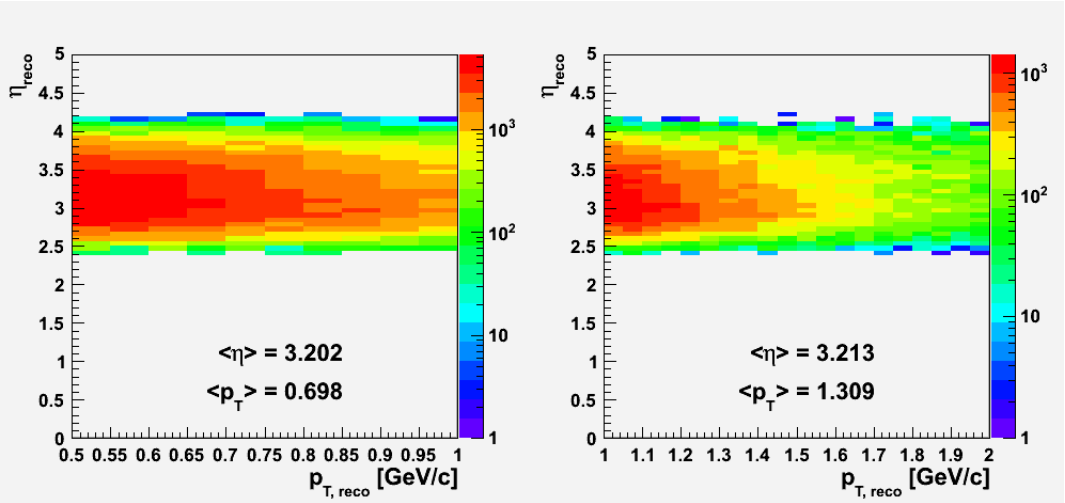


Fig. 38.: Reconstructed pseudorapidity and transverse momentum for Monte Carlo FTPC tracks embedded in FMS-triggered data and reconstructed with $0.5 < p_T < 1.0$ GeV/c (left) and $1.0 < p_T < 2.0$ GeV/c (right).

Then, if I use the average measured values from FMS-triggered data (Fig. 40), I arrive at true values of

$$\langle p_{T,\mathrm{true}}^{\mathrm{low}} \rangle = 0.68 \pm 0.04 \text{ GeV/c} \tag{5.9}$$

$$\langle p_{T,\mathrm{true}}^{\mathrm{high}} \rangle = 1.16 \pm 0.14 \text{ GeV/c}. \tag{5.10}$$

The errors are systematic in nature and calculated by taking the difference in the values when alternative weighting schemes are utilized. This can be converted into an average true energy for each bin by the familiar formula

$$E = p_T \cosh\eta. \tag{5.11}$$

By utilizing the mean $\eta$ values from the FMS-triggered data, I can approximate the true charged-particle energy for each $p_T$ bin as

$$\langle E_{\mathrm{true}}^{\mathrm{low}} \rangle = 8.48 \pm 0.5 \text{ GeV} \tag{5.12}$$

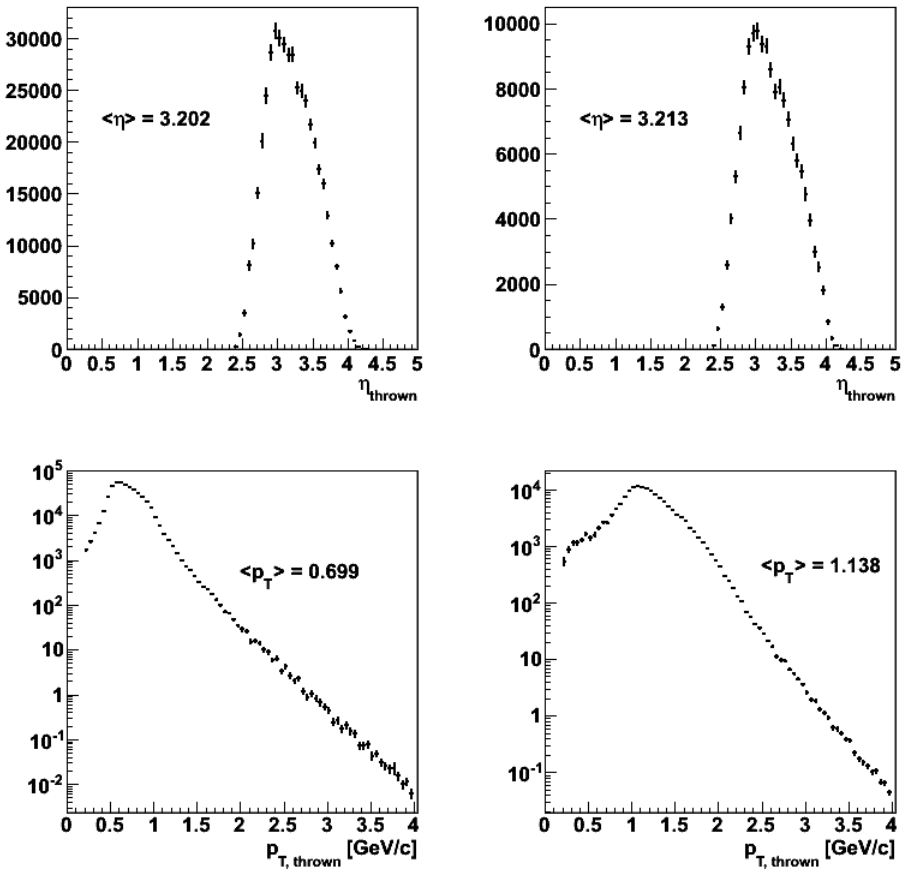


Fig. 39.: Thrown pseudorapidity and transverse momentum for Monte Carlo FTPC tracks embedded in FMS-triggered data and reconstructed with $0.5 < p_T < 1.0$ GeV/c (left) and $1.0 < p_T < 2.0$ GeV/c (right).

$$\langle E_{\text{true}}^{\text{high}} \rangle \quad = \quad 15.18 \pm 1.8 \text{ GeV}. \tag{5.13}$$

## I. Trigger Determination

I am interested in events which are triggered by a $\pi^0$ in the FMS. Thus, it is important to verify that at least one daughter photon from the pion decay could have fired the FMS high-tower trigger. To this end I have developed a procedure to define "trigger photons." A trigger photon must, first, arise from a cluster of towers containing a tower above the trigger threshold. For clusters which yield only one photon, this condition is sufficient to declare the photon a trigger photon. If the photon arises from a two-photon cluster, then, the high tower is associated with the nearer of the two photon centroids. In the rare case when the high tower is equidistant from the photons, the high tower is associated with the higher-energy photon.

## J. Neutral Pion Reconstruction

As discussed earlier, photons are required to be free of auto-correlated FTPC tracks. Additionally, it was discussed that part of the calibration process is an energy-dependent correction to photon energy. This correction is quadratic in nature and, occasionally, can result in photons "corrected" to have negative energy. Energy cuts eliminate all photons in this region, however, I implement a requirement up front to eliminate photons with $E_\gamma < 0$ GeV.

In addition, photons are required to satisfy a fiducial-volume requirement. Standard FPD and FMS analyses [9, 83] have utilized a fiducial volume of one half of a cell width from the edge of the detector. In this same spirit, photons in this analysis are required to have a centroid reconstructed at least one half of a cell width from the edge of the FMS. Photons within three quarters of a cell from a dead cell, or "hole,"

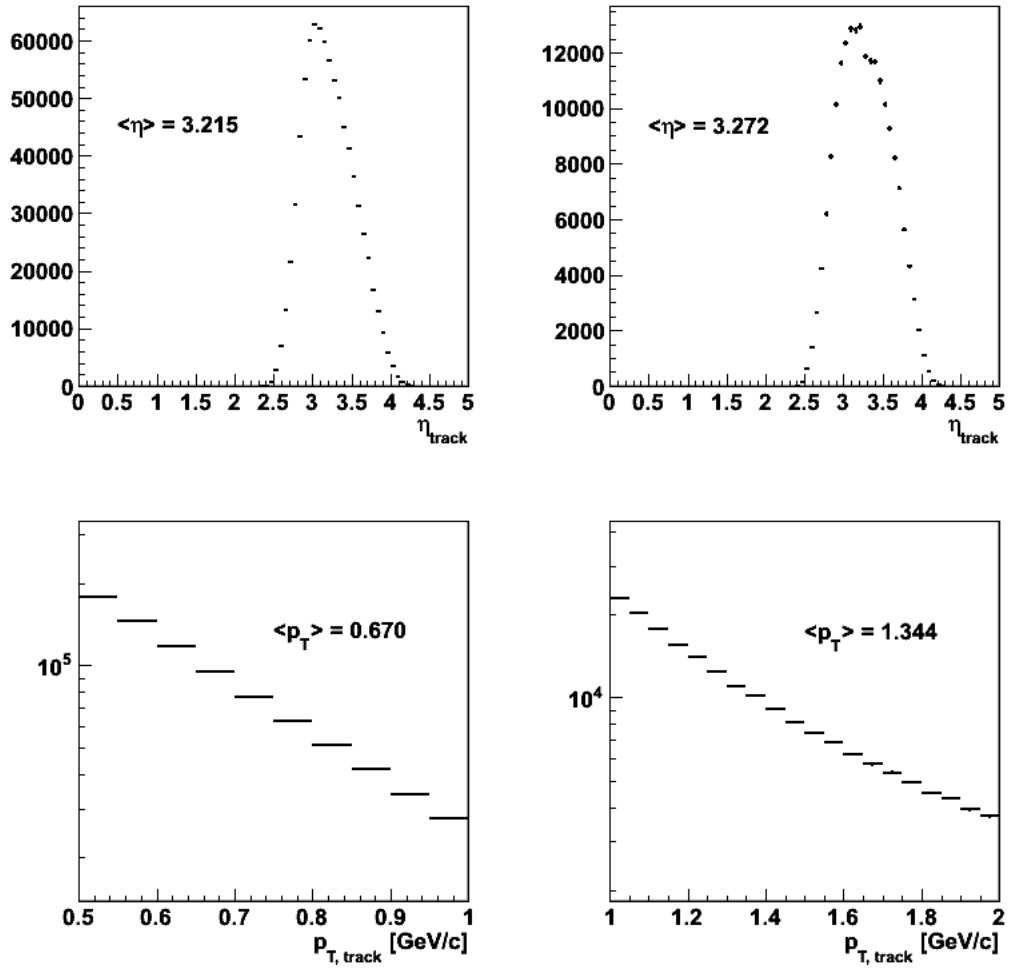


Fig. 40.: Measured pseudorapidity and transverse momentum distributions for FTPC tracks from FMS-triggered data.

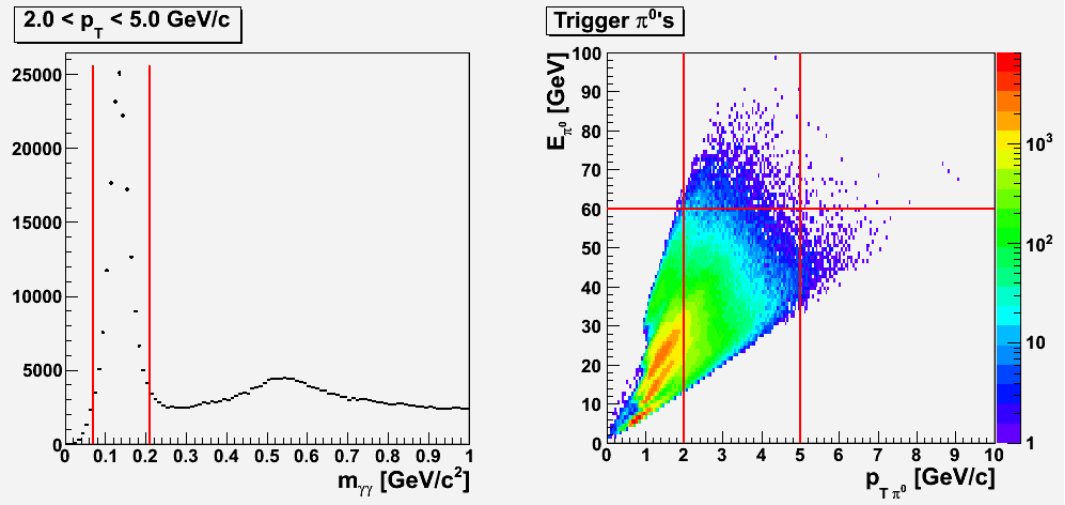


Fig. 41.: Di-photon invariant mass (left) and pion energy as a function of transverse momentum (right). In both cases, a requirement of $z_{\gamma\gamma} < 0.8$ is imposed. For the mass spectrum additional requirements of $E_{\gamma\gamma} < 60$ GeV and $2 < p_T < 5$ GeV/c are imposed. For energy as a function of transverse momentum a mass requirement of $0.07 < m_{\gamma\gamma} < 0.21$ GeV/c$^2$ is imposed. These cuts are denoted by red lines.

are also vetoed in the fiducial cut.

Pions are selected from all combinations of photon pairs where at least one photon satisfies the trigger requirement. To correct for the observed $\Delta\eta$ offset (discussed in chapter 4), the photons are shifted by $\delta\eta = -0.0256$. Because of the limitations of the two-photon separation capability of the cluster-finding algorithm, an upper-limit of $E_{\gamma\gamma} < 60$ GeV is enforced. One consequence of the high-tower trigger is that the data are biased toward asymmetric pion decay. Achieving sufficient ADC in a single tower favors an energetic photon depositing all of its energy in the center of a single tower. The pion cross section falls as a function of energy and, thus, minimizing the pion energy biases the decay in favor of one photon carrying most of the energy. This situation is only exacerbated by the extreme nature of the gain non-uniformity. To combat this trigger bias, an upper limit of 0.8 on the energy-sharing, $z_{\gamma\gamma}$, is enforced. The energy sharing is defined as

$$z_{\gamma\gamma} = \frac{|E_1 - E_2|}{E_1 + E_2}, \tag{5.14}$$

where $E_{\mathrm{n}}$ denotes the energy of the $\mathrm{n}^{\mathrm{th}}$ photon. A mass requirement of $0.07 < m_{\gamma\gamma} < 0.21$ GeV/$\mathrm{c}^2$ is, then, enforced to select $\pi^0$'s. In the event that more than one pion satisfies the $z_{\gamma\gamma}$, $E_{\gamma\gamma}$, and $m_{\gamma\gamma}$ requirements, the pion with highest $p_T$ is selected. Finally, pions are analyzed within a window of $2 < p_T < 5$ GeV/c (Fig. 41).

## K. Corrected Pion Energy

Just as it is useful to evaluate the corrected values for track energy, it is also useful to examine the corrected values for pion energy. Misidentification of the energy is due to limitations in energy resolution and the effects of lower energy pions (with greater cross section) reconstructing with higher energy, leading to a stiffer measured energy

spectrum than is really there.

In understanding the shift in pion energy, toy models can be powerful tools. First, the FPD neutral pion cross section for $\langle\eta\rangle = 3.3$ [12] is fit with a simple exponential function of the form $\sigma \propto \exp(-\alpha E)$. To evaluate how this is distorted by finite resolution, the fit is convoluted with a response function. One such example is a gaussian function with width based on the detector resolution. This resolution can be estimated to be $\sim 8\%$ [84]. Similarly, the true energy as a function of the measured energy can be understood by convoluting the cross section with the response function times the true energy and dividing by the measured cross section. Then, the average energies can be calculated by the familiar integral form

$$\langle E_{\rm meas}\rangle = \frac{\int_{E_{\rm min}}^{E_{\rm max}} dE_{\rm meas} E_{\rm meas}\sigma\left(E_{\rm meas}\right)}{\int_{E_{\rm min}}^{E_{\rm max}} dE_{\rm meas}\sigma\left(E_{\rm meas}\right)} \tag{5.15}$$

$$\langle E_{\rm true}\rangle = \frac{\int_{E_{\rm min}}^{E_{\rm max}} dE_{\rm meas} E_{\rm true}\left(E_{\rm meas}\right)\sigma\left(E_{\rm meas}\right)}{\int_{E_{\rm min}}^{E_{\rm max}} dE_{\rm meas}\sigma\left(E_{\rm meas}\right)}. \tag{5.16}$$

After tuning parameters for the cross section slope, minimum energy threshold, and energy resolution, the shift in pion energy can be reported as

$$\frac{E_{\rm true}}{E_{\rm meas}} = 0.95 \pm 0.05. \tag{5.17}$$

The uncertainty is systematic in nature and derived by taking the difference between the shifts for various extremes of cross-section slopes, energy thresholds, and energy resolutions. Thus, for a nominal pion energy of $E_{\rm meas} = 31.0$ GeV, the true energy can be reported as $E_{\rm true} = 29.5 \pm 1.6$ GeV.

# CHAPTER VI

# TWO-PARTICLE CORRELATIONS

Having studied the neutral pions and charged particles in their own right, it is now possible to evaluate the correlation of the neutral pions and the charged-particles. It is in these correlations where new information on dynamical contributions to asymmetries is accessible.

## A. Acceptance Correction

As discussed in chapters 4 and 5, the FMS trigger suffers from considerable acceptance inefficiency due to gain non-uniformity, while electronics failures in the FTPC introduce their own acceptance inefficiencies into the associations. While a correlation signal may forgive acceptance transgressions for one participant, the convolution of acceptance issues in both participants introduces significant distortions. Correction of acceptance distortions constitutes one of the major tasks of this analysis.

One way to understand the effect of acceptance inefficiencies is to utilize a mixed-event analysis. Two-particle correlations from the same event should contain a physics signal on top of an underlying structure due to the acceptance inefficiency. Two-particle correlations with each participant from different events should be void of physics, revealing the underlying structure based solely on acceptance. Thus, dividing the "same-event" correlation distribution by the mixed-event distribution should remove the acceptance structure, revealing an acceptance-corrected correlation signal.

Mixed-event analyses are challenging from a computing standpoint, since the true procedure involves calculations, in this case $(\eta_\pi - \eta_{\text{track}}, \phi_\pi - \phi_{\text{track}})$, while looping over every track in all events for every pion from every event (save those from the same event). The computing time for such a procedure is quite large, rendering the

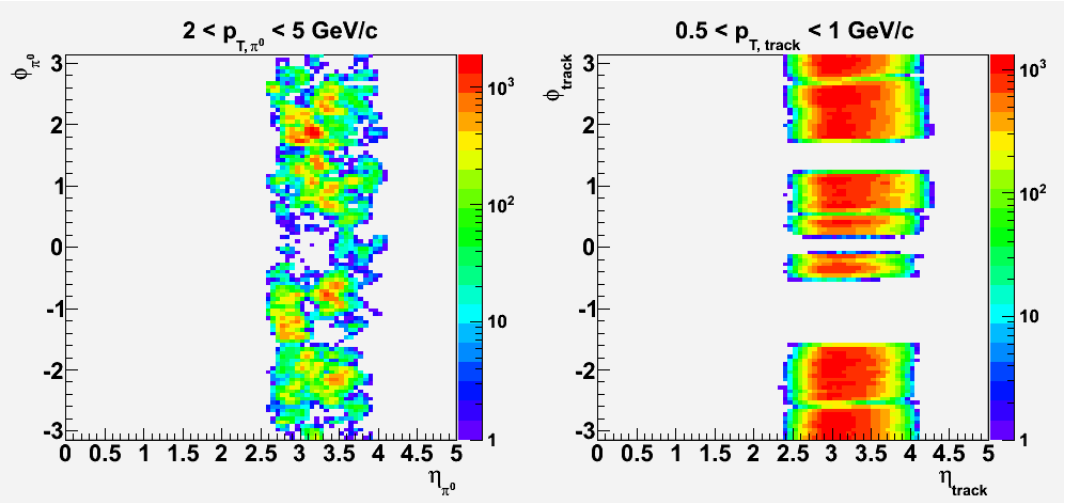


Fig. 42.: $\eta$-$\phi$ scatter plots for (left) neutral pions and (right) charged-particles. Associated charged particles shown satisfy $0.5 < p_T < 1$ GeV/c, while the pions satisfy $2 < p_T < 5$ GeV/c.

true procedure impractical. In light of this, approximations are necessary. One option is to mix events with like properties. Such a method will be discussed in a forthcoming section. Additionally, one can work from histograms. The benefit of working from histograms is a major reduction in computing time, in this case, down to a matter of minutes. The sacrifice is a loss in granularity. For the purposes of this analysis the gain in computing efficiency outweighs the loss in granularity. First, a pass is made over the data, binning $\eta$ and $\phi$ for every track and every $\pi^0$ passing the cuts and $\Delta\eta = \eta_\pi - \eta_{\text{track}}$ and $\Delta\phi = \phi_\pi - \phi_{\text{track}}$ for each coincidence in an event. To ensure that the granularity is treated consistently, each correlation entry is computed with the same granularity as the forthcoming histogram procedure. The single-particle distributions in hand (Fig. 42), I loop over every track $(\eta, \phi)$-bin for each pion bin. For each iteration, $\Delta\eta$ and $\Delta\phi$ are calculated from the histogram bin centers. These values are binned in a new correlation histogram with a weight of the product of

the entries of the two single-particle bins. The resulting new correlation histogram contains not only the mixed events but also "same events." However, the "same events" can be removed by subtracting out the raw correlation histogram produced in the data pass from the new histogram. This results in a true mixed event distribution (Fig. 43) with somewhat limited granularity. One remaining issue is the handling of auto-correlations in the mixed events. Auto-correlations in the raw physics have been discussed in chapter 4. One possibility is simply to zero out bins surrounding $(0,0)$ in $\Delta\eta$-$\Delta\phi$-space. As long as the bin zeroing is a more liberal cut than the event-level veto, the bin zero can be a consistent veto for both raw physics and mixed events. To this end, I implement a veto excluding bins from $-3\pi/100 < \Delta\phi < 3\pi/100$ and from $-3/32 < \Delta\eta < 3/32$.

Figure 43 shows an example of dividing out the relative acceptance distortions from raw physics correlations. It is clear that prior to correction, the acceptance distortions (see Fig. 42), completely wash out the away-side signal. After correction, there is clear evidence of an away-side peak. For a true physics measurement, scaling for absolute efficiency is necessary. By applying the corrections discussed in chapter 5, the acceptance-corrected correlations can be scaled for the FTPC efficiency across the range of $2.5 < \eta < 4.0$. The results of this are shown in Fig. 44 for both ranges of associated transverse momentum. The distributions have been fit with a series of Gaussians plus a constant background. The function is of the form

$$\begin{aligned}\frac{dN}{d\Delta\phi} &= C_{\mathrm{B.G.}} + C_{\mathrm{N.S.}}\left[\exp\left(-\frac{1}{2}\frac{\Delta\phi^2}{\sigma^2_{\mathrm{N.S.}}}\right) + \exp\left(-\frac{1}{2}\frac{(\Delta\phi-2\pi)^2}{\sigma^2_{\mathrm{N.S.}}}\right)\right] \\ &\quad + C_{\mathrm{A.S.}}\left[\exp\left(-\frac{1}{2}\frac{(\Delta\phi-\pi)^2}{\sigma^2_{\mathrm{A.S.}}}\right) + \exp\left(-\frac{1}{2}\frac{(\Delta\phi+\pi)^2}{\sigma^2_{\mathrm{A.S.}}}\right)\right], \qquad (6.1)\end{aligned}$$

where B.G. denotes the continuum background, N.S. denotes the "near-side peak," centered at $\Delta\phi = 0$, and A.S. denotes the "away-side peak," centered at $\Delta\phi = \pi$.

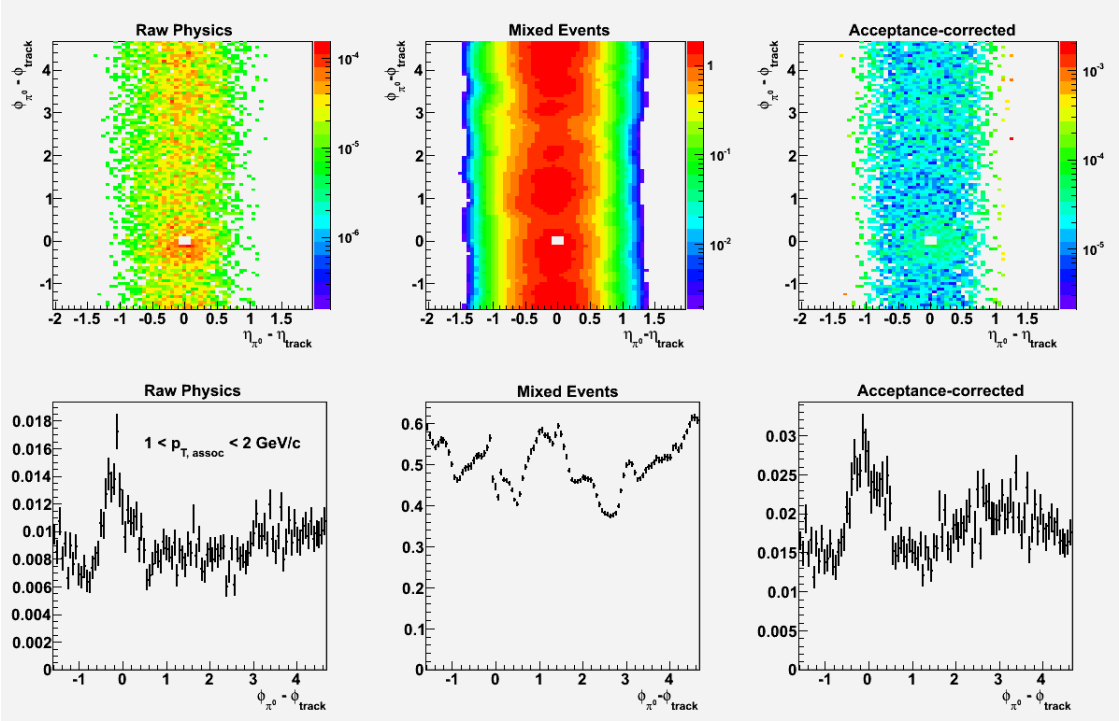


Fig. 43.: Correlation distributions for (left) raw physics (center) mixed events uncorrected for absolute efficiency and (right) acceptance corrected physics not scaled for absolute efficiency. Associated charged particles satisfy $1.0 < p_T < 2.0$ GeV/c. Bins near $(\Delta\eta, \Delta\phi) = (0, 0)$ in the 2-D distributions (top row) are removed to veto residual auto-correlations in a consistent manner between raw physics and mixed events.

Table III.: Parameters for double-Gaussian plus constant (Eq. 6.1) fit to azimuthal $\pi^0$-charged particle correlations (Fig. 44).

| Parameter | $1 < p_{T,\text{assoc}} < 2$ GeV/c | $0.5 < p_{T,\text{assoc}} < 1$ GeV/c |
|---|---|---|
| Continuum | $0.0077 \pm 0.0070$ | $0.0671 \pm 0.0048$ |
| N.S. Amplitude | $0.0132 \pm 0.0010$ | $0.0246 \pm 0.0042$ |
| N.S. Width | $0.385 \pm 0.030$ | $0.516 \pm 0.075$ |
| A.S. Amplitude | $0.0100 \pm 0.0070$ | $0.0187 \pm 0.0044$ |
| A.S. Width | $1.60 \pm 0.63$ | $0.94 \pm 0.24$ |

Because the widths of the away-side peaks are rather large, I have included the additional Gaussian functions, centered at $\Delta\phi = 2\pi$ and $\Delta\phi = -\pi$, to account for the "wrap-around" of the signal peaks. Results of the fits are summarized in Table III. Associations with $1.0 < p_T < 2.0$ GeV/c suffer from statistics limitations, which lead to large uncertainties for the away-side peak parameters and strong correlations between the continuum and away-side peak parameters. Associations with $0.5 < p_T < 1.0$ GeV/c tend to have a much larger continuum background than the higher-$p_T$ counterparts.

## B. Pile-up and Rate Dependence

Since the FTPC is a slow read-out detector, one large source of background is pile-up tracks. A cut on the track distance of closest approach to the primary vertex is used to limit pile-up (Fig. 29). Quantifying the remaining pile-up is an important step in understanding the components of the yield which factor into asymmetry corrections.

In principle, physics should be independent of the collision rate. Pile-up on the

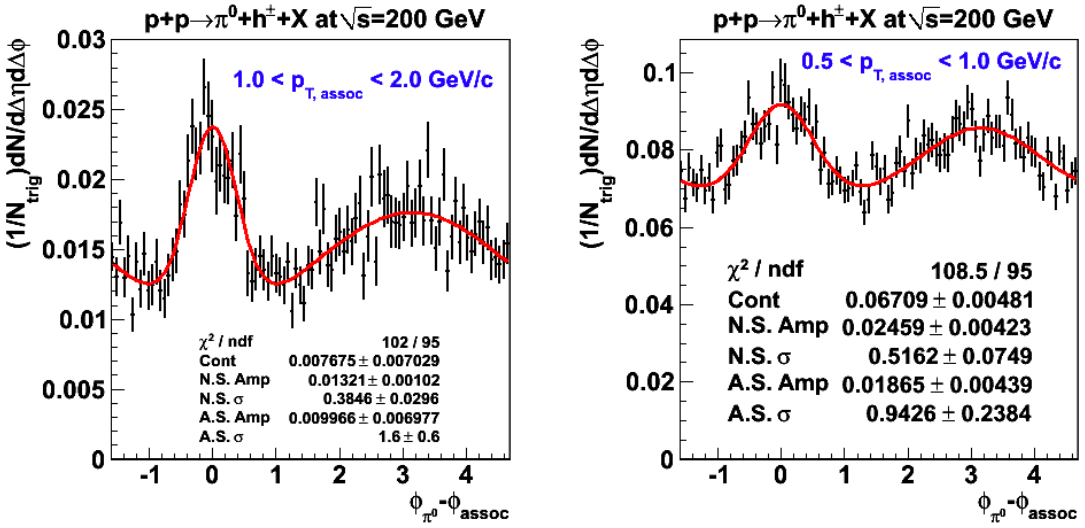


(a) (b)

Fig. 44.: Efficiency and acceptance-corrected two-particle azimuthal correlations from $p+p$ collisions at 200 GeV. Correlations are between $\pi^0$'s with $2 < p_T < 5$ GeV/c and charged particles with (a) $1.0 < p_T < 2.0$ GeV/c and (b) $0.5 < p_T < 1.0$ GeV/c. Distributions have been fit with a double-Gaussian plus constant background function (Eq. 6.1). The near-side centroid is forced to $\Delta\phi = 0$ and the away-side centroid is forced to $\Delta\phi = \pi$. Results of the fit are summarized in Table III.

other hand, is strongly coupled to the rate of collisions. One way to model the yield is to consider a linear dependence on collision rate for pile-up. To quantify the pile-up fraction of the yield, I divide the $\Delta\phi$ correlations into three bins of BBC coincidence rate, $\nu$. After correcting each bin for acceptance, I fit the resulting distribution with a function of the form

$$\begin{aligned}\frac{dN}{d\Delta\phi}(\nu) &= C_{\text{B.G.Phys.}} + C_{\text{rate}}\nu \\ &\quad + C_{\text{N.S.}}\left[\exp\left(-\frac{1}{2}\frac{\Delta\phi^2}{\sigma^2_{\text{N.S.}}}\right) + \exp\left(-\frac{1}{2}\frac{(\Delta\phi-2\pi)^2}{\sigma^2_{\text{N.S.}}}\right)\right] \\ &\quad + C_{\text{A.S.}}\left[\exp\left(-\frac{1}{2}\frac{(\Delta\phi-\pi)^2}{\sigma^2_{\text{A.S.}}}\right) + \exp\left(-\frac{1}{2}\frac{(\Delta\phi+\pi)^2}{\sigma^2_{\text{A.S.}}}\right)\right], \qquad (6.2)\end{aligned}$$

where B.G. Phys. denotes the physical, underlying-event component of the background. Figure 45 shows the results of the fits for each sample of associated transverse momentum with the parameter values summarized in Table IV. The lower of the two associated $p_T$-bins shows a larger rate dependence. Applying the rate-dependent fit to the full correlation distributions (Fig. 46) the rate-dependent component, $C_{\text{rate}}\nu$, constitutes $0.23 \pm 0.13$ of the total background, $C_{\text{B.G.Phys.}} + C_{\text{rate}}\nu$, for tracks with $1 < p_T < 2$ GeV/c and $0.201 \pm 0.017$ of the total background for tracks with $0.5 < p_T < 1$ GeV/c. The large error for the higher $p_T$ correlations is due to the effect of limited statistics on the azimuthal correlation fit, specifically, the large uncertainties related to the wide away-side peak.

A two-dimensional fit to the distribution proves problematic due to low statistics and large bin fluctuations. Thus, I turn to a reasonably intuitive model for the two-dimensional correlations. I assume a constant for the continuum background. For the near-side peak, I assume a two-dimensional Gaussian centered on $(0, 0)$ in $\eta$-$\phi$ space with a single width for both dimensions. For the away-side peak, I assume the Gaussian for $\Delta\phi$ constant across the range of $\Delta\eta$. This assumption for the away-

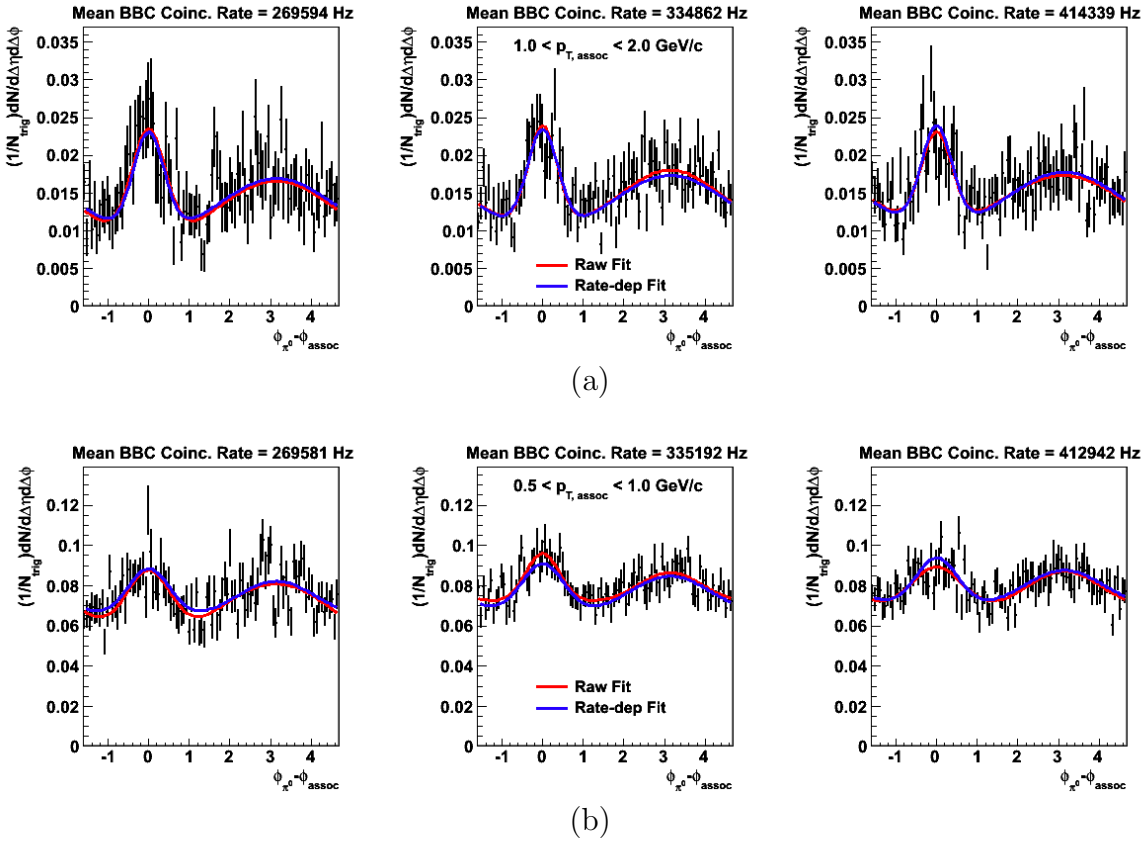


Fig. 45.: $\Delta\phi$ correlation for three bins of BBC coincidence rate for associated particles with (a) $1 < p_T < 2$ GeV/c and (b) $0.5 < p_T < 1$ GeV/c. Distributions are shown with two fits: shown in red is a raw fit to each panel with a double-Gaussian plus constant background (Eq. 6.1), and shown in blue is a double-Gaussian plus a background linear in BBC coincidence rate (Eq. 6.2). The results of the rate-dependent fit are summarized in Table IV.

Table IV.: Parameters for double-Gaussian plus rate-dependent continuum fit (Eq. 6.2) to azimuthal $\pi^0$-charged particle correlations (Fig. 45).

| Parameter | $1 < p_{T,\text{assoc}} < 2$ GeV/c | $0.5 < p_{T,\text{assoc}} < 1$ GeV/c |
|---|---|---|
| Physics Continuum | $0.0067 \pm 0.0048$ | $0.0530 \pm 0.0058$ |
| Rate Dependence | $0.0058 \pm 0.0029$ MHz$^{-1}$ | $0.0382 \pm 0.0071$ MHz$^{-1}$ |
| N.S. Amplitude | $0.0132 \pm 0.0012$ | $0.0249 \pm 0.0045$ |
| N.S. Width | $0.380 \pm 0.034$ | $0.518 \pm 0.074$ |
| A.S. Amplitude | $0.0087 \pm 0.0046$ | $0.0188 \pm 0.0048$ |
| A.S. Width | $1.43 \pm 0.54$ | $0.97 \pm 0.25$ |

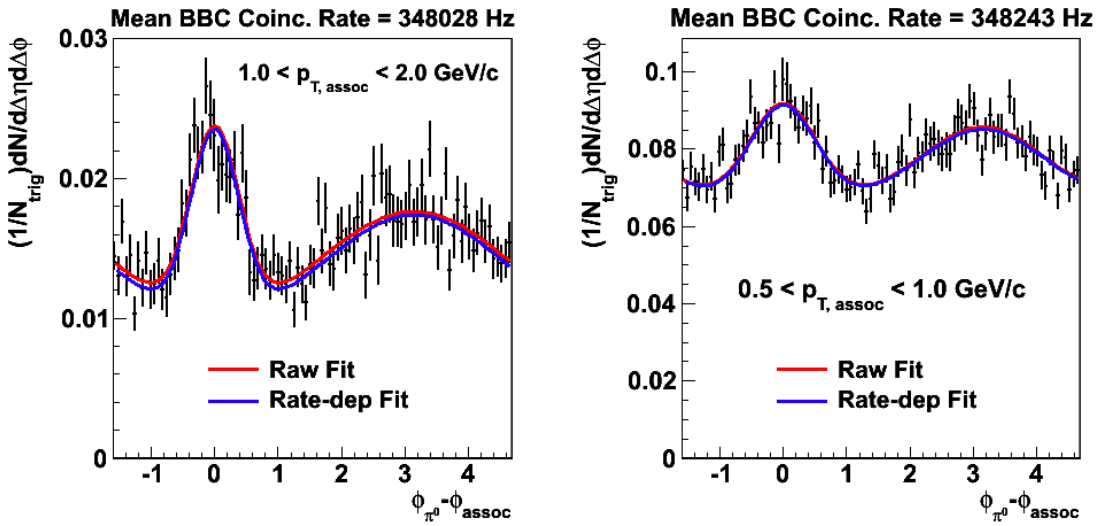


(a) (b)

Fig. 46.: $\Delta\phi$ correlation integrated over BBC coincidence rate for associated particles with (a) $1 < p_T < 2$ GeV/c and (b) $0.5 < p_T < 1$ GeV/c. Distributions are shown with two fits: shown in red is the raw fit (Eq. 6.1) as shown in Fig. 44, and shown in blue is the rate-dependent fit (Eq. 6.2) as summarized in Table IV.

side is a crude approximation. Ultimately, however, it is the near-side peak which is of most interest. Approximations for the away-side peak should translate into negligible ambiguities in the near-side peak given the available statistical precision. To determine the parameters, I integrate the two-dimensional function across a sensible range of $\Delta\eta$ and tune the two-dimensional parameters to equal the parameters from the one-dimensional fits (Fig. 46). There is some ambiguity in the appropriate range of $\Delta\eta$, so I have performed the integration over two ranges. The range of $-1 < \Delta\eta < 1$ is taken as the baseline measurement, and the range of $-0.7 < \Delta\eta < 0.7$ will factor into systematic uncertainties. The results are summarized in Table V.

## C. Near-side Correlations

Ultimately, I am interested in two-particle correlations from the same jet. Thus, prior to investigating polarized effects, it is useful to examine the unpolarized near-side correlations. "Near-side," here, means satisfaction of a restriction on the two-particle pair radius,

$$\Delta R = \sqrt{\Delta\eta^2 + \Delta\phi^2}. \tag{6.3}$$

Changing the upper-limit on $\Delta R$ will change the various contributions–signal, pile-up, underlying-event, etc.–to the over-all near-side yield. Given the statistics limitations of this analysis, it is important to optimize the amount of raw yield for the amount of background dilution under the signal. In this analysis, I focus on three upper-limits of $\Delta R$: $\pi/3$, 0.7, and 0.5. The components of the yield can be estimated by integrating the two-dimensional correlation fit, summarized in Table V. The yield fractions are, then, the ratios of the various components to the total yield, after accounting for the auto-correlation cut. The various yield fractions are summarized in Table VI.

Finite momentum resolution in the FMS and FTPC leads to the need to apply

Table V.: Parameters for two-dimensional double-Gaussian plus constant fit to azimuthal $\pi^0$-charged particle correlations. The parameters are derived from integration of the two-dimensional function across the range of $\Delta\eta$ and comparing to the parameters from the fit to the azimuthal distribution (Fig. 46).

| | $-1 < \Delta\eta < 1$ | |
|---|---|---|
| Parameter | $1 < p_{T,\text{assoc}} < 2$ GeV/c | $0.5 < p_{T,\text{assoc}} < 1$ GeV/c |
| Continuum | $0.00437 \pm 0.00246$ | $0.0332 \pm 0.0031$ |
| N.S. Amplitude | $0.0140 \pm 0.0018$ | $0.0202 \pm 0.0042$ |
| N.S. Width | $0.380 \pm 0.034$ | $0.518 \pm 0.074$ |
| A.S. Amplitude | $0.00433 \pm 0.00229$ | $0.00942 \pm 0.00240$ |
| A.S. Width | $1.43 \pm 0.54$ | $0.973 \pm 0.254$ |

| | $-0.7 < \Delta\eta < 0.7$ | |
|---|---|---|
| Parameter | $1 < p_{T,\text{assoc}} < 2$ GeV/c | $0.5 < p_{T,\text{assoc}} < 1$ GeV/c |
| Continuum | $0.00625 \pm 0.00352$ | $0.0474 \pm 0.0045$ |
| N.S. Amplitude | $0.0149 \pm 0.0017$ | $0.0232 \pm 0.0045$ |
| N.S. Width | $0.380 \pm 0.034$ | $0.518 \pm 0.074$ |
| A.S. Amplitude | $0.00619 \pm 0.00327$ | $0.0135 \pm 0.0034$ |
| A.S. Width | $1.43 \pm 0.54$ | $0.973 \pm 0.254$ |

Table VI.: Yield fractions of the near-side peak, defined by upper-limits on the pair radius, $\Delta R$. Yields are determined by integrating the two-dimensional correlation fit (Table V) tuned to the one-dimensional correlation fit (Fig. 46) by assuming an active range of $-1 < \Delta\eta < 1$. The integrated yields exclude the auto-correlation component falling within $-3/32 < \eta < 3/32$ and $-3\pi/100 < \phi < 3\pi/100$.

| $1 < p_{T,\text{assoc}} < 2$ GeV/c | | | |
|---|---|---|---|
| Component | $\Delta R < \pi/3$ | $\Delta R < 0.7$ | $\Delta R < 0.5$ |
| Signal Fraction | $0.396 \pm 0.158$ | $0.557 \pm 0.174$ | $0.638 \pm 0.168$ |
| Underlying-event Fraction | $0.381 \pm 0.301$ | $0.285 \pm 0.217$ | $0.234 \pm 0.176$ |
| Pile-up Fraction | $0.114 \pm 0.068$ | $0.085 \pm 0.048$ | $0.070 \pm 0.038$ |
| Away-side Fraction | $0.110 \pm 0.175$ | $0.073 \pm 0.128$ | $0.057 \pm 0.104$ |

| $0.5 < p_{T,\text{assoc}} < 1$ GeV/c | | | |
|---|---|---|---|
| Component | $\Delta R < \pi/3$ | $\Delta R < 0.7$ | $\Delta R < 0.5$ |
| Signal Fraction | $0.203 \pm 0.062$ | $0.282 \pm 0.072$ | $0.324 \pm 0.077$ |
| Underlying-event Fraction | $0.632 \pm 0.092$ | $0.571 \pm 0.082$ | $0.538 \pm 0.078$ |
| Pile-up Fraction | $0.159 \pm 0.033$ | $0.143 \pm 0.030$ | $0.135 \pm 0.028$ |
| Away-side Fraction | $0.007 \pm 0.012$ | $0.0037 \pm 0.0083$ | $0.0028 \pm 0.0068$ |

the corrections discussed in chapters 4 and 5 to evaluate the kinematics of the near-side correlations. Taking the example of $\Delta R < \pi/3$, in the presence of a $1 < p_T < 2$ GeV/c association, $\pi^0$'s show an average uncorrected energy of 30.53 GeV; and in the presence of a $0.5 < p_T < 1$ GeV/c association, $\pi^0$'s show an average uncorrected energy of 30.79 GeV. Utilizing Eqn. 5.17, I can cite corrected pion energies of

$$\langle E_{\pi^0,\mathrm{low}}^{\Delta R<\pi/3} \rangle = 29.3 \pm 1.5 \text{ GeV} \tag{6.4}$$

$$\langle E_{\pi^0,\mathrm{high}}^{\Delta R<\pi/3} \rangle = 29.0 \pm 1.5 \text{ GeV}, \tag{6.5}$$

where "low" denotes $0.5 < p_T < 1$ GeV/c associations and "high" denotes $1 < p_T < 2$ GeV/c associations. Combining this information with Eqns. 5.12 and 5.13, I can quote a corrected average pair-wise energy of

$$\langle E_{\mathrm{pair,low}}^{\Delta R<\pi/3} \rangle = 37.7 \pm 1.6 \text{ GeV} \tag{6.6}$$

$$\langle E_{\mathrm{pair,high}}^{\Delta R<\pi/3} \rangle = 44.2 \pm 2.4 \text{ GeV}. \tag{6.7}$$

Table VII summarizes the corrected average pair-wise energy for near-side correlations defined by all three upper-limits on pair radius. The variation with $\Delta R$ is small compared to the correlated systematic uncertainty associated with the conversion from measured to true momenta. Thus, I can quote a common average $x_F$ for all upper-limits on pair radius

$$\langle x_{F,\mathrm{low}} \rangle = 0.38 \pm 0.02 \tag{6.8}$$

$$\langle x_{F,\mathrm{high}} \rangle = 0.44 \pm 0.02. \tag{6.9}$$

Figures 47 and 48 show the invariant mass of the two-particle system for the three upper limits on $\Delta R$. In all but the tightest restriction on the low-$p_T$ correlations, there is some evidence of a $\rho$ peak on a falling continuum. The absence of a $\rho$ signal

Table VII.: Corrected average pair-wise energy for near-side correlations defined by upper-limits on pair radius, $\Delta R_{\rm max}$.

| $\Delta R_{\rm max}$ | $1 < p_{T,\rm assoc} < 2$ GeV/c | $0.5 < p_{T,\rm assoc} < 1$ GeV/c |
|---|---|---|
| $\pi/3$ | $44.2 \pm 2.4$ GeV | $37.7 \pm 1.6$ GeV |
| 0.7 | $44.4 \pm 2.4$ GeV | $37.9 \pm 1.6$ GeV |
| 0.5 | $44.3 \pm 2.4$ GeV | $37.8 \pm 1.6$ GeV |

in this particular bin is consistent with the expectation for maximal invariant mass based on kinematic and geometric limits. At $\Delta R = 0.5$, $p_{T,\pi^0} = 5$ GeV/c, and $p_{T,\rm assoc} = 1$ GeV/c, $m_{\rm pair}^{\rm max} = 0.80$ GeV/c$^2$. The mass distributions suggest the events provide sensitivity to a "jet-like" sample, rather than an inclusive meson sample, for instance.

As discussed in chapter 1, spin effects due to IFF's depend on two angles: $\phi_S$, which defines the azimuthal angle of the spin-polarization relative to the sum of the two particle momenta, and $\phi_R$, which defines the azimuthal angle of the difference of the two particle momenta about the sum. Thus, it is useful to analyze the unpolarized $\phi_R$ distribution prior to moving on to spin effects. For each event, I correlate the trigger pion with each track in the event satisfying either $0.5 < p_T < 1.0$ GeV/c or $1.0 < p_T < 2.0$ GeV/c. Provided the pair radius limit and the auto-correlation cut are satisfied, I calculate two vectors:

$$\vec{P} = \vec{p}_{\pi^0} + \vec{p}_{\rm track} \tag{6.10}$$

$$\vec{R} = \vec{p}_{\pi^0} - \vec{p}_{\rm track}, \tag{6.11}$$

where $\vec{p}$ denotes the three-momentum. I, then, rotate both $\vec{P}$ and $\vec{R}$ into the so-called

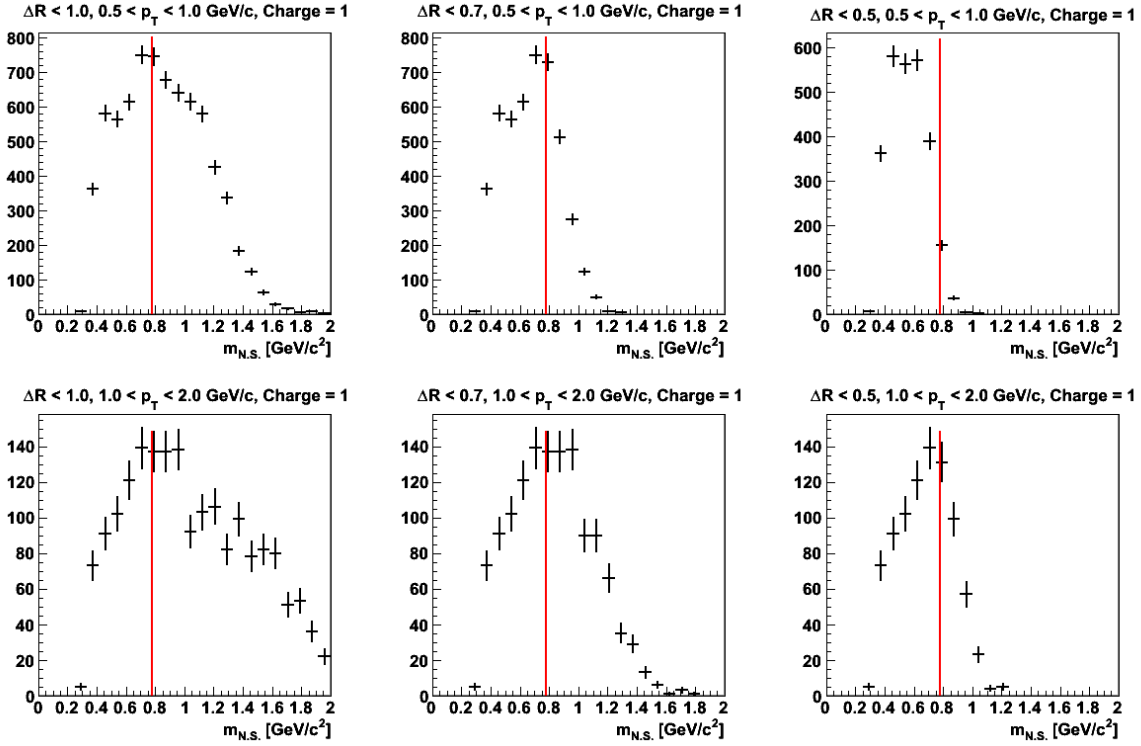


Fig. 47.: Invariant pair mass for three upper-limits on pair radius for positively-charged associated particles. The top row shows mass for associated particles with $0.5 < p_T < 1$ GeV/c while the lower row shows mass for associated particles with $1 < p_T < 2$ GeV/c. The red lines denote the mass for the $\rho$ meson. Note that for lower $p_T$ correlations with $\Delta R < 0.5$, the kinematics severely restrict the ability to reach the $\rho$ mass.

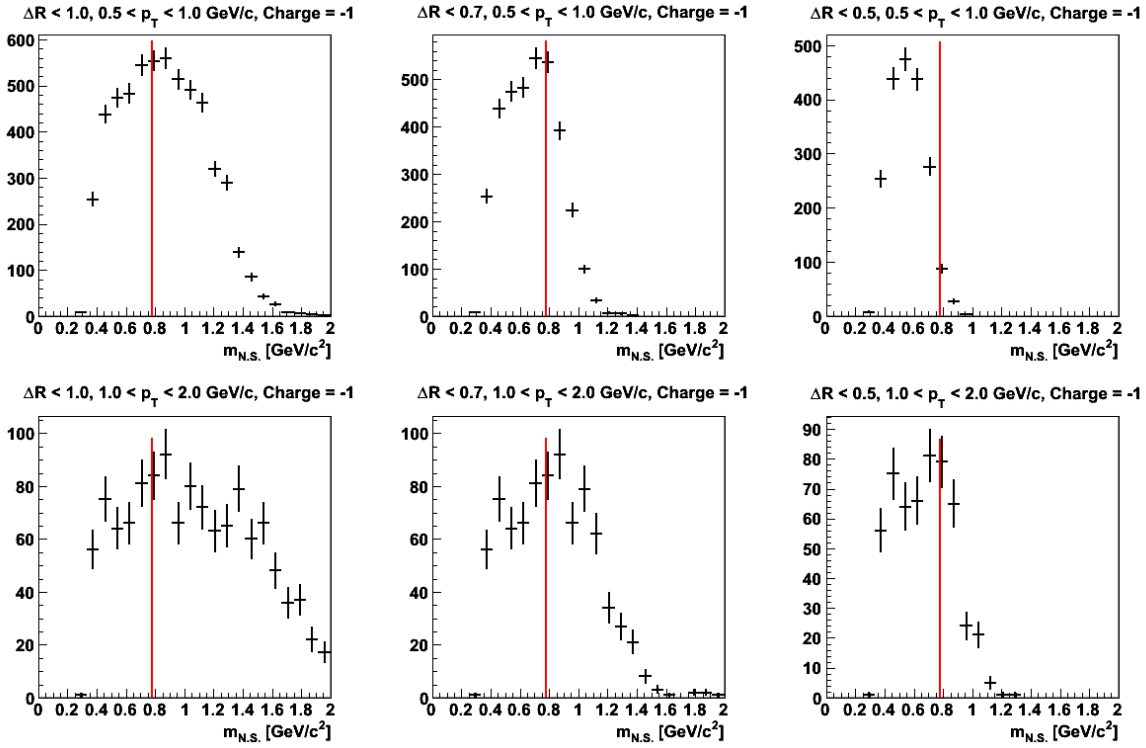


Fig. 48.: Invariant pair mass for three upper-limits on pair radius for negatively-charged associated particles. The top row shows mass for associated particles with $0.5 < p_T < 1$ GeV/c while the lower row shows mass for associated particles with $1 < p_T < 2$ GeV/c. The red lines denote the mass for the $\rho$ meson. Note that for lower $p_T$ correlations with $\Delta R < 0.5$, the kinematics severely restrict the ability to reach the $\rho$ mass.

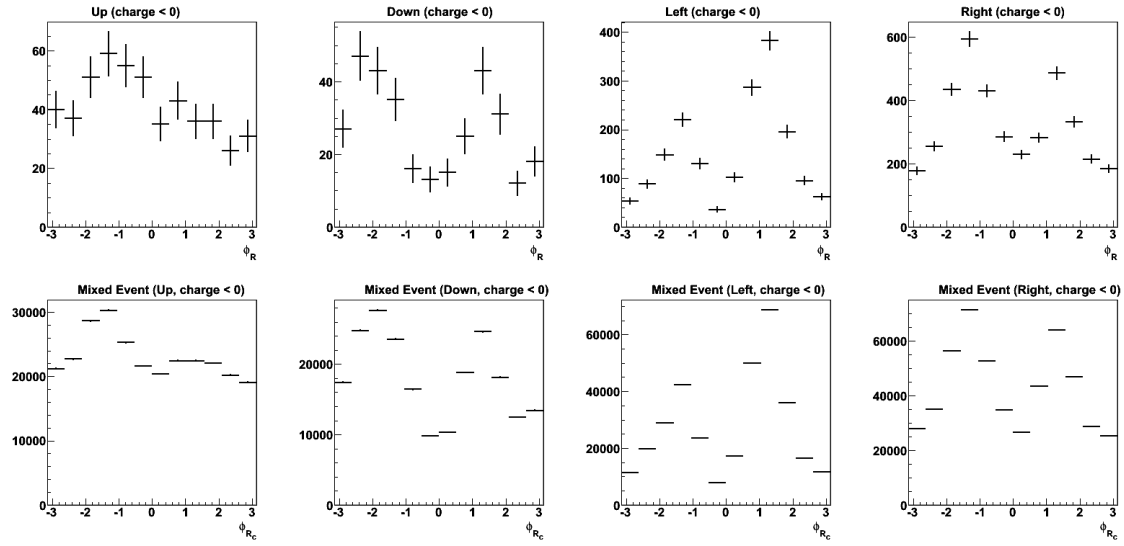


Fig. 49.: $\phi_R$ correlations for negatively-charged associations with (a) $\Delta R < 0.7$ and $1.0 < p_{T,\text{assoc}} < 2.0$ GeV/c and (b) $\Delta R < \pi/3$ and $0.5 < p_{T,\text{assoc}} < 1.0$ GeV/c. (a) separates the data into up ($0 < \phi_{\text{pair}} < \pi$) and down ($-\pi < \phi_{\text{pair}} < 0$) production, while (b) separates the data into left ($-\pi/2 < \phi_{\text{pair}} < \pi/2$) and right ($\pi/2 < \phi_{\text{pair}} < 3\pi/2$) production. The top row reflects raw $\phi_R$ correlations, while the bottom row reflects $\phi_R$ correlations for mixed events.

NLS frame, where $\vec{P}$ defines the $z$-axis. Then, $\phi_R$ is taken as the azimuthal angle of $\vec{R}$ when rotated into the NLS coordinates. The forthcoming spin asymmetries are measured using so-called cross-ratio techniques. This utilizes the symmetry of the detectors to combine yields from various portions of the detector in forming the asymmetries. Thus, it is useful to examine $\phi_R$ correlations when $\vec{P}$ falls in various detector locations. Figure 49 shows examples of correlations when $\vec{P}$ falls in either the "top" half, i.e. $0 < \phi_{\text{pair}} < \pi$, the "bottom" half, i.e. $-\pi < \phi_{\text{pair}} < 0$, the "left" half, i.e. $-\pi/2 < \phi_{\text{pair}} < \pi/2$, or the "right" half, i.e. $\pi/2 < \phi_{\text{pair}} < 3\pi/2$.

The acceptance issues shown in Fig. 42 complicate not only the azimuthal correlations as shown in Fig. 43, but also correlations in $\phi_R$. Two examples of these acceptance issues are shown in Fig. 49. Earlier, I discussed a mixed-event technique using histograms as a means to overcome such acceptance effects. For these $\phi_R$ acceptance issues I use a different event-mixing procedure. Here, I mix events with like properties. First, I divide the detector into six wedges in $\phi$ with three on the left-hand side ($-\pi/2 < \phi < \pi/2$) and three on the right ($\pi/2 < \phi < 3\pi/2$). I define "event classes" based on the wedge into which the event's trigger pion falls. For each event, the trigger pion is mixed with tracks from previous events of the same class. The tracks are stored in one of six buffers (one for each event class). After the event mixing, the tracks from the current event are stored in the buffer corresponding to the event class defined by the trigger pion. Since correlations are restricted by the pair-radius cut, the tracks are only stored if they fall within the class wedge or the two adjacent wedges. For the sake of computing efficiency, the buffer size is restricted to twenty tracks. After event mixing, the oldest tracks are removed to make room for the newest tracks if the buffer is full.

The $\phi_R$ correlations can be corrected for relative efficiency by dividing the raw yield by the mixed-event distributions. As shown in Fig. 50, the acceptance-corrected distributions can be fitted with a function of the form $p_0 \left[1 + p_1 \times \cos\left(\phi_R\right)\right]$. The constant scale parameters, then, factor out the absolute efficiency, which is not corrected, leaving the cosine term describing the physical aspects of the yield. The cosine fit parameters for positively-charged and negatively-charged correlations at three different pair-radius limits are summarized in Figs. 51 and 52. Statistics are limited, but within the available precision the cosine parameters do not show strong dependence on pair radius, charge sign, or location in the detector. The results suggest a positive value for the cosine parameter. This makes sense from a kinematics standpoint.

Given that I cut both the pions and associated particles in terms of $p_T$, the jet will tend to orient the particles to minimize the jet energy. This is achieved when the trigger, with higher $p_T$, falls to lower $\eta$ than the softer associated particle. So, the expectation is a bias toward production in the event plane with the trigger at lower $\eta$. With my definition of $\vec{P} = \vec{p}_{\pi^0} - \vec{p}_{\text{assoc}}$, the expected bias is toward $\phi_R = 0$ and, thus, positive cosine parameter. This is consistent with the results in Figs. 51 and 52. It is also possible, that the behavior is influenced by the so-called Boer-Mulders effect [22]. The Boer-Mulders effect is a correlation between the spin polarization and transverse momentum of partons within an unpolarized nucleon. By coupling with the Collins fragmentation function, this results in a $\cos\phi_R$ dependence in the unpolarized cross section, and for maximized scenarios, could be sizable at the kinematics of this analysis [23]. Since the asymmetry exists in the unpolarized cross section, to isolate the contribution of such an effect, this analysis would need far more rigorous understanding of acceptance inefficiencies and a robust quantification of the trigger-bias.

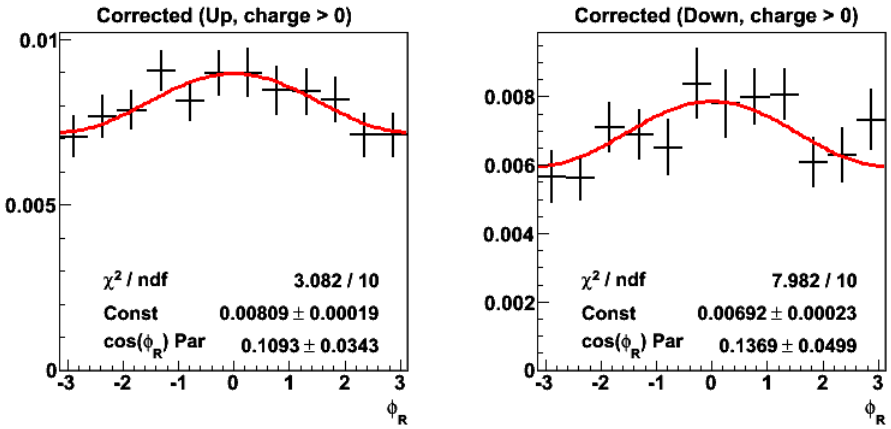


(a)

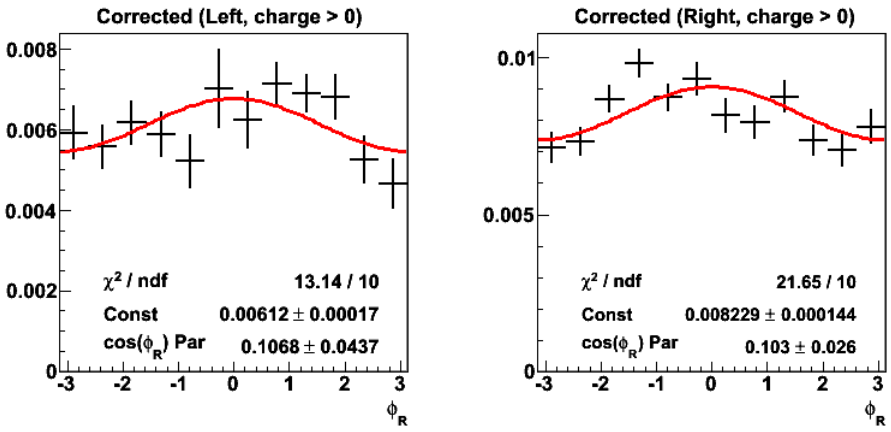


(b)

Fig. 50.: Acceptance-corrected $\phi_R$ correlations for positively-charged associations with $0.5 < p_{T,\text{assoc}} < 1.0$ GeV/c and (a) $\Delta R < 0.5$ and (b) $\Delta R < 0.7$. (a) separates the data into up ($0 < \phi_{\text{pair}} < \pi$) and down ($-\pi < \phi_{\text{pair}} < 0$) production, while (b) separates the data into left ($-\pi/2 < \phi_{\text{pair}} < \pi/2$) and right ($\pi/2 < \phi_{\text{pair}} < 3\pi/2$) production. The distributions have been fit with a function of the form $p_0\,[1 + p_1 \times \cos(\phi_R)]$. The differing constant scale parameters reflect differing absolute efficiency in the various portions of the detector. The peaks at $\phi_R \sim 0$ are consistent with kinematic expectation for my $p_T$ cuts.

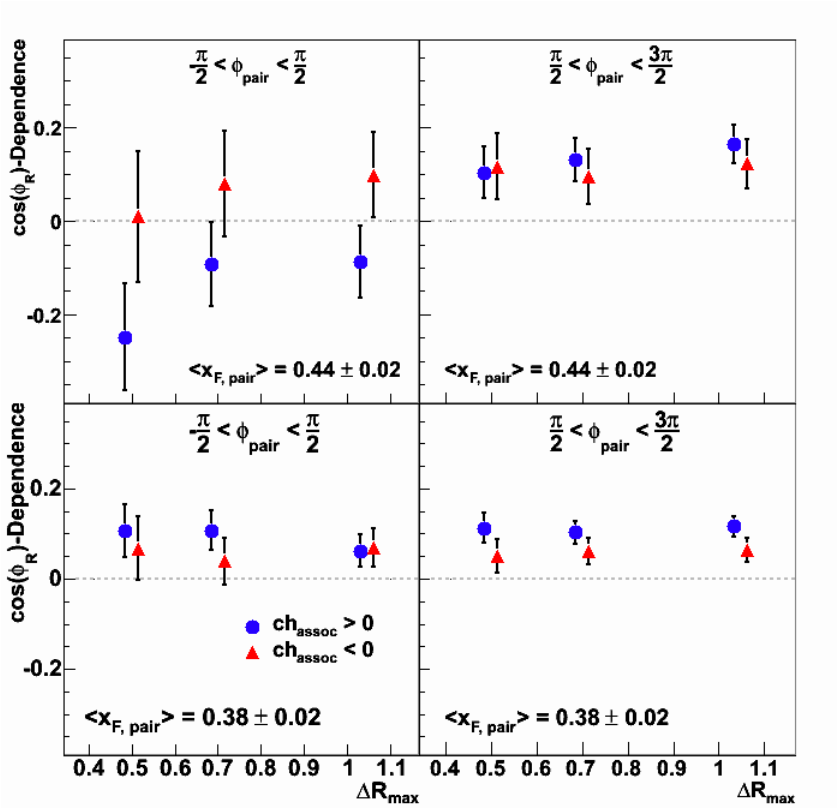


Fig. 51.: Cosine parameters describing $\phi_R$ correlations for three upper limits on pair radius. Errors are statistical only. The left column demonstrates results for left production, and the right column demonstrates results for right production. The top row reflects results for associations with $1 < p_T < 2$ GeV/c and the bottom row reflects results for associations with $0.5 < p_T < 1$ GeV/c. Within the statistical precision, the results do not reflect a strong dependence on pair radius, charge sign, $p_T$, and detector location.

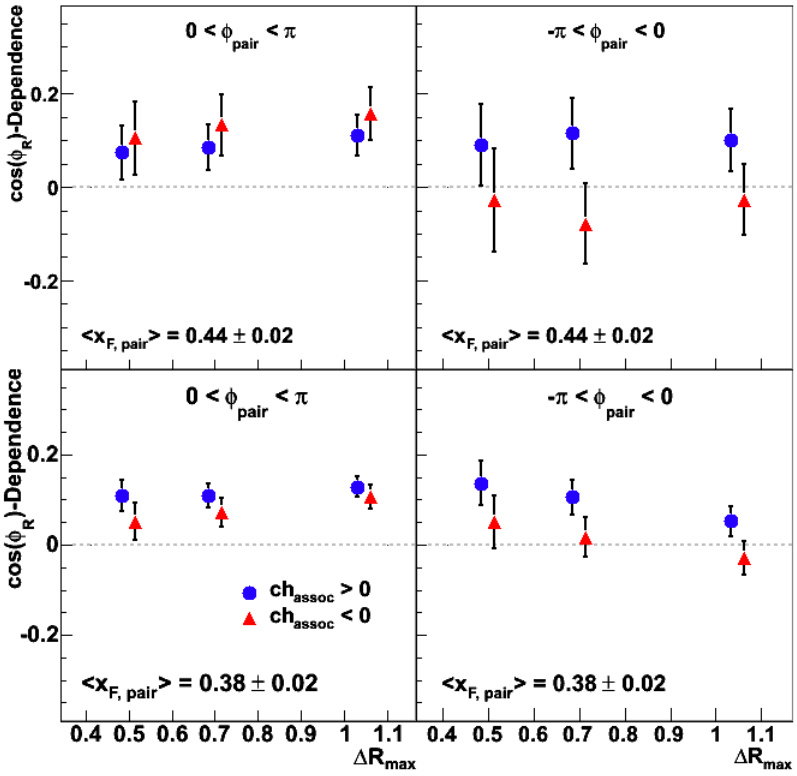


Fig. 52.: Cosine parameters describing $\phi_R$ correlations for three upper limits on pair radius. Errors are statistical only. The left column demonstrates results for up production, and the right column demonstrates results for down production. The top row reflects results for associations with $1 < p_T < 2$ GeV/c and the bottom row reflects results for associations with $0.5 < p_T < 1$ GeV/c. Within the statistical precision, the results do not reflect a strong dependence on pair radius, charge sign, $p_T$, and detector location.

# CHAPTER VII

## TWO-PARTICLE CORRELATION ASYMMETRIES

The presence of a $\pi^0$-charged particle correlation signal in the 200 GeV polarized-proton data (Fig. 46) affords the opportunity to study spin asymmetries beyond the current inclusive measurements from polarized-proton data discussed in chapter 1. Among the considerations in such an analysis are the effects of the observed acceptance inefficiencies (Fig. 42) and the effects of the large background under the correlation signal.

### A. Cross Ratios

Asymmetries are often measured as a function of the angle between the spin polarization direction and the event plane (the plane containing the axes of the beam and the scattered particle) (Eq. 2.25). The literature commonly defines the $x$-axis collinear with the event plane. Using this convention, for the Sivers effect, an asymmetry is measured in $\phi_S$ of the jet yield. A two-particle Sivers measurement is possible by considering the sum of the momentum vectors of the two particles, $\vec{p}_1 + \vec{p}_2$, as a surrogate for the jet axis. For an IFF measurement, an additional angle is needed. The asymmetry exists in $\phi_S - \phi_R$, where $\phi_R$ (Fig. 50) measures the azimuthal angle of $\vec{p}_1 - \vec{p}_2$ around the sum, $\vec{p}_1 + \vec{p}_2$.

Asymmetries can be measured in a variety of ways. First, it is possible to measure the angular dependence of cross sections, e.g.

$$d\sigma(\theta, \phi) = d\sigma_0(\theta)\left[1 + P_{\text{beam}} A(\theta)\right]. \tag{7.1}$$

However, this requires detailed knowledge of such elements as efficiencies and luminosities. Since RHIC beams flip the spin of proton bunches several million times per

second, it is possible to consider the difference in yields produced between collisions with "spin-up" and "spin-down,"

$$A = \frac{1}{P_{\text{beam}}} \frac{d\sigma^{\uparrow} - d\sigma^{\downarrow}}{d\sigma^{\uparrow} + d\sigma^{\downarrow}}. \tag{7.2}$$

In this formulation, detector acceptance effects cancel, however, knowledge of the relative spin-up and spin-down beam luminosities remains critical. In the absence of relative luminosity information, the cross-ratio formulation [85] provides a viable option for symmetric detectors. In the cross ratio formulation both detector acceptance and relative luminosity asymmetries cancel. Given the large acceptance asymmetries and the lack of relative luminosity information for the 2008 RHIC run, the cross-ratio formulation remains the best option for this analysis.

For the asymmetry measurements, I follow the approach of Bacchetta and Radici [47] with the caveat that I consider the incoming beam to be polarized rather than the target beam, as is the typical SIDIS convention. As with the unpolarized $\phi_R$ correlation analysis, I calculate two vectors: the sum vector $\vec{P} = \vec{p}_{\pi^0} + \vec{p}_h$ and the difference vector $\vec{R} = \vec{p}_{\pi^0} - \vec{p}_h$, where $h$ denotes the associated charged particle. For the polarized analysis, $\phi_R$ is calculated from the NLS frame, the same as in the unpolarized analysis. As depicted in Fig. 53, $\phi_S$ is calculated depending on the hemisphere into which $\vec{P}$ falls. If $\vec{P}$ falls in the upper (left) hemisphere, $\phi_S$ is the angle between $\vec{P}$ and the positive vertical axis, independent of whether the beam spin points up or down. If $\vec{P}$ falls in the lower (right) hemisphere, $\phi_S$ is the angle between $\vec{P}$ and the negative vertical axis. This convention ensures that like regions of the detector are compared when the spin is flipped.

Figure 53 provides a pictorial representation of the yields and angles contributing to the cross-ratio asymmetries. In this depiction the space is divided into an upper hemisphere and a lower hemisphere. The formulation is equally valid when divided

between left and right hemispheres. The yields, $\alpha$ and $\beta$, are functions of both $\phi_S$ and $\Delta\phi = \phi_S - \phi_R$. For each measurement, the cross ratio is constructed with the yields as

$$\epsilon = P_{\text{beam}} \times A = \frac{\sqrt{\alpha^{\uparrow}\beta^{\downarrow}} - \sqrt{\alpha^{\downarrow}\beta^{\uparrow}}}{\sqrt{\alpha^{\uparrow}\beta^{\downarrow}} + \sqrt{\alpha^{\downarrow}\beta^{\uparrow}}}, \tag{7.3}$$

where $\uparrow$ ($\downarrow$) denotes spin-up (spin-down). The product $\alpha^{\uparrow}\beta^{\downarrow}$ combines instrumental terms from both $\alpha$ and $\beta$ as well as luminosity terms from both spin-up and spin-down. Since the acceptance may be asymmetric between the two hemispheres, and the luminosity may differ between spin-up and spin-down, these terms may differ. The spin physics, however, is the same, between $\alpha^{\uparrow}$ and $\beta^{\downarrow}$, simply rotated into opposite detector hemispheres. Similarly, $\alpha^{\downarrow}\beta^{\uparrow}$ combines the same instrumental and luminosity terms as $\alpha^{\uparrow}\beta^{\downarrow}$, and the spin physics is the same between $\alpha^{\downarrow}$ and $\beta^{\uparrow}$. In the ideal case, then, the luminosity and acceptance terms factor from the numerator and denominator of Eq. 7.3, and the ratio cancels them. What remains is the spin physics, i.e. how the yields in $\alpha$ and $\beta$ change when the polarization is flipped.

For an IFF asymmetry, the yields are functions of $\Delta\phi$ integrated over $\phi_S$. For a Sivers asymmetry, the yields are functions of $\phi_S$ integrated over $\Delta\phi$. The statistical uncertainties in the raw cross ratio can be expressed

$$\delta\epsilon = \frac{\sqrt{(1-A)^2\left(\alpha^{\uparrow} + \beta^{\downarrow}\right)/4 + (1+A)^2\left(\alpha^{\downarrow} + \beta^{\uparrow}\right)/4}}{\sqrt{\alpha^{\uparrow}\beta^{\downarrow}} + \sqrt{\alpha^{\downarrow}\beta^{\uparrow}}}. \tag{7.4}$$

The analysis code is run twice for each measurement, once selecting spin-up events and once selecting spin-down events. The $\Delta\phi$ and $\phi_S$ yields are binned in histograms corresponding to the appropriate hemisphere. The cross ratios are constructed offline combining the appropriate yield histograms.

Aside from the physics cross-ratio asymmetry, two other cross ratios can be constructed with the yields. An instrumental cross ratio, measuring the detector

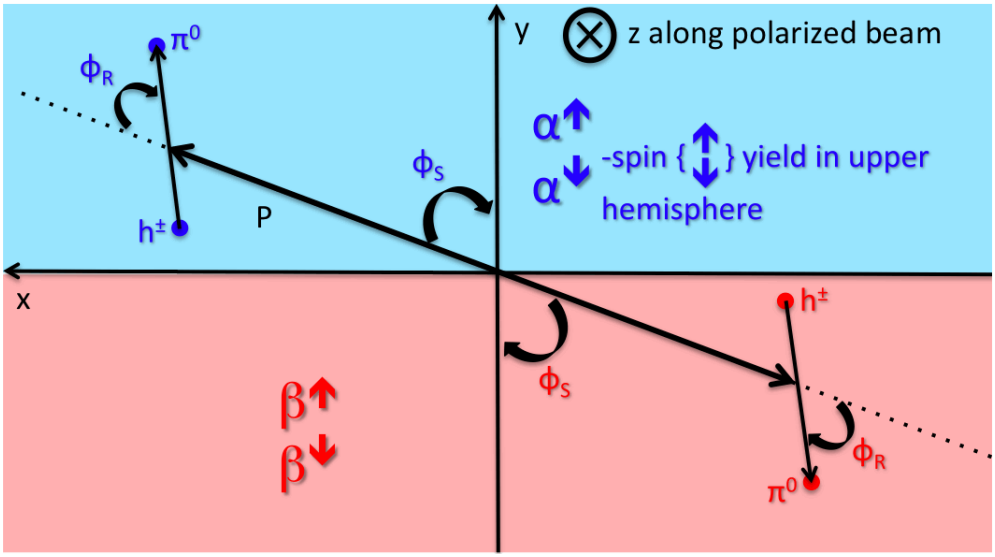


Fig. 53.: Pictorial diagram of yields and angles contributing to the cross-ratio asymmetries for the IFF and Sivers effects. More detailed diagrams are outlined by Bacchetta and Radici [47].

acceptance asymmetry, can be constructed as

$$I = \frac{\sqrt{\alpha^\uparrow \alpha^\downarrow} - \sqrt{\beta^\uparrow \beta^\downarrow}}{\sqrt{\alpha^\uparrow \alpha^\downarrow} + \sqrt{\beta^\uparrow \beta^\downarrow}}. \tag{7.5}$$

Additionally, a luminosity cross ratio, measuring the spin-up-spin-down beam asymmetry, can be constructed as

$$L = \frac{\sqrt{\alpha^\uparrow \beta^\uparrow} - \sqrt{\alpha^\downarrow \beta^\downarrow}}{\sqrt{\alpha^\uparrow \beta^\uparrow} + \sqrt{\alpha^\downarrow \beta^\downarrow}}. \tag{7.6}$$

Figure 54 shows an example of a set of IFF cross ratios for $x_F > 0$, $0.5 < p_T < 1.0$ GeV/c associations with negative charge, and $\Delta R < 0.7$. In this particular example, I have adopted the formulation where the space is divided into left and right hemispheres. The physics cross ratio is fit with a function of the form $p_0 + p_1 \sin(\Delta\phi)$. The asymmetry derives from the sine term, which for this example is

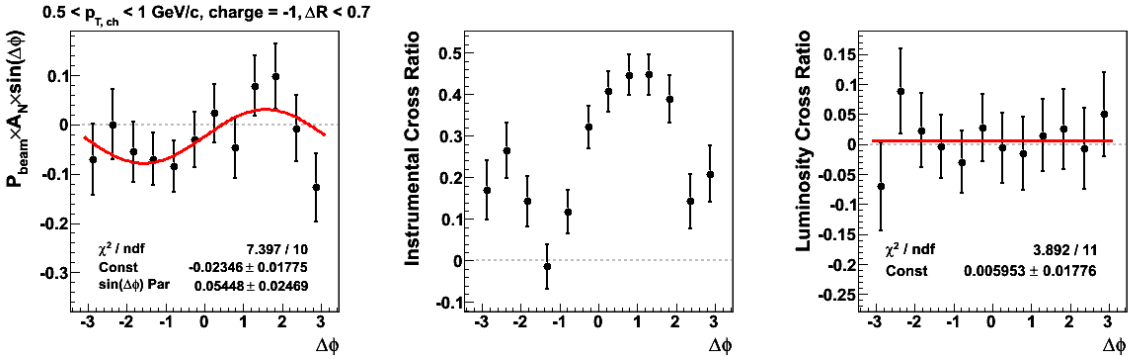


Fig. 54.: Raw IFF Cross Ratios for $\pi^0 - h^-$ with $0.5 < p_{T,h} < 1$ GeV/c, $\Delta R < 0.7$, and $x_F > 0$ uncorrected for backgrounds and polarization. The cross ratios reflect the left-right formulation. The physics cross ratio (left) is fit with a function of the form $p_0 + p_1 \sin(\Delta\phi)$ and returns a positive asymmetry of $2.2\sigma$. The instrumental cross ratio (center) shows considerable non-uniformity and sizable effects ($\approx 0.4$). The luminosity cross ratio (right) is fit with a constant, the value of which is small and consistent with 0.

$p_1 = 0.054 \pm 0.025$, a $2.2\sigma$ effect. The instrumental cross-ratio shows sizable structure and will be discussed in the forthcoming section. The luminosity cross ratio is fit with a constant, the value of which is quite small and consistent with zero within the available statistics. This is characteristic of the luminosity cross ratios for all cuts in $\Delta R$, $p_T$, and charge sign.

Figure 55 shows an example of a set of Sivers cross ratios for $x_F > 0$, $1.0 < p_T < 2.0$ GeV/c associations with negative charge, and $\Delta R < 0.7$. For this example, I have adopted the convention of dividing the space into up and down hemispheres. Furthermore, the left-right formulation yields identical results to the up-down formulation in the case of the Sivers asymmetry, since the data points are identical, shifted by a phase. Therefore, I will only show examples of Sivers asymmetries using the up-down convention. In this case, the physics cross ratio is fit with a function of the

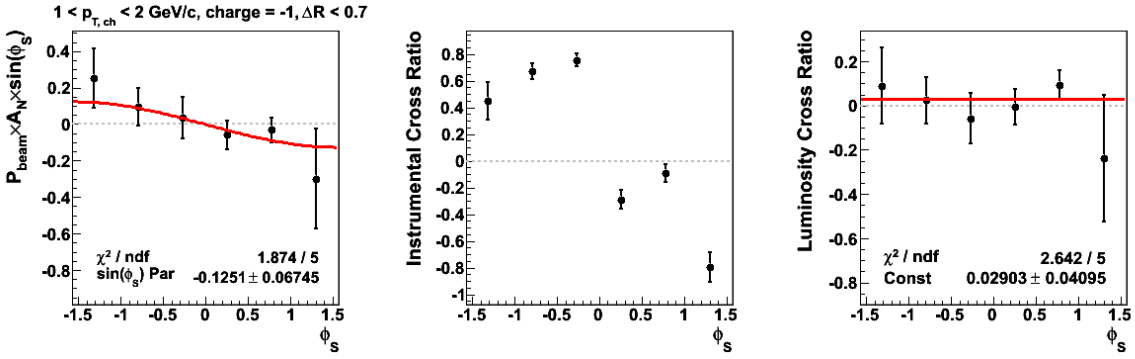


Fig. 55.: Sivers Cross Ratios for $\pi^0 - h^-$ with $1 < p_{T,h} < 2$ GeV/c, $\Delta R < 0.7$, and $x_F > 0$. The physics cross ratio (left) is fit with a function of the form $p_0 \sin(\phi_S)$ and returns a negative asymmetry of $1.9\sigma$. The instrumental cross ratio (center) shows considerable non-uniformity and sizable effects ($\approx \pm 0.8$). The luminosity cross ratio (right) is fit with a constant, the value of which is consistent with 0.

form $p_0 \sin(\phi_S)$. Again, the asymmetry derives from the sine term, which for this example is $p_0 = -0.125 \pm 0.067$, a $1.9\sigma$ effect. Just as in the IFF asymmetry example (Fig. 54), the instrumental cross ratio shows considerable structure and reaches values near 80%. The luminosity cross ratio is fit with a constant, as in the IFF example. Again, the value is consistent with zero; and, like the IFF case, this is typical for all combinations of cuts.

## B. Acceptance Effects

It is possible for asymmetries in a number of different angular moments to contribute to the yields depicted in Fig. 53. D'Alesio and company have shown that for the kinematics of this analysis only the Sivers and IFF effects contribute in a meaningful way, even for maximal considerations [23]. Thus, the yields from the two hemispheres

depicted in Fig. 53 can be expressed in terms of Sivers and IFF asymmetries as

$$\alpha^{\uparrow}(\Delta\phi,\phi_S) = \sigma\mathcal{L}^{\uparrow}I_{\alpha}(\Delta\phi,\phi_S)\left[1+P_{\text{beam}}\left(A_{\text{IFF}}\sin\Delta\phi+A_{\text{SIV}}\sin\phi_S\right)\right] \quad (7.7)$$

$$\alpha^{\downarrow}(\Delta\phi,\phi_S) = \sigma\mathcal{L}^{\downarrow}I_{\alpha}(\Delta\phi,\phi_S)\left[1-P_{\text{beam}}\left(A_{\text{IFF}}\sin\Delta\phi+A_{\text{SIV}}\sin\phi_S\right)\right] \quad (7.8)$$

$$\beta^{\downarrow}(\Delta\phi,\phi_S) = \sigma\mathcal{L}^{\downarrow}I_{\beta}(\Delta\phi,\phi_S)\left[1+P_{\text{beam}}\left(A_{\text{IFF}}\sin\Delta\phi+A_{\text{SIV}}\sin\phi_S\right)\right] \quad (7.9)$$

$$\beta^{\uparrow}(\Delta\phi,\phi_S) = \sigma\mathcal{L}^{\uparrow}I_{\beta}(\Delta\phi,\phi_S)\left[1-P_{\text{beam}}\left(A_{\text{IFF}}\sin\Delta\phi+A_{\text{SIV}}\sin\phi_S\right)\right], \quad (7.10)$$

where $\mathcal{L}^{\uparrow(\downarrow)}$ denotes spin-up(down) beam luminosity and $I_{\alpha(\beta)}$ denotes the instrumental acceptance of the $\alpha\,(\beta)$ hemisphere. For an IFF measurement, the yields are taken as functions of $\Delta\phi$, integrated over $\phi_S$. If the acceptance is uniform in $\phi_S$, $I_{\alpha}$ and $I_{\beta}$ will factor out from the cross ratio. Furthermore, in the up-down formulation, $\phi_S$ ranges from $-\pi/2$ to $\pi/2$; and the Sivers term disappears from the $\phi_S$-integrated yields. The IFF cross ratio completely decouples from the Sivers asymmetry, reducing to

$$\frac{1}{P_{\text{beam}}}\frac{\sqrt{\alpha^{\uparrow}\beta^{\downarrow}}-\sqrt{\alpha^{\downarrow}\beta^{\uparrow}}}{\sqrt{\alpha^{\uparrow}\beta^{\downarrow}}+\sqrt{\alpha^{\downarrow}\beta^{\uparrow}}} = A_{\text{IFF}}\sin(\Delta\phi). \quad (7.11)$$

In the left-right formulation, $\phi_S$ ranges from 0 to $\pi$ introducing a Sivers-asymmetry-dependent constant offset to the IFF asymmetry of the form

$$\frac{1}{P_{\text{beam}}}\frac{\sqrt{\alpha^{\uparrow}\beta^{\downarrow}}-\sqrt{\alpha^{\downarrow}\beta^{\uparrow}}}{\sqrt{\alpha^{\uparrow}\beta^{\downarrow}}+\sqrt{\alpha^{\downarrow}\beta^{\uparrow}}} = A_{\text{IFF}}\sin(\Delta\phi)+\frac{2}{\pi}A_{\text{SIV}}. \quad (7.12)$$

The same procedure can be applied for the Sivers asymmetry cross ratio yielding analogous results. If, however, the acceptance is not uniform in $\phi_S$, then the $I_{\alpha}$ and $I_{\beta}$ do not factor out from the cross ratio. The integration of $I(\Delta\phi,\phi_S)\,A_{\text{SIV}}\sin\phi_S$ terms couples the acceptance to the Sivers asymmetry resulting in a distortion of the IFF asymmetry. Analogously, for a Sivers asymmetry, non-uniformity in $\Delta\phi$ results in a distortion from coupling the instrumental effects to the IFF asymmetry in $\Delta\phi$-integrated yields.

The acceptance issues in the 2008 polarized-proton data (Fig. 42) translate into non-uniform acceptance in both $\Delta\phi$ and $\phi_S$. Figure 56 shows the effective $\phi_S$ coverage for each bin of $\Delta\phi$ for $\Delta R_{\max} = \pi/3$ with $0.5 < p_{T,h} < 1$ GeV/c. These inefficiencies lead to the instrumental effects seen in Fig. 49 as well as the instrumental asymmetries observed in Figs. 54 and 55. Thus, it is necessary to understand how the instrumental effects and competing asymmetries conspire to "leak-through" and distort the desired measurements.

## C. Leak-through Correction

One common technique in understanding how a true signal is distorted by non-physical effects is to implant an effect into the data and compare the known input to the recovered measurement. For this analysis, I wish to understand how the presence of a Sivers measurement distorts the measured IFF asymmetry and vice versa. One possibility, then, is to weight the IFF yields based on a Sivers asymmetry and construct the cross ratios with the Sivers-weighted yields. The difference between the weighted and un-weighted cross ratios, then, isolates the "leak-through" of the Sivers asymmetry to the IFF asymmetry. The exact analogy works for the leak-through of the IFF asymmetry to the Sivers.

One complication to this is that real IFF and Sivers effects may be present. These real effects, then, couple to the weighting factors to produce higher-order distortions which are difficult to quantify. One solution to this is to perform the weighting process in an unpolarized environment. Thus, real Sivers and IFF effects will be removed, and the resulting weighted cross ratios will only contain contributions from the input asymmetry.

To achieve the unpolarized scenario, I proceed in the same manner as the polar-

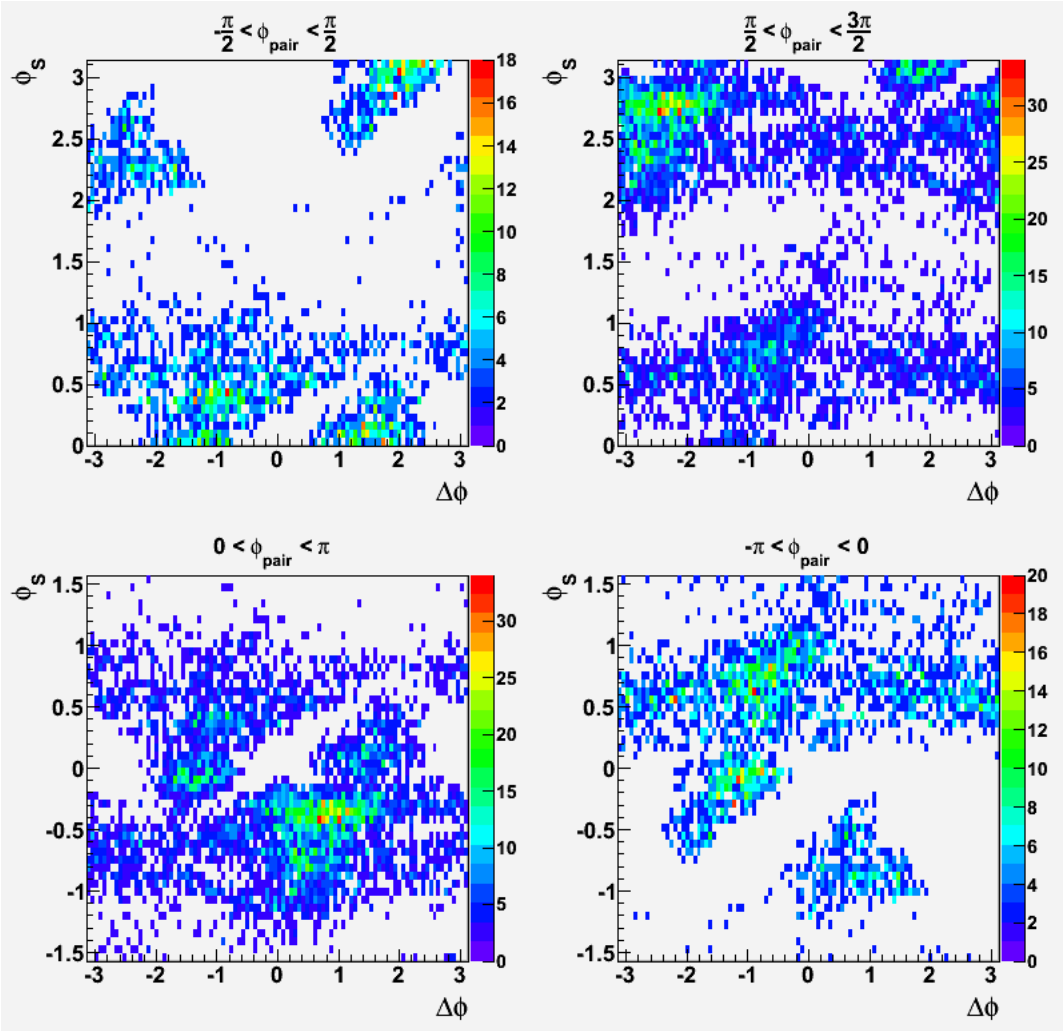


Fig. 56.: Effective $\phi_S$ coverage for each bin of $\Delta\phi$. Events satisfy $\Delta R < \pi/3$ and $0.5 < p_{T,\text{assoc}} < 1$ GeV/c. The non-uniform FMS gain coupled with hardware failures in the FTPC translate into the observed non-uniform acceptance in $\Delta\phi$-$\phi_S$ space. For an IFF measurement, this acceptance non-uniformity introduces a distortion by coupling to the Sivers asymmetry. Analogously, the acceptance introduces a distortion in the Sivers asymmetry by coupling to the IFF asymmetry.

ized analysis, now, removing the spin-state selection. For each event, I fill both the spin-up and spin-down yield histograms. I weight the Sivers yields for the actual spin state by $1 + A_{\rm IFF}^{\rm input} \sin\Delta\phi_{\rm true}$ and the Sivers yields for the opposite spin state by $1 - A_{\rm IFF}^{\rm input} \sin\Delta\phi_{\rm true}$. I weight the IFF yields for the actual spin state by $1+A_{\rm SIV}^{\rm input} \sin\phi_{S,\rm true}$ and the Sivers yields for the opposite spin state by $1 - A_{\rm SIV}^{\rm input} \sin\phi_{S,\rm true}$. Here, "true" denotes that the weighting factors utilize $\phi_S$ calculated relative to the actual spin direction, rather than the vertical direction corresponding to the hemispheres as depicted in Fig. 53. The statistical uncertainties for the weighted cross ratios can be expressed

$$\begin{aligned}(\delta\epsilon_w)^2 &= \frac{1}{(A+B)^4}\left\{\frac{B^2}{A^2}\left[\left(\beta^{\downarrow}\right)^2\sum_i\left(w_i^{\uparrow}\right)^2+\left(\alpha^{\uparrow}\right)^2\sum_j\left(w_j^{\downarrow}\right)^2\right]\right.\\ &\quad+\frac{A^2}{B^2}\left[\left(\beta^{\uparrow}\right)^2\sum_i\left(w_i^{\downarrow}\right)^2+\left(\alpha^{\downarrow}\right)^2\sum_j\left(w_j^{\uparrow}\right)^2\right]\\ &\quad\left.-2\left(\beta^{\downarrow}\beta^{\uparrow}\sum_i w_i^{\uparrow}w_i^{\downarrow}+\alpha^{\uparrow}\alpha^{\downarrow}\sum_j w_j^{\uparrow}w_j^{\downarrow}\right)\right\},\end{aligned} \tag{7.13}$$

where $A^2 = \alpha^{\uparrow}\beta^{\downarrow}$, $B^2 = \beta^{\uparrow}\alpha^{\downarrow}$, and $w_{i(j)}$ denotes the weight factor for $\alpha\,(\beta)$ yields. Two examples of unpolarized, weighted cross ratios are shown in Fig. 57. The Sivers leak-through cross ratios are fit with a function of the form $p_0 + p_1 \times \sin\Delta\phi$, and the IFF leak-through cross ratios are fit with a function of the form $p_0 \times \sin\Delta\phi$. The fits are often quite poor, however, they represent the leading-order harmonic terms. Given the size of the statistical uncertainties in the raw cross ratios, as well as the over-all small scale of the leak-through, the leading-order harmonics are sufficient. While the scale of the leak-through cross ratios, shown here for a 10% input asymmetry, is relatively small, the fluctuations are large compared to the statistical errors. Thus, the leak-through is real and can be removed from the raw physics cross ratios as an acceptance correction.

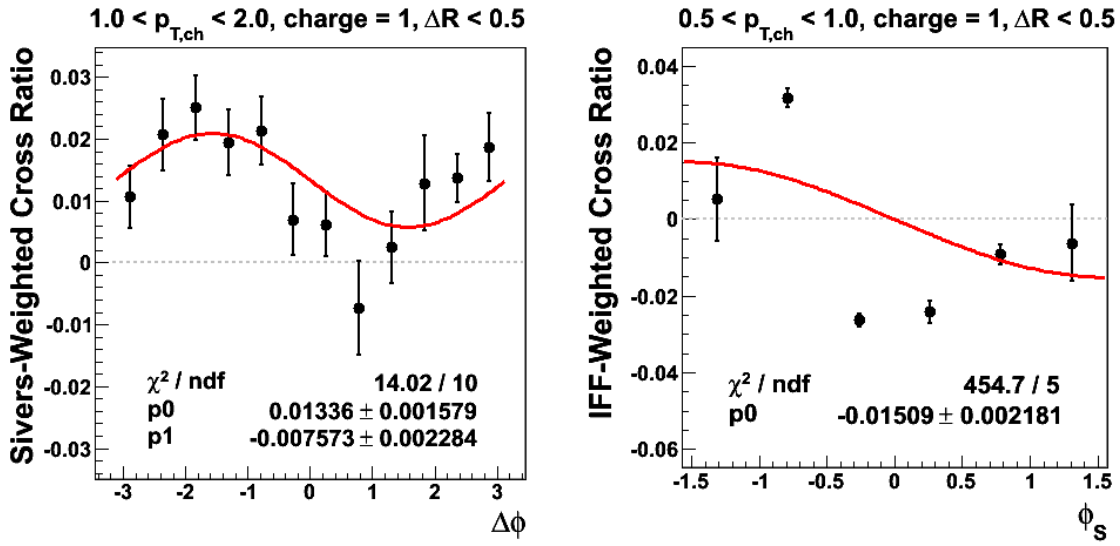


(a) (b)

Fig. 57.: Unpolarized cross ratios for (a) Sivers weighting and (b) IFF weighting, each with an input of $P_{\text{beam}} \times A = 10\%$. (a) shows up-down formulated IFF cross ratios for charged particles with $1 < p_T < 2$ GeV/c, positive charge, and $\Delta R < 0.5$. The cross ratio has been fit with a function of the form $p_0 + p_1 \times \sin(\Delta\phi)$. (b) shows up-down formulated Sivers cross ratios for charged particles with $0.5 < p_T < 1$ GeV/c, positive charge, and $\Delta R < 0.5$. The cross ratio has been fit with a function of the form $p_0 \times \sin(\phi_S)$.

To correct for competing effects, I, first, divide the Sivers leak-through cross ratios by the input asymmetry and scale by the raw, measured Sivers effect (e.g. Fig. 55). I, then, subtract the scaled leak-through cross ratios from the raw, measured IFF cross ratios. The resulting distribution can, then, be fit with a function of the form $p_0 + p_1 \times \sin\Delta\phi$ to extract the leak-through-corrected IFF asymmetry. To calculate the uncertainties, it is important to account for the large uncertainty from the Sivers asymmetry. One simple way to do this is by utilizing the first-order fits to the leak-through cross ratios. The parameters of the fit to the corrected distribution are approximately

$$p_i^{\rm corr} = p_i^{\rm uncorr} - p_i^{\rm leak}; \tag{7.14}$$

and, thus, the uncertainties are

$$(\delta p_i^{\rm corr})^2 = (\delta p_i^{\rm uncorr})^2 + \left(\delta p_i^{\rm leak}\right)^2. \tag{7.15}$$

The "uncorrected" uncertainties are simply those of the fit to the raw IFF cross ratios. The leak-through uncertainties, however, involve both the fit uncertainties as well as the Sivers asymmetry uncertainties. The leak-through fit parameters should scale with the Sivers asymmetry. Thus,

$$p_i^{\rm leak} = A_{\rm SIV} \times p_i^{\rm raw} \tag{7.16}$$

$$\left(\delta p_i^{\rm leak}\right)^2 = (A_{\rm SIV} \times \delta p_i^{\rm raw})^2 + (\delta A_{\rm SIV} \times p_i^{\rm raw})^2$$

$$\left(\delta p_i^{\rm leak}\right)^2 = \left(\delta p_i^{\rm leak-fit}\right)^2 + \left(p_i^{\rm leak} \times \frac{\delta A_{\rm SIV}}{A_{\rm SIV}}\right)^2, \tag{7.17}$$

where $\delta p_i^{\rm leak-fit}$ is the uncertainty of the fit to the leak-through cross ratio, which scales with the Sivers asymmetry. So, the calculated uncertainty on the leak-through-

corrected IFF asymmetry is

$$(\delta p_i^{\text{corr}})^2 = (\delta p_i^{\text{uncorr}})^2 + \left(\delta p_i^{\text{leak-fit}}\right)^2 + \left(\frac{\delta A_{\text{SIV}}}{A_{\text{SIV}}} \times p_i^{\text{leak}}\right)^2. \tag{7.18}$$

With the leak-through-corrected IFF asymmetries in hand, I, then, repeat the procedure to correct the leak-through on the Sivers asymmetries. This time, however, I use the corrected IFF asymmetries to scale the leak-through cross ratios. Given the size of the statistical uncertainties, any ambiguities from using uncorrected Sivers asymmetries to scale the leak-through cross ratios for the IFF correction should be negligible. Figure 58 shows examples of leak-through-corrected cross ratios for IFF and Sivers effects. These resulting cross ratios exhibit effects of $2.2\sigma$ and $2.5\sigma$, respectively.

## D. Scale Factors and Background Correction

So far, I have reported cross ratios uncorrected for polarization. To convert cross ratios to asymmetries, it is necessary to divide by the beam polarization. Such a correction is trivial, however, a more complicated question is how to correct for background and underlying event fractions. To a large degree, this question does not have a definitive answer and is worth some exploration.

When an asymmetry is measured, the yields are always a combination of signal and background. One way to visualize the situation is

$$A_{\text{meas}} = \frac{N_{\text{sig}}^{\uparrow} + \sum_i N_{\text{bg}}^{i\uparrow} - N_{\text{sig}}^{\downarrow} - \sum_i N_{\text{bg}}^{i\downarrow}}{N_{\text{tot}}}, \tag{7.19}$$

where $A_{\text{meas}}$ represents the measured asymmetry, $N_{\text{sig}}^{\uparrow(\downarrow)}$ represents the signal yield for spin-up or spin-down, the $N_{\text{bg}}^{i\uparrow(\downarrow)}$ terms represent the various background yields for spin-up or spin-down, and $N_{\text{tot}}$ represents the sum of all components. Equation 7.19 can be reexpressed in terms of its yield fractions to obtain an expression for the true

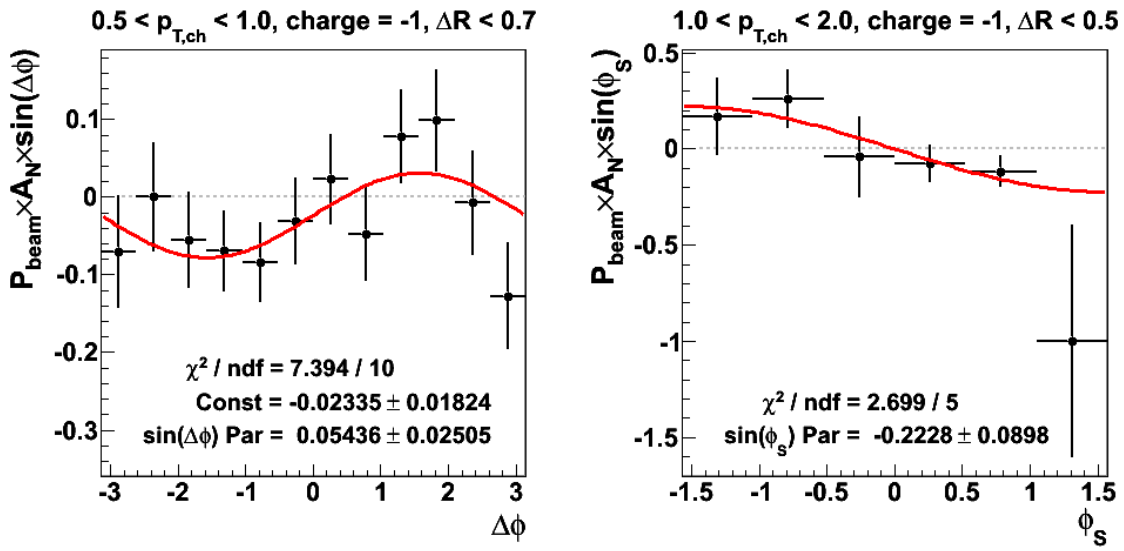


(a) (b)

Fig. 58.: Leak-through-corrected (a) IFF and (b) Sivers cross ratios. (a) is shown in the up-down formulatlion for associated charged particles with $0.5 < p_T < 1$ GeV/c, negative charge, and $\Delta R < 0.7$. (b) is shown in the up-down formulation for associated charged particles with $1 < p_T < 2$ GeV/c, negative charge, and $\Delta R < 0.5$. The corrections result in a (a) $2.2\sigma$ effect and a (b) $2.5\sigma$ effect.

asymmetry

$$\begin{aligned} A_{\text{meas}} &= \frac{\left(N_{\text{sig}}^{\uparrow} - N_{\text{sig}}^{\downarrow}\right) + \sum_i \left(N_{\text{bg}}^{i\uparrow} - N_{\text{bg}}^{i\downarrow}\right)}{N_{\text{tot}}} \\ &= \frac{N_{\text{sig}} A_{\text{sig}} + \sum_i N_{\text{bg}}^i A_{\text{bg}}^i}{N_{\text{tot}}} \\ &= f_{\text{sig}} A_{\text{sig}} + \sum_i f_{\text{bg}}^i A_{\text{bg}}^i \\ A_{\text{sig}} &= \frac{A_{\text{meas}} - \sum_i f_{\text{bg}}^i A_{\text{bg}}^i}{f_{\text{sig}}}, \end{aligned} \tag{7.20}$$

where $N_{\text{sig}}$ and $N_{\text{bg}}^i$ represent the components summed over spin states and the $f$ terms represent the various fractions of the total yield. So, given the appropriate background asymmetries, I can use the yield fractions listed in Table VI to correct the measured asymmetries to obtain the desired signal asymmetry. The two non-signal contributions for which I correct in this analysis are the pile-up and underlying-event backgrounds. Additionally, there is a contribution from the away-side peak. Most likely, the away-side contributions are simply artifacts of the fitting model coupled to the limited statistics. Thus, I treat the away-side fraction as an additional piece of the underlying event. The question, then, is what are the appropriate background asymmetries.

For the IFF measurement, I assume the pile-up background contains no asymmetry. The IFF asymmetry depends on the relative orientation of the associated particle and the trigger. Thus, if the associated particle is randomly oriented, furthermore, with no defined spin-state, as should be the case for pile-up, then there should exist no asymmetry in the IFF pile-up. For the Sivers measurement, on the other hand, I do assume a pile-up asymmetry. The Sivers effect is based on an asymmetry in the sum of the two-particle momenta. This is largely anchored by the trigger pion, which is prompt, carrying a defined spin-state. Since it is well known that the pion carries an asymmetry, I must assume some asymmetry for the Sivers pile-up.

Since the trigger pion carries the stiffer $p_T$ cut, it largely approximates the two-particle axis. So, one sensible way to model the asymmetry from pile-up is to dilute the pion asymmetry by a smearing function based on the difference of the pion and pair axes. For all series of cuts, $\phi_{S,\pi^0} - \phi_{S,\text{pair}} < 0.18$. If I convolute a sine function with a gaussian of RMS = 0.18, I find the sine amplitude damped by $< 2\%$. Thus, any effects from the axis smearing are negligible compared to the statistical uncertainties, and the pion asymmetry serves as the background asymmetry for Sivers pile-up.

Since one expects the underlying event to know nothing about the spin of the fragmenting parton, I assume no underlying event contribution to the IFF measurement. On the other hand, if the underlying event and signal interfere with each other, then, the IFF effect may have a greater reach than the near-side signal. For the Sivers effect, the situation is reversed. The Sivers asymmetry exists in the distribution of the hard-scattered parton. Thus, given no interference with the underlying event, the pion-underlying-event pair will carry an asymmetry I can approximate with the smearing procedure discussed above. If there is an interference, however, the situation changes, and I cannot assume the pion asymmetry survives in the underlying event. The existence of interference is a physics question, of course, and so I am motivated to two different corrections. First, I will present results correcting for the full underlying event and pile-up backgrounds, i.e.

$$A_{\text{sig}} = \frac{A_{\text{meas}} - A_{\text{bg}}\,(1 - f_{\text{sig}})}{f_{\text{sig}}}. \tag{7.21}$$

Second, I will also present results for only the pile-up correction, i.e.

$$A_{\text{sig}} = \frac{A_{\text{meas}} - f_{\text{pu}} \times A_{\text{bg}}}{1 - f_{\text{pu}}}, \tag{7.22}$$

where $f_{\text{pu}}$ is the pile-up fraction. Differences in the behavior may motivate further study to understand effects of final-state interactions (or the lack thereof) between

the near-side peak and underlying event. Additionally, for the full underlying-event and pile-up background corrections of the Sivers effect, I will factor into systematic estimations the difference of applying the pion asymmetry to the pile-up fraction only.

To remove the background asymmetries from the Sivers measurement, I need to understand what the pion asymmetry is for these kinematics. Earlier, I have shown the pion asymmetry as a function of $x_F$ (Fig. 26). However, now, I need to know the asymmetry integrated over $x_F$. Figure 59 shows the set of $\phi_S$ cross ratios for pions within $2 < p_T < 5$ GeV/c. The physics cross ratio has been corrected for polarization ($\langle P \rangle = 47 \pm 2\%$), finite binning, and acceptance effects. An asymmetry of $A_N = 0.027 \pm 0.003$, a $7.9\sigma$ effect, is evident. This value can be factored in as the pile-up and underlying-event backgrounds for the Sivers effect. For $x_F < 0$, I measure an asymmetry of $A_N = 0.0034 \pm 0.0034$. Additionally, Fig. 59 includes instrumental and luminosity cross ratios. The instrumental effects are quite sizable, emphasizing the importance of correctly handling statistics (e.g. Eq. 7.4). The luminosity cross ratio is quite small, however, a constant fit yields a $2.5\sigma$ effect. This suggests that though residual polarization may exist after summing over spin states in the unpolarized leak-through procedure, it is miniscule and negligible.

## E. Statistical Uncertainties

A major task in any physics analysis is to understand the statistical uncertainties. For Eq. 7.21, the statistical uncertainties can be expressed

$$\begin{aligned}
(\delta A_{\rm sig})^2 &= \left(\frac{\partial A_{\rm sig}}{\partial A_{\rm meas}}\delta A_{\rm meas}\right)^2 + \left(\frac{\partial A_{\rm sig}}{\partial A_{\rm bg}}\delta A_{\rm bg}\right)^2 + \left(\frac{\partial A_{\rm sig}}{\partial f_{\rm sig}}\delta f_{\rm sig}\right)^2 \\
&= \left(\frac{1}{f_{\rm sig}}\delta A_{\rm meas}\right)^2 + \left(\frac{1-f_{\rm sig}}{f_{\rm sig}}\delta A_{\rm bg}\right)^2 \\
&\quad + \left(\frac{A_{\rm meas} - A_{\rm bg}}{f_{\rm sig}}\frac{\delta f_{\rm sig}}{f_{\rm sig}}\right)^2 . \qquad (7.23)
\end{aligned}$$

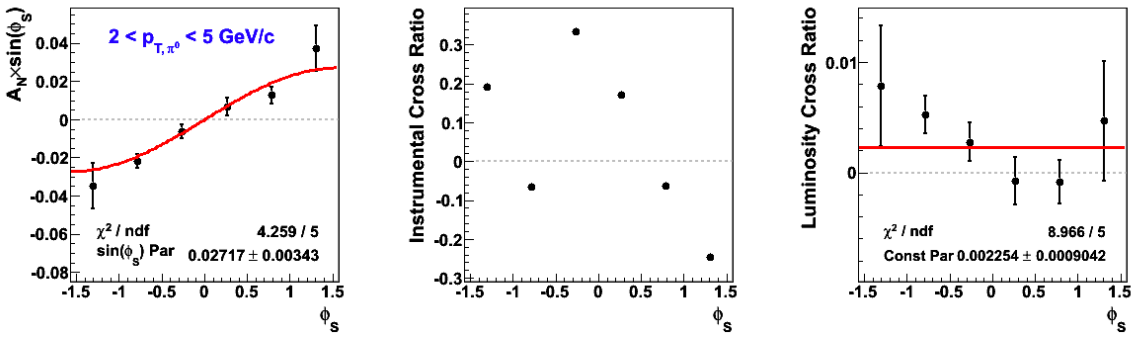


Fig. 59.: Cross ratios as a function of $\phi_S$ for trigger pions with $2 < p_T < 5$ GeV/c integrated over $x_F$. The physics asymmetry is shown corrected for beam polarization, binning, and finite acceptance. The trigger pions exhibit $A_N = 0.027 \pm 0.003$. For $x_F < 0$, the asymmetry is small and consistent with zero. This can be factored in as a correction for pile-up and underlying-event backgrounds for the Sivers asymmetry.

Similarly, for Eq. 7.22, the statistical uncertainties can be expressed

$$\begin{aligned}(\delta A_{\rm sig})^2 &= \left(\frac{1}{1-f_{\rm pu}}\delta A_{\rm meas}\right)^2 + \left(\frac{f_{\rm pu}}{1-f_{\rm pu}}\delta A_{\rm bg}\right)^2 \\ &\quad + \left(\frac{A_{\rm meas}-A_{\rm bg}}{1-f_{\rm pu}}\frac{\delta f_{\rm pu}}{1-f_{\rm pu}}\right)^2 . \end{aligned} \tag{7.24}$$

So, the statistical uncertainties can be divided into three groups: the measured asymmetries, the background asymmetries, and the yield fractions.

The uncertainty in the measured asymmetry can be expressed

$$\left(\frac{\delta A_{\rm meas}}{A_{\rm meas}}\right)^2 = \left(\frac{\delta \epsilon_{\rm meas}}{\epsilon_{\rm meas}}\right)^2 + \left(\frac{\delta P_{\rm meas}}{P_{\rm meas}}\right)^2 , \tag{7.25}$$

and, thus, contains two contributions: the uncertainty on the raw cross ratio (Eq. 7.4) and the uncertainty from the polarization. In this analysis, the limited statistics translate into large statistical uncertainties in the raw cross ratios. Furthermore, the large instrumental asymmetries work to compound the limitations of these uncertain-

ties. Additionally, the leak-through correction introduces uncertainties related to the measured effects (Eq. 7.18). For IFF and Sivers events, the average polarization is $48 \pm 2\%$ for $x_F > 0$ and $40 \pm 3\%$ for $x_F < 0$. The relative polarization uncertainty is quoted as $\delta P/P = 4.2\%$ for $x_F > 0$ and $\delta P/P = 7.2\%$ for $x_F < 0$ [86]. In all cases, the uncertainties related to the polarization are negligible compared to the raw cross-ratio uncertainties.

As I discussed, the uncertainties from the yield fractions, $f_{\rm sig}$ or $f_{\rm pu}$, are derived from fits tuned to the one-dimensional azimuthal correlations (Fig. 46). The uncertainties from the fit translate into uncertainties in the yield fractions (Table VI). In all cases, the yield fraction uncertainties are smaller than those from the cross ratio. However, in some cases the yield fraction uncertainties are still large enough that they contribute in a meaningful way to the over-all statistical uncertainty.

Uncertainties in the background asymmetry (Fig. 59) take on the same form as those from the measured asymmetry (Eq. 7.25). However, these uncertainties are quite small, relative to cross ratio uncertainties, and do not contribute in a meaningful way to the over-all statistical uncertainty.

## F. Systematic Uncertainties

In chapter 4, I show that autocorrelations between the FMS and FTPC exhibit a systematic offset in $\eta$ (Figs. 22 and 22). This has motivated a shift in the reconstructed photon location of $\delta\eta = -0.0256$ prior to reconstructing the $\pi^0$'s. However, it is important to understand how this photon shift changes the measured asymmetries. To this end, I have repeated the analysis, leaving the photons unshifted. For this pass, the autocorrelation veto is shifted to $-5/32 < \Delta\eta < 1/32$ and $-3\pi/100 < \Delta\phi < 3\pi/100$ to account for the shift in $\eta$. The difference between the shifted and

unshifted analyses is taken as the reconstruction systematic. In most cases, this reconstruction systematic is the largest of the systematic contributions.

As I discussed, additional systematic uncertainties arise from the fitting procedure. To estimate this, the two-dimensional correlation fit function has been tuned twice. The baseline measurement is taken by assuming an active range of $-1 < \Delta\eta < 1$. The function is also tuned to an active range of $-0.7 < \Delta\eta < 0.7$. The asymmetries are calculated using both functions, and the difference between the two sets the contribution to the systematic uncertainties.

The final systematic estimation comes from varying the background asymmetry contributions to the Sivers asymmetry. As I discussed earlier, the baseline measurement assumes the pion asymmetry applies to the full pile-up and underlying-event backgrounds. The asymmetry calculation is repeated, assuming the pion asymmetry only applies to the pile-up background. The difference between the two calculations sets the contribution to the systematic uncertainties. The three contributions are added in quadrature to estimate the total systematic uncertainty.

# CHAPTER VIII

# RESULTS AND CONCLUSIONS

## A. IFF and Sivers Asymmetries

Summarized in Tables VIII and IX and shown in Figs. 60 and 61 are full-background-corrected IFF asymmetries for $x_F > 0$ and $x_F < 0$. The asymmetries are shown for three upper-limits on the pair radius $\Delta R$. Asymmetries for $x_F < 0$ are consistent with zero. It is difficult to draw conclusions for $x_F > 0$ given the statistics limitations. There is some hint of a positive asymmetry ($\sim 2\sigma$ effect) for $\pi^0 - h^-$ with $x_F \approx 0.38$. All other bins are consistent with zero within the large statistical uncertainties.

Figure 62 shows full background-corrected Sivers asymmetries for $x_F > 0$ and $x_F < 0$. As with the IFF asymmetries, the Sivers asymmetries are shown for three different upper-limits on $\Delta R$. Again, asymmetries for $x_F < 0$ are consistent with zero. Most asymmetries for $x_F > 0$ are also consistent with zero, and the statistical uncertainties make further conclusions difficult. There is some hint of a negative effect ($\sim 1.7\sigma$) for $\pi^0 - h^-$ with $x_F \approx 0.44$. All other bins are consistent with zero. The values are summarized in Table X.

Given the questions concerning interference between the near-side peak and the underlying event, I also present results of only correcting for pile-up (Figs. 63, 64, 65). The values are summarized in Tables XI and XII Once again, statistics limit the ability to draw conclusions from the data. However, there is some hint that the data are less dependent on the pair radius after correcting for the underlying event. There is some ambiguity, however, as to what the pair-radius dependence should be. As I show in Fig. 8, HERMES and COMPASS observe some mass-dependence to the IFF asymmetry in SIDIS. Figures 47 and 48 illustrate that the pair mass varies with

Table VIII.: IFF Asymmetries in the up-down formulation for $p^{\uparrow} + p \to \pi^0 + h^{\pm} + X$ at $\sqrt{s} = 200$ GeV. Asymmetries are reported as $A + \delta A_{\text{stat}} + \delta A_{\text{syst}}$.

| $x_F = 0.44 \pm 0.02$ | | | |
|---|---|---|---|
| | $\Delta R_{\max} = \pi/3$ | $\Delta R_{\max} = 0.7$ | $\Delta R_{\max} = 0.5$ |
| $\pi^0 + h^+$ | $0.053 \pm 0.191 \pm 0.017$ | $0.035 \pm 0.164 \pm 0.043$ | $-0.160 \pm 0.178 \pm 0.075$ |
| $\pi^0 + h^-$ | $-0.193 \pm 0.231 \pm 0.052$ | $-0.150 \pm 0.200 \pm 0.049$ | $-0.248 \pm 0.228 \pm 0.054$ |

| $x_F = 0.38 \pm 0.02$ | | | |
|---|---|---|---|
| | $\Delta R_{\max} = \pi/3$ | $\Delta R_{\max} = 0.7$ | $\Delta R_{\max} = 0.5$ |
| $\pi^0 + h^+$ | $-0.030 \pm 0.179 \pm 0.011$ | $0.051 \pm 0.165 \pm 0.036$ | $-0.083 \pm 0.192 \pm 0.021$ |
| $\pi^0 + h^-$ | $0.278 \pm 0.219 \pm 0.060$ | $0.402 \pm 0.213 \pm 0.089$ | $0.412 \pm 0.241 \pm 0.128$ |

| $x_F = -0.44 \pm 0.02$ | | | |
|---|---|---|---|
| | $\Delta R_{\max} = \pi/3$ | $\Delta R_{\max} = 0.7$ | $\Delta R_{\max} = 0.5$ |
| $\pi^0 + h^+$ | $0.061 \pm 0.225 \pm 0.052$ | $0.072 \pm 0.193 \pm 0.030$ | $0.062 \pm 0.202 \pm 0.037$ |
| $\pi^0 + h^-$ | $-0.150 \pm 0.262 \pm 0.065$ | $-0.107 \pm 0.230 \pm 0.112$ | $0.039 \pm 0.257 \pm 0.133$ |

| $x_F = -0.38 \pm 0.02$ | | | |
|---|---|---|---|
| | $\Delta R_{\max} = \pi/3$ | $\Delta R_{\max} = 0.7$ | $\Delta R_{\max} = 0.5$ |
| $\pi^0 + h^+$ | $0.210 \pm 0.221 \pm 0.044$ | $0.278 \pm 0.206 \pm 0.080$ | $0.251 \pm 0.231 \pm 0.042$ |
| $\pi^0 + h^-$ | $0.165 \pm 0.242 \pm 0.114$ | $0.066 \pm 0.217 \pm 0.022$ | $0.062 \pm 0.256 \pm 0.040$ |

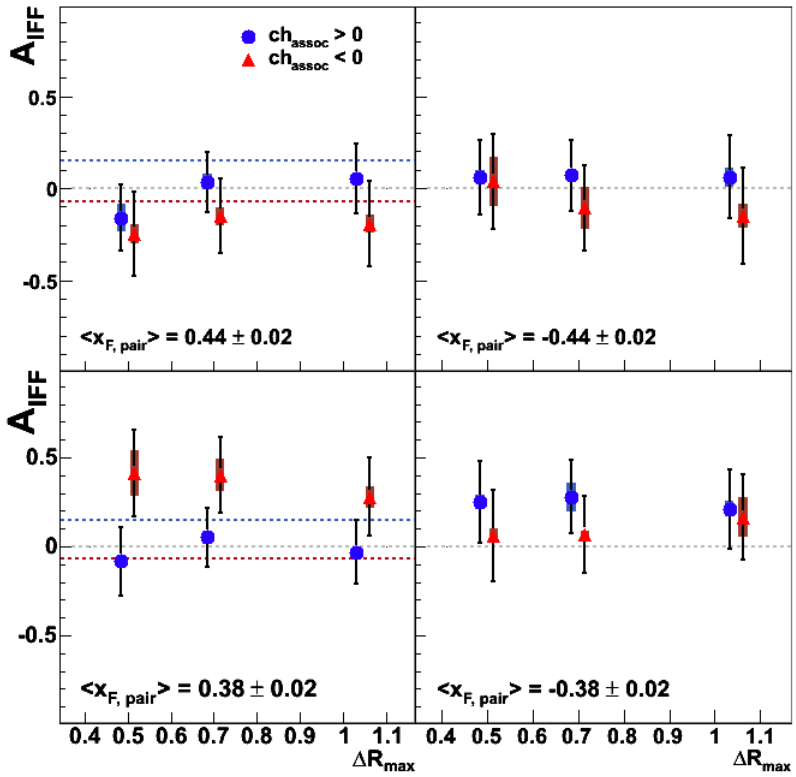


Fig. 60.: Background-corrected IFF asymmetries from the up-down formulation shown as a function of the upper-limit on pair radius from $p^{\uparrow} + p \rightarrow \pi^0 + h^{\pm} + X$ at $\sqrt{s} = 200$ GeV. The pions satisfy $2 < p_T < 5$ GeV/c, while the associated charged-particles satisfy (top) $1 < p_T < 2$ GeV and (bottom) $0.5 < p_T < 1$ GeV/c. The asymmetries are shown for (left) $x_F > 0$ and (right) $x_F < 0$. Systematic errors are shown as shaded boxes around the data points. The blue, dashed lines indicates the expected scale of the IFF effect for $\pi^0 - \pi^+$ (Eq. 1.36); and the red, dashed lines indicates the expected scale of the IFF effect for $\pi^0 - \pi^-$ (Eq. 1.37). Statistics limitations make drawing conclusions difficult.

Table IX.: IFF Asymmetries in the left-right formulation for $p^{\uparrow} + p \to \pi^0 + h^{\pm} + X$ at $\sqrt{s} = 200$ GeV. Asymmetries are reported as $A + \delta A_{\text{stat}} + \delta A_{\text{syst}}$.

| $x_F = 0.44 \pm 0.02$ | | | |
|---|---|---|---|
| | $\Delta R_{\text{max}} = \pi/3$ | $\Delta R_{\text{max}} = 0.7$ | $\Delta R_{\text{max}} = 0.5$ |
| $\pi^0 + h^+$ | $0.040 \pm 0.244 \pm 0.041$ | $0.108 \pm 0.225 \pm 0.079$ | $-0.032 \pm 0.243 \pm 0.147$ |
| $\pi^0 + h^-$ | $-0.212 \pm 0.283 \pm 0.053$ | $-0.049 \pm 0.253 \pm 0.040$ | $-0.168 \pm 0.287 \pm 0.021$ |

| $x_F = 0.38 \pm 0.02$ | | | |
|---|---|---|---|
| | $\Delta R_{\text{max}} = \pi/3$ | $\Delta R_{\text{max}} = 0.7$ | $\Delta R_{\text{max}} = 0.5$ |
| $\pi^0 + h^+$ | $0.013 \pm 0.218 \pm 0.038$ | $0.079 \pm 0.211 \pm 0.027$ | $-0.017 \pm 0.255 \pm 0.060$ |
| $\pi^0 + h^-$ | $0.469 \pm 0.282 \pm 0.126$ | $0.659 \pm 0.292 \pm 0.154$ | $0.644 \pm 0.324 \pm 0.184$ |

| $x_F = -0.44 \pm 0.02$ | | | |
|---|---|---|---|
| | $\Delta R_{\text{max}} = \pi/3$ | $\Delta R_{\text{max}} = 0.7$ | $\Delta R_{\text{max}} = 0.5$ |
| $\pi^0 + h^+$ | $0.083 \pm 0.234 \pm 0.021$ | $0.101 \pm 0.216 \pm 0.039$ | $0.183 \pm 0.240 \pm 0.045$ |
| $\pi^0 + h^-$ | $-0.262 \pm 0.286 \pm 0.059$ | $-0.166 \pm 0.256 \pm 0.087$ | $-0.302 \pm 0.298 \pm 0.228$ |

| $x_F = -0.38 \pm 0.02$ | | | |
|---|---|---|---|
| | $\Delta R_{\text{max}} = \pi/3$ | $\Delta R_{\text{max}} = 0.7$ | $\Delta R_{\text{max}} = 0.5$ |
| $\pi^0 + h^+$ | $0.181 \pm 0.218 \pm 0.065$ | $0.184 \pm 0.210 \pm 0.094$ | $0.101 \pm 0.251 \pm 0.041$ |
| $\pi^0 + h^-$ | $0.102 \pm 0.238 \pm 0.131$ | $0.003 \pm 0.230 \pm 0.014$ | $-0.013 \pm 0.277 \pm 0.080$ |

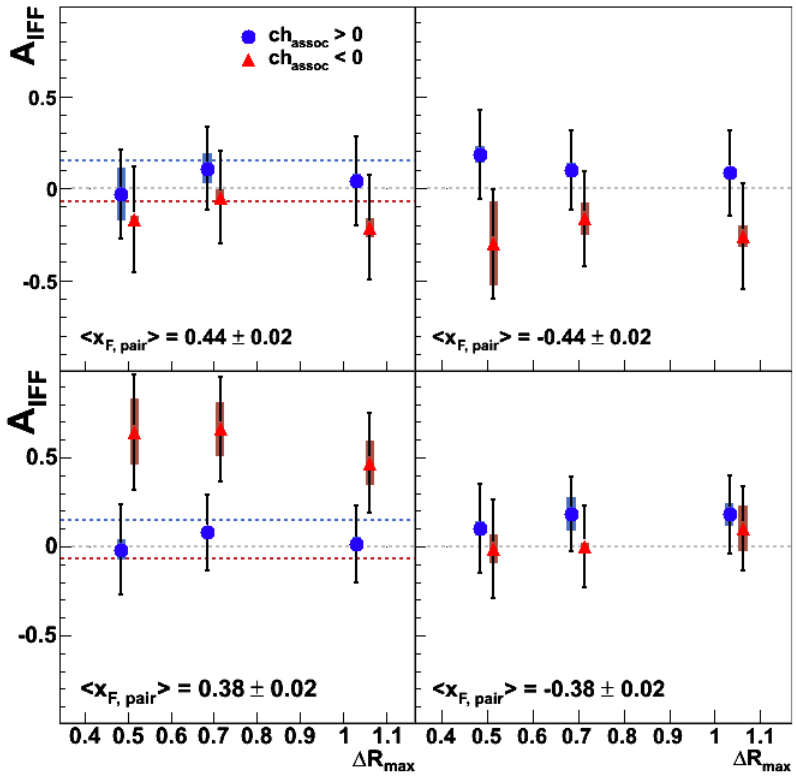


Fig. 61.: Background-corrected IFF asymmetries from the left-right formulation shown as a function of the upper-limit on pair radius from $p^{\uparrow} + p \rightarrow \pi^0 + h^{\pm} + X$ at $\sqrt{s} = 200$ GeV. The pions satisfy $2 < p_T < 5$ GeV/c, while the associated charged-particles satisfy (top) $1 < p_T < 2$ GeV and (bottom) $0.5 < p_T < 1$ GeV/c. The asymmetries are shown for (left) $x_F > 0$ and (right) $x_F < 0$. Systematic errors are shown as shaded boxes around the data points. The blue, dashed lines indicates the expected scale of the IFF effect for $\pi^0 - \pi^+$ (Eq. 1.36); and the red, dashed lines indicates the expected scale of the IFF effect for $\pi^0 - \pi^-$ (Eq. 1.37). Statistics limitations make drawing conclusions difficult.

Table X.: Sivers Asymmetries for $p^{\uparrow}+p \to \pi^0+h^{\pm}+X$ at $\sqrt{s} = 200$ GeV. Asymmetries are reported as $A + \delta A_{\rm stat} + \delta A_{\rm syst}$.

| $x_F = 0.44 \pm 0.02$ | | | |
|---|---|---|---|
| | $\Delta R_{\rm max} = \pi/3$ | $\Delta R_{\rm max} = 0.7$ | $\Delta R_{\rm max} = 0.5$ |
| $\pi^0 + h^+$ | $0.098 \pm 0.280 \pm 0.141$ | $0.121 \pm 0.244 \pm 0.055$ | $0.130 \pm 0.264 \pm 0.131$ |
| $\pi^0 + h^-$ | $-0.503 \pm 0.363 \pm 0.116$ | $-0.509 \pm 0.310 \pm 0.103$ | $-0.742 \pm 0.360 \pm 0.251$ |

| $x_F = 0.38 \pm 0.02$ | | | |
|---|---|---|---|
| | $\Delta R_{\rm max} = \pi/3$ | $\Delta R_{\rm max} = 0.7$ | $\Delta R_{\rm max} = 0.5$ |
| $\pi^0 + h^+$ | $-0.175 \pm 0.266 \pm 0.138$ | $-0.091 \pm 0.231 \pm 0.140$ | $-0.007 \pm 0.265 \pm 0.256$ |
| $\pi^0 + h^-$ | $-0.211 \pm 0.295 \pm 0.098$ | $0.052 \pm 0.258 \pm 0.073$ | $-0.027 \pm 0.305 \pm 0.059$ |

| $x_F = -0.44 \pm 0.02$ | | | |
|---|---|---|---|
| | $\Delta R_{\rm max} = \pi/3$ | $\Delta R_{\rm max} = 0.7$ | $\Delta R_{\rm max} = 0.5$ |
| $\pi^0 + h^+$ | $-0.450 \pm 0.376 \pm 0.172$ | $-0.290 \pm 0.298 \pm 0.045$ | $-0.180 \pm 0.303 \pm 0.070$ |
| $\pi^0 + h^-$ | $-0.101 \pm 0.336 \pm 0.082$ | $-0.219 \pm 0.314 \pm 0.073$ | $-0.503 \pm 0.376 \pm 0.183$ |

| $x_F = -0.38 \pm 0.02$ | | | |
|---|---|---|---|
| | $\Delta R_{\rm max} = \pi/3$ | $\Delta R_{\rm max} = 0.7$ | $\Delta R_{\rm max} = 0.5$ |
| $\pi^0 + h^+$ | $-0.503 \pm 0.331 \pm 0.109$ | $-0.183 \pm 0.270 \pm 0.043$ | $-0.110 \pm 0.312 \pm 0.170$ |
| $\pi^0 + h^-$ | $0.251 \pm 0.334 \pm 0.140$ | $0.125 \pm 0.305 \pm 0.083$ | $-0.245 \pm 0.364 \pm 0.221$ |

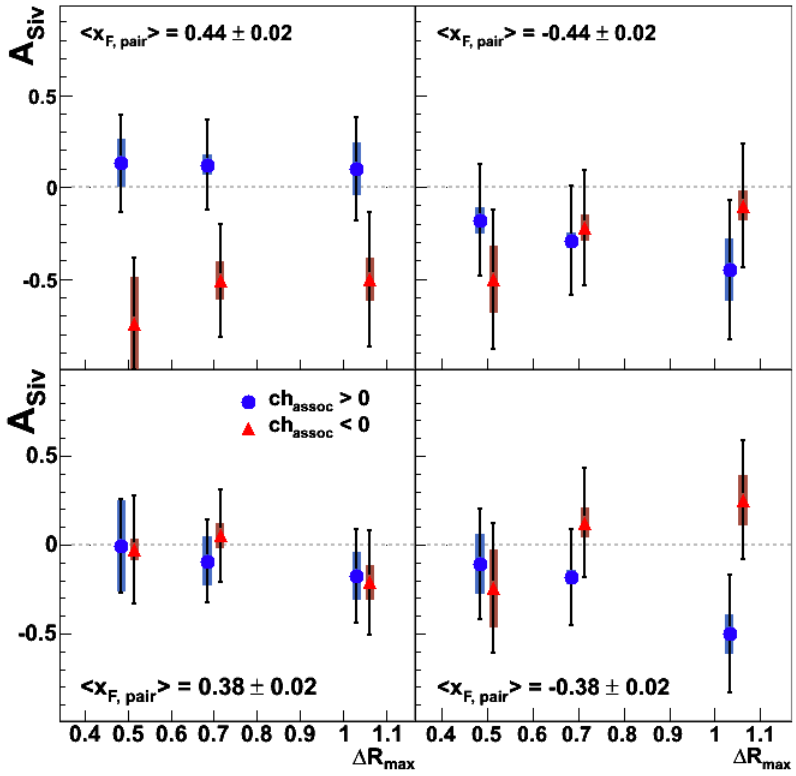


Fig. 62.: Background-corrected Sivers asymmetries shown as a function of the upper-limit on pair radius from $p^{\uparrow} + p \rightarrow \pi^0 + h^{\pm} + X$ at $\sqrt{s} = 200$ GeV. The pions satisfy $2 < p_T < 5$ GeV/c, while the associated charged-particles satisfy (top) $1 < p_T < 2$ GeV and (bottom) $0.5 < p_T < 1$ GeV/c. The asymmetries are shown for (left) $x_F > 0$ and (right) $x_F < 0$. Systematic errors are shown as shaded boxes around the data points. Statistics limitations make drawing conclusions difficult.

the pair-radius cut. Thus, one might expect some sensitivity with the pair-radius. Unfortunately, statistics render this question unanswered by this study.

## B. Final Considerations

Unfortunately, statistics limit the conclusions one can draw from this study. There are some hints at effects in $\pi^0 + h^-$ for $x_F \approx 0.38$ IFF asymmetries and $x_F \approx 0.44$ Sivers asymmetries. Furthermore, there is also some hint that asymmetries are less sensitive to pair radius after underlying-event correction. However, more data is needed to conclude any further.

As of the fall of 2011, the FTPC has been removed from STAR. The 2008 $p + p$ data are the only transverse-spin data that exist with the FMS trigger and read-out of the slow-detectors. Thus, the data reported in this analysis are the only data that will exist for these measurements at STAR. Further study at STAR requires a forward tracking upgrade.

Table XI.: Pile-up-only corrected IFF Asymmetries for $p^{\uparrow} + p \rightarrow \pi^0 + h^{\pm} + X$ at $\sqrt{s} = 200$ GeV. Asymmetries are reported as $A + \delta A_{\text{stat}} + \delta A_{\text{syst}}$.

| $x_F = 0.44 \pm 0.02$ Up-Down | | | |
|---|---|---|---|
| | $\Delta R_{\text{max}} = \pi/3$ | $\Delta R_{\text{max}} = 0.7$ | $\Delta R_{\text{max}} = 0.5$ |
| $\pi^0 + h^+$ | $0.024 \pm 0.085 \pm 0.005$ | $0.022 \pm 0.100 \pm 0.024$ | $-0.110 \pm 0.119 \pm 0.051$ |
| $\pi^0 + h^-$ | $-0.086 \pm 0.097 \pm 0.018$ | $-0.091 \pm 0.118 \pm 0.029$ | $-0.171 \pm 0.150 \pm 0.034$ |

| $x_F = 0.38 \pm 0.02$ Up-Down | | | |
|---|---|---|---|
| | $\Delta R_{\text{max}} = \pi/3$ | $\Delta R_{\text{max}} = 0.7$ | $\Delta R_{\text{max}} = 0.5$ |
| $\pi^0 + h^+$ | $-0.007 \pm 0.043 \pm 0.003$ | $0.017 \pm 0.054 \pm 0.011$ | $-0.031 \pm 0.071 \pm 0.006$ |
| $\pi^0 + h^-$ | $0.067 \pm 0.049 \pm 0.004$ | $0.132 \pm 0.061 \pm 0.015$ | $0.154 \pm 0.083 \pm 0.038$ |

| $x_F = 0.44 \pm 0.02$ Left-Right | | | |
|---|---|---|---|
| | $\Delta R_{\text{max}} = \pi/3$ | $\Delta R_{\text{max}} = 0.7$ | $\Delta R_{\text{max}} = 0.5$ |
| $\pi^0 + h^+$ | $0.018 \pm 0.109 \pm 0.016$ | $0.066 \pm 0.135 \pm 0.043$ | $-0.022 \pm 0.167 \pm 0.099$ |
| $\pi^0 + h^-$ | $-0.095 \pm 0.121 \pm 0.017$ | $-0.030 \pm 0.154 \pm 0.024$ | $-0.115 \pm 0.194 \pm 0.004$ |

| $x_F = -0.38 \pm 0.02$ Left-Right | | | |
|---|---|---|---|
| | $\Delta R_{\text{max}} = \pi/3$ | $\Delta R_{\text{max}} = 0.7$ | $\Delta R_{\text{max}} = 0.5$ |
| $\pi^0 + h^+$ | $0.003 \pm 0.052 \pm 0.010$ | $0.026 \pm 0.069 \pm 0.008$ | $-0.006 \pm 0.096 \pm 0.023$ |
| $\pi^0 + h^-$ | $0.113 \pm 0.059 \pm 0.017$ | $0.217 \pm 0.079 \pm 0.029$ | $0.241 \pm 0.107 \pm 0.053$ |

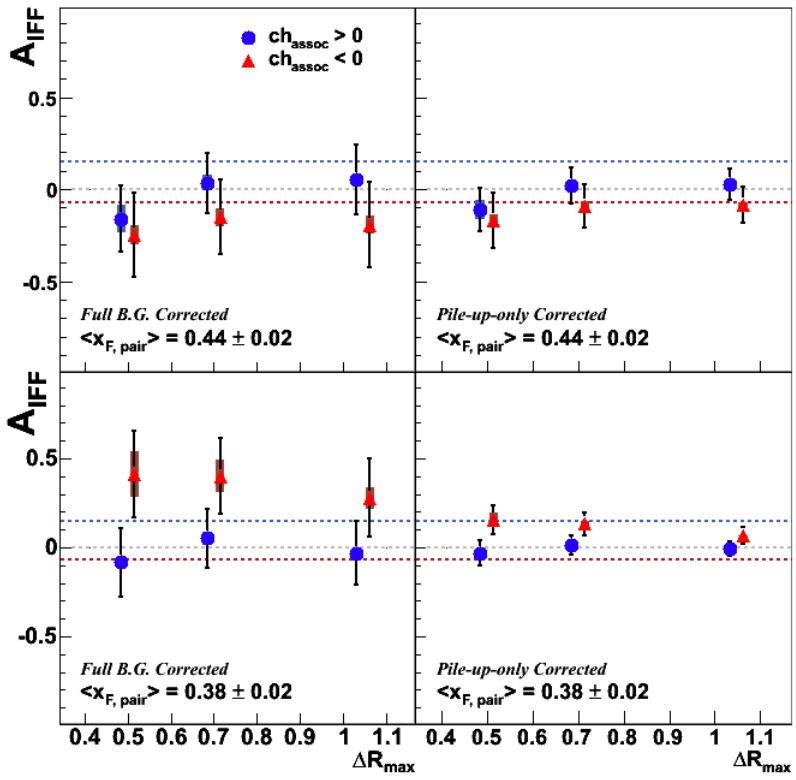


Fig. 63.: IFF asymmetries from the up-down formulation shown as a function of the upper-limit on pair radius from $p^{\uparrow} + p \rightarrow \pi^0 + h^{\pm} + X$ at $\sqrt{s} = 200$ GeV. The asymmetries are shown for two different sets of background correction: (left) full pile-up and underlying event correction and (right) pile-up-only correction. The blue, dashed lines indicates the expected scale of the IFF effect for $\pi^0 - \pi^+$ (Eq. 1.36); and the red, dashed lines indicates the expected scale of the IFF effect for $\pi^0 - \pi^-$ (Eq. 1.37). As before, statistics limitations make conclusions difficult, however, it appears the full background correction may hint at a slower pair-radius dependence.

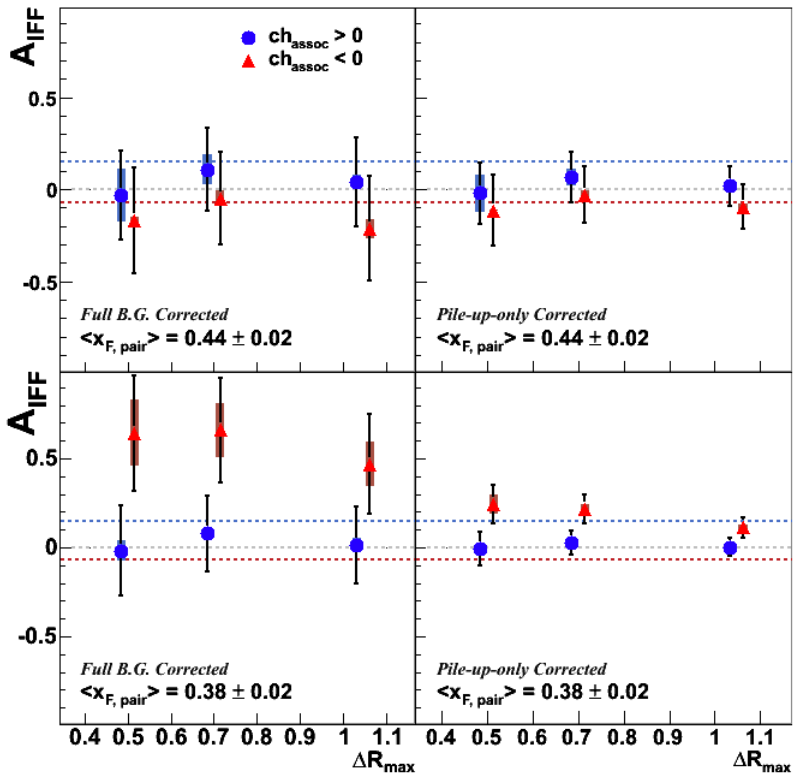


Fig. 64.: IFF asymmetries from the left-right formulation shown as a function of the upper-limit on pair radius for $p^{\uparrow} + p \rightarrow \pi^0 + h^{\pm} + X$ at $\sqrt{s} = 200$ GeV. The asymmetries are shown for two different sets of background correction: (left) full pile-up and underlying event correction and (right) pile-up-only correction. The blue, dashed lines indicates the expected scale of the IFF effect for $\pi^0 - \pi^+$ (Eq. 1.36); and the red, dashed lines indicates the expected scale of the IFF effect for $\pi^0 - \pi^-$ (Eq. 1.37). As before, statistics limitations make conclusions difficult, however, it appears the full background correction may hint at a slower pair-radius dependence.

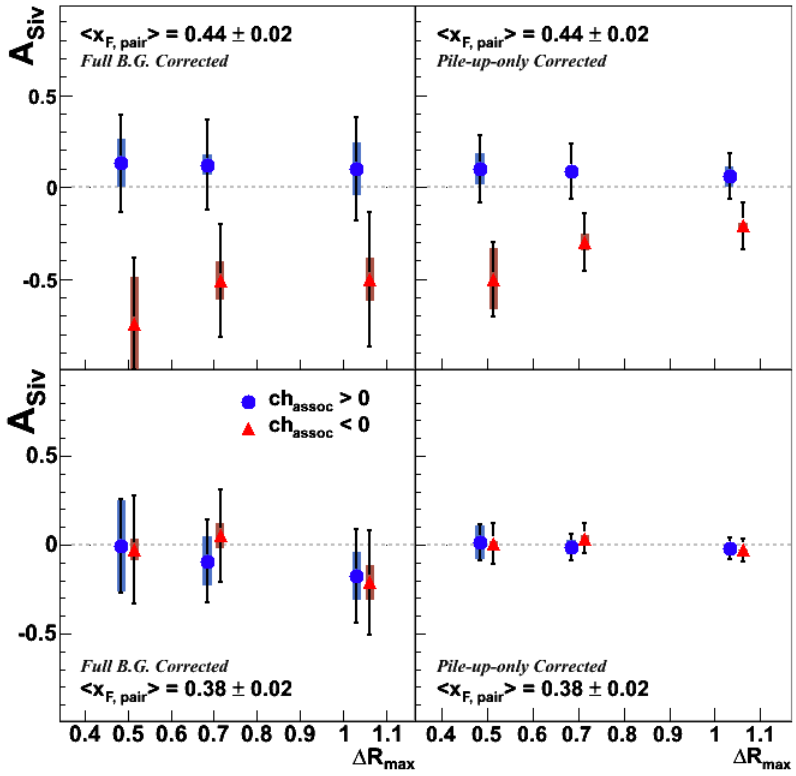


Fig. 65.: Sivers asymmetries shown as a function of the upper-limit on pair radius for $p^{\uparrow} + p \rightarrow \pi^0 + h^{\pm} + X$ at $\sqrt{s} = 200$ GeV. The asymmetries are shown for two different sets of background correction: (left) full pile-up and underlying event correction and (right) pile-up-only correction. As before, statistics limitations make conclusions difficult, however, it appears the full background correction may hint at a slower pair-radius dependence.

Table XII.: Pile-up-only corrected Sivers Asymmetries for $p^{\uparrow} + p \to \pi^0 + h^{\pm} + X$ at $\sqrt{s} = 200$ GeV. Asymmetries are reported as $A + \delta A_{\text{stat}} + \delta A_{\text{syst}}$.

| $x_F = 0.44 \pm 0.02$ | | | |
|---|---|---|---|
| | $\Delta R_{\text{max}} = \pi/3$ | $\Delta R_{\text{max}} = 0.7$ | $\Delta R_{\text{max}} = 0.5$ |
| $\pi^0 + h^+$ | $0.059 \pm 0.125 \pm 0.055$ | $0.085 \pm 0.148 \pm 0.027$ | $0.098 \pm 0.181 \pm 0.084$ |
| $\pi^0 + h^-$ | $-0.209 \pm 0.128 \pm 0.012$ | $-0.299 \pm 0.157 \pm 0.046$ | $-0.501 \pm 0.203 \pm 0.168$ |

| $x_F = 0.38 \pm 0.02$ | | | |
|---|---|---|---|
| | $\Delta R_{\text{max}} = \pi/3$ | $\Delta R_{\text{max}} = 0.7$ | $\Delta R_{\text{max}} = 0.5$ |
| $\pi^0 + h^+$ | $-0.022 \pm 0.060 \pm 0.022$ | $-0.012 \pm 0.074 \pm 0.040$ | $0.014 \pm 0.099 \pm 0.095$ |
| $\pi^0 + h^-$ | $-0.030 \pm 0.066 \pm 0.006$ | $0.035 \pm 0.085 \pm 0.017$ | $0.007 \pm 0.114 \pm 0.013$ |

# REFERENCES


[1] E. Leader, AIP Conf. Proc. **1149**, 11 (2009).

[2] L. Dick *et al.*, Phys. Lett. B **57**, 93 (1975); R. D. Klem *et al.*, Phys. Rev. Lett. **36**, 929 (1976); W. H. Dragoset, Jr. *et al.*, Phys. Rev. D **18**, 3939 (1978); D. Aschman *et al.*, Nucl. Phys. **B142**, 220 (1978).

[3] G. L. Kane, J. Pumplin, and W. Repko, Phys. Rev. Lett. **41**, 1689 (1978).

[4] J. Antille *et al.*, Phys. Lett. B **94**, 532 (1980).

[5] V. D. Apokin *et al.*, Phys. Lett. B **243**, 461 (1990).

[6] B. E. Bonner *et al.* (FNAL-E704 Collaboration), Phys. Rev. Lett. **61**, 1918 (1988); A. Bravar *et al.* (FNAL-E704 Collaboration), *ibid.* **77**, 2626 (1996); D. L. Adams *et al.* (FNAL-E581/704 Collaboration), Phys. Lett. B **261**, 201 (1991); D. L. Adams *et al.* (FNAL-E704 Collaboration), *ibid.* **264**, 462 (1991); Z. Phys. C **56**, 181 (1992).

[7] C. Bourrely and J. Soffer, Eur. Phys. J. C **36**, 371 (2004).

[8] J. Adams *et al.* (STAR Collaboration), Phys. Rev. Lett. **92**, 171801 (2004).

[9] B. I. Abelev *et al.* (STAR Collaboration), Phys. Rev. Lett. **101**, 222001 (2008).

[10] I. Arsene *et al.* (BRAHMS Collaboration), Phys. Rev. Lett. **101**, 042001 (2008).

[11] S. Adler *et al.* (PHENIX Collaboration), Phys. Rev. Lett. **95**, 202001 (2005).

[12] J. Adams *et al.* (STAR Collaboration), Phys. Rev. Lett. **97**, 152302 (2006).

[13] E. Leader, *Spin in Particle Physics*, edited by T. Ericson and P. V. Landshoff (Cambridge University Press, Cambridge, United Kingdom, 2001).

[14] U. D'Alesio and F. Murgia, Phys. Rev. D **70**, 074009 (2004).

[15] D. Sivers, Phys. Rev. D **41**, 83 (1990); **43**, 261 (1991).

[16] J. C. Collins, Nucl. Phys. **B396**, 161 (1993).

[17] F. Yuan, Phys. Lett. B **666**, 44 (2008).

[18] S. J. Brodsky, D. S. Hwang, and I. Schmidt, Phys. Lett. B **530**, 99 (2002).

[19] J. C. Collins, Phys. Lett. B **536**, 43 (2002).

[20] M. Anselmino, M. Boglione, U. DAlesio, E. Leader, and F. Murgia, Phys. Rev. D **71**, 014002 (2005).

[21] M. Anselmino *et al.*, in *Proc. of the II International Workshop on Transverse Polarisation Phenomena in Hard Processes* (World Scientific, Singapore, 2009), pp. 122–129.

[22] D. Boer and P. J. Mulders, Phys. Rev. D **57**, 5780 (1998).

[23] U. D'Alesio, F. Murgia, and C. Pisano, Phys. Rev. D **83**, 034021 (2011).

[24] J. Qiu and G. Sterman, Phys. Rev. D **59**, 014004 (1998).

[25] C. Kouvaris, J. Qiu, W. Vogelsang, and F. Yuan, Phys. Rev. D **74**, 114013 (2006).

[26] X. Ji, J. Qiu, W. Vogelsang, and F. Yuan, Phys. Rev. Lett. **97**, 082002 (2006).

[27] J. Collins and J. Qiu, Phys. Rev. D **75**, 114014 (2007).

[28] T. C. Rodgers and P. J. Mulders, Phys. Rev. D **81**, 094006 (2010); T. C. Rodgers and P. J. Mulders, arXiv:1102.4569 [hep-ph].

[29] X. Ji and F. Yuan, Phys. Lett. B **543**, 66 (2002); X. Ji, J. P. Ma, and F. Yuan, *ibid.* **597**, 299 (2004); A. V. Belitsky, X. Ji, and F. Yuan, Nucl. Phys. **B656**, 165 (2003); X. Ji, J. P. Ma, and F. Yuan, Phys. Rev. D **71**, 034005 (2005).

[30] F. Yuan, Phys. Rev. Lett. **100**, 032003 (2008).

[31] Z. Kang and J. Qui, Phys. Rev. Lett. **103**, 172001 (2009).

[32] A. Airapetian *et al.* (HERMES Collaboration), Phys. Rev. Lett. **103**, 152002 (2009); **94**, 012002 (2005); L. L. Pappalardo (HERMES Collaboration), Eur. Phys. J. A **38**, 145 (2008); M. Diefenthaler (HERMES Collaboration), in *Proceedings of the XV International Workshop on Deep Inelastic Scattering* (Atlantis Press/Science Wise, Amsterdam, 2007); L. Pappalardo (HERMES Collaboration), in *Proceedings of the XIV International Workshop on Deep Inelastic Scattering* (World Scientific, Singapore, 2007), p. 667; M. Diefenthaler (HERMES Collaboration), AIP Conf. Proc. **792**, 933 (2005).

[33] M. G. Alekseev *et al.* (COMPASS Collaboration), Phys. Lett. B **692**, 240 (2010); **673**, 127 (2009); E. S. Ageev *et al.*, Nucl. Phys. **B765**, 31 (2007); V. Y. Alexakhin *et al.* (COMPASS Collaboration), Phys. Rev. Lett. **94**, 202002 (2005).

[34] R. Seidl *et al.* (BELLE Collaboration), Phys. Rev. D **78**, 032011 (2008); Phys. Rev. Lett. **96**, 232002 (2006).

[35] M. Anselmino *et al.*, Eur. Phys. J. A **39**, 89 (2009).

[36] M. Anselmino *et al.*, Phys. Rev. D **71**, 074006 (2005).

[37] D. de Florian, R. Sassot, and M. Stratmann, Phys. Rev. D **75**, 114010 (2007).

[38] M. Glück, E. Reya, and A. Vogt, Eur. Phys. J. C **5**, 461 (1998).

[39] A. D. Martin, R. G. Roberts, W. J. Stirling, and R. Thorne, Phys. Lett. B **531**, 216 (2002).

[40] M. Anselmino *et al.*, in *Proceedings of the XVII International Workshop on Deep Inelastic Scattering* (Science Wise Press, Amsterdam, 2009).

[41] M. Anselmino *et al.*, Nucl. Phys. B Proc. Suppl. **191**, 98 (2009).

[42] M. Glück, E. Reya, M. Stratmann, and W. Vogelsang, Phys. Rev. D **63**, 094005 (2001).

[43] J. Soffer, Phys. Rev. Lett. **74**, 1292 (1995).

[44] J. C. Collins, S. F. Heppelmann, and G. A. Ladinsky, Nucl. Phys. **B420**, 565 (1994); J. C. Collins and G. A. Ladinsky, arXiv:hep-ph/9411444 (1994).

[45] X. Ji, Phys. Rev. D **49**, 114 (1994).

[46] R. L. Jaffe, X. Jin, and J. Tang, Phys. Rev. Lett. **80**, 1166 (1998).

[47] A. Bacchetta and M. Radici, Phys. Rev. D **70**, 094032 (2004).

[48] A. Bacchetta and M. Radici, Phys. Rev. D **67**, 094002 (2003).

[49] A. Airapetian *et al.* (HERMES Collaboration), JHEP **06**, 017 (2008).

[50] H. Wollny, Ph.D. thesis, Universität Freiburg, Freiburg im Breisgau, Germany, 2010.

[51] A. Vossen *et al.* (BELLE Collaboration), Phys. Rev. Lett. **107**, 072004 (2011).

[52] A. D. Martin, W. J. Stirling, R. S. Thorne, and G. Watt, Eur. Phys. J. C **63**, 189 (2009).

[53] A. Bacchetta, A. Courtoy, and M. Radici, Phys. Rev. Lett. **107**, 012001 (2011).

[54] J. Koster (PHENIX Collaboration), Transverse Spin Physics at PHENIX, 2010, presented at the RBRC Workshop on Progress in High-pT Physics at RHIC.

[55] E. Merzbacher, *Quantum Mechanics*, 3rd ed. (John Wiley and Sons, Inc., New York, 1998).

[56] M. Jacob and G. C. Wick, Annals of Physics **7**, 404 (1959).

[57] DOE/NSF Nuclear Science Advisory Committee, A Long Range Plan for Nuclear Science, 1983, `http://science.energy.gov/~/media/np/nsac/pdf/docs/lrp_1983.pdf`.

[58] J. Collins *et al.*, AIP Conf. Proc. **223**, 1 (1991).

[59] RHIC Spin Collaboration, Proposal on Spin Physics Using the RHIC Polarized Collider (R5), 1992, submitted to the BNL PAC.

[60] A. N. Zelenski *et al.*, in *Proceedings of the 1999 IEEE Particle Accelerator Conference* (IEEE, Piscataway, New Jersey, 1999), p. 106.

[61] I. Alekseev *et al.*, Nucl. Instrum. Meth. **A499**, 392 (2003).

[62] L. H. Thomas, Philos. Mag. **3**, 1 (1927); V. Bargmann, L. Michel, and V. Telegdi, Phys. Rev. Lett. **2**, 435 (1959).

[63] Y. S. Derbenev *et al.*, Part. Accel. **8**, 115 (1978).

[64] M. Bai, RHIC Polarized Proton Operation, 2008, presented at the 4th Electron Ion Collider Workshop, http://web.mit.edu/eicc/Hampton08/PRESENTATIONS/Tuesday_plenary_II/RHICpp_EIC_SOFFICE.ppt.

[65] J. Kiryluk (STAR Collaboration), AIP Conf. Proc. **675**, 424 (2003).

[66] K. H. Akermann *et al.* (STAR Collaboration), Nucl. Instrum. Meth. **A499**, 624 (2003).

[67] K. H. Akermann *et al.*, Nucl. Instrum. Meth. **A499**, 659 (2003).

[68] M. Beddo *et al.*, Nucl. Instrum. Meth. **A499**, 725 (2003).

[69] K. H. Ackermann *et al.*, Nucl. Instrum. Meth. **A499**, 713 (2003).

[70] C. E. Allgower *et al.*, Nucl. Instrum. Meth. **A499**, 740 (2003).

[71] L. C. Bland *et al.*, Eur. Phys. J. C **43**, 427 (2005).

[72] F. S. Bieser *et al.*, Nucl. Instrum. Meth. **A499**, 766 (2003).

[73] J. M. Landgraf *et al.* (STAR Collaboration), Nucl. Instrum. Meth. **A499**, 762 (2003).

[74] H. Hümmler, Ph.D. thesis, Technical University, München, Germany, 2000; Simulation and Reconstruction of Data from the STAR FTPC, 2000, STAR Note SN0429, http://drupal.star.bnl.gov/STAR/starnotes/public/sn0429.

[75] P. Yepes, Nucl. Instrum. Meth. **A380**, 582 (1996); M. Oldenburg, Ph.D. thesis, Technical University, München, Germany, 2001.

[76] Y. Wang, Ph.D. thesis, University of Texas, Austin, Texas, 2004.

[77] J. Putschke, Ph.D. thesis, Max Plank Institut für Physics, München, Germany, 2004.

[78] B. Back *et al.*, Phys. Rev. Lett. **91**, 052303 (2003).

[79] J. Putschke, Particle production and transverse dynamics in Au+Au and d+Au in the FTPCs, 2004, presented at the STAR Collaboration Meeting, `http://www.star.bnl.gov/protected/ftpc/putschke/ftpc_spectra.ppt`.

[80] B. I. Abelev *et al.* (STAR Collaboration), Nucl. Phys. **A832**, 134 (2010).

[81] J. Adams *et al.* (STAR Collaboration), Phys. Rev. Lett. **91**, 072304 (2003).

[82] F. Simon, Ph.D. thesis, Max Plank Institut für Physics, München, Germany, 2005.

[83] N. Poljak (STAR Collaboration), AIP Conf. Proc. **1149**, 521 (2009).

[84] L. Eun, Ph.D. thesis, Pennsylvania State University, University Park, Pennsylvania, 2011.

[85] G. Ohlsen and P. K. Jr., Nucl. Instrum. Meth. **109**, 41 (1973).

[86] CNI Polarimeter Group, 2008 Polarizations for RHIC, 2008, `http://www4.rcf.bnl.gov/~cnipol/pubdocs/Run08Offline/NOTE_2008_Polarizations_RHIC.txt`.

# VITA

James Lucus Drachenberg is a native of Atascocita, Texas, and a graduate of Northland Christian School in Houston, Texas, where he received his diploma in May 2000. He earned the degree of Bachelor of Science with a major in Physics from Abilene Christian University in May 2004. Afterward, he enrolled in graduate school at Texas A&M University, where he was admitted to doctoral candidacy in September 2010. During his time at Texas A&M University, he married his wife, Dr. Annie Sprott Drachenberg, M.D., on June 7, 2008, and welcomed his first child, Daniel James Drachenberg, on November 12, 2011. He may be reached at Cyclotron Institute, Texas A&M University, 3366 TAMU, College Station, Texas, 77843-3366.

The typist for this thesis was James Lucus Drachenberg.